KINETIC INDUCTANCE DETECTORS FOR CMB POLARIMETRY AT 100 GHZ

by

Amy E. Lowitz

A dissertation submitted in partial fulfillment of

the requirements for the degree of

Doctor of Philosophy

(Physics)

at the

UNIVERSITY OF WISCONSIN–MADISON

2017

Date of final oral examination: Dec 21, 2016

The dissertation is approved by the following members of the Final Oral Committee:

Peter Timbie, Professor, Physics

Dan McCammon, Professor, Physics

Matthew Bershady, Professor, Astronomy

Mark Rzchowski, Professor, Physics

Kimberly Palladino, Assistant Professor, Physics

ABSTRACT

Kinetic inductance detectors (KIDs) are a promising technology for astronomical observations over a wide range of wavelengths in the mm and submm regime. Simple fabrication, in as little as one lithographic layer, and passive frequency-domain multiplexing, with readout of up to $\sim$1000 pixels on a single line with a single cold amplifier, make KIDs an attractive solution for high pixel-count detector arrays.

Described in this dissertation is the design, fabrication, and testing of a 20-pixel prototype array of kinetic inductance detectors intended for cosmic microwave background (CMB) polarimetry in a band centered at 3 mm (100 GHz), which is an important band for CMB observations from the ground. We first show that the theoretical performance of idealized KIDs rivals that of their primary competitor detector technology, superconducting transition edge sensors (TESs). Next, we describe the design process, which employed both simulation and semianalytic calculations to optimize the resonant frequencies and optical coupling. Where a specific observing scenario was required to motivate design choices, we have used the QUBIC telescope, a bolometric interferometer designed to study the CMB polarization anisotropy initially from Alto Chorillos, Argentina and later from Dome C, Antarctica. Finally, we describe the fabrication and testing of three prototype arrays made with different materials and geometries.

In two iterations of the device geometry, we demonstrate response to mm-wave illumination and improvements in control of pixel center frequencies and coupling quality factors. Additionally, we find that molybdenum is not well-suited to mm-wave KIDs because of excessive thermal dissipation resulting from double-gap behavior of superconducting molybdenum. Titanium nitride trilayers perform better, but exhibit complex and poorly-understood non-Mattis-Bardeen behavior. The superconducting properties of this material will need to be better understood before it can be used in successful mm-wave kinetic inductance detectors.

ACKNOWLEDGMENTS

It is impossible to acknowledge every person without whose input this project would have suffered greatly or failed entirely. I will nonetheless attempt it.

First, I cannot adequately express my gratitude to my advisor, Peter Timbie, for his unending patience and encouragement, from the first day of my graduate career to the last. I am thankful to many others at UW. In particular, I'd like to thank Dan McCammon who taught me most of what I know about practical electronics and who generously loaned key pieces of equipment. I am thankful to all of my lab mates who helped with myriad aspects of this project: Emily Barrentine, Amanda Gault, Chris Anderson, Sara Stanchfield, Catherine Steffel, Brandon Melcher, and Felix Tsao. I am grateful also to the Van der Weide Laboratory for the loan of several essential pieces of equipment, and to Meghan McGarry-Unks and her family for sharing their home with me during my final month of dissertating.

I worked at NASA Goddard Space Flight Center for several months of this project, and I am grateful to many there. I especially want to thank my advisors Thomas Stevenson, Ed Wollack, and Ari Brown, all of whom have been extremely generous with their time and expertise. Kevin Denis, Erik Crowe, Deborah Towner, Manuel Balvin, Vilem Mikula, and Archana Devasia also went above and beyond to help me. Most of the work described in this dissertation was supported by a NASA Office of the Chief Technologist's Space Technology Research Fellowship, without which none of the fabrication or testing would have been possible.

I owe a large debt of thanks to my undergraduate advisor, Ian Dell'Antonio, for guiding me through my first significant solo research project and for years of advice and mentorship during my time at Brown and beyond. Lyman Page took a chance on hiring me as a sophomore undergraduate to work on CMB instrumentation, and the rest (as they say) is history.

Most of the actual writing of this dissertation took place at the Amundsen-Scott South Pole

Station during the austral winter of 2016. The community of scientists and support staff there is unparalleled, and I count myself exceedingly fortunate to have spent a year working among them. I also count myself exceedingly fortunate to have a graduate advisor who barely batted an eye when I decided to disappear to another continent for a year in the middle of dissertating.

Finally, thank you to my friends. Anna Korver and James Hostetter are the best qual study buddies, movie night partners-in-crime, and my-experiment-is-broken commiseraters a gal could ask for. Chris McKenney supplied advice, mentorship, and friendship, and was my long-distance lab partner. To all of my friends and family, thank you for humoring my rants about my broken <fridge/heat switch/detectors/whatever>, for tolerating all the last-minute canceled plans "because I have to babysit the Dewar", and for being categorically awesome.

This dissertation is dedicated to all the CMB photons whose 13.7 billion lightyear journeys have ended in absorption by detectors in CMB instruments. Thanks, guys. It's been real enlightening.

CONTENTS

LIST OF TABLES

LIST OF FIGURES

CHAPTER 1

_____

INTRODUCTION

1.1 A Brief History of CMB Science

For almost as long as there have been humans, they have looked to the sky in an effort to understand their place in the universe. The oldest surviving records of cosmological thought come from the early Mesopotamians and describe a flat, circular Earth embedded in a cosmic ocean. As seafaring and geometry advanced, humanity came to understand that we live on a spherical planet. By the 4th century BC, we had the Aristotelian model: Earth stationary and spherical at the center, orbited by the sun, moon, and naked-eye planets, and surrounded by a series of celestial spheres onto which the stars were affixed. As the centuries wore on, we realized that the Earth is not at the center of the solar system, that the solar system is not at the center of the galaxy, that the galaxy is not at the center of the universe, and indeed that there is no center at all. As our understanding of our place in the present universe has evolved, so has our understanding of the earliest moments of the universe.

In 1922, Alexander Friedmann found an expanding-universe solution to the Einstein equtions, putting one of the first cracks in the foundations of the steady state model [10]. Pondering Friedmann's solution, Belgian priest Georges Lemaître derived in 1927 what would be known as Hubble's law (2 years before Hubble published his famous observational result), and pointed out that an expanding universe would have an origin point in the distant past; a "Big Bang" (though that term was not coined for another 23 years) [11]. Hubble published his pivotal distance vs redshift result in 1929 [12], but there was still a great deal of uncertainty about whether we lived in a steady-state or Big Bang universe.

In 1948, Ralph Alpher and Robert Herman wrote a paper [13] predicting a 5 K cosmic afterglow from the Big Bang, but their work was shortly forgotten. This afterglow, the cosmic microwave

background (CMB), was rederived by Soviet physicist Yakov Zel'Dovich, working behind the iron curtain in the early 1960s, and independently derived by Robert Dicke at around the same time. Dicke, a pioneer in radiometry, set out to make a measurement of the predicted background, but in 1965 Bell Labs scientists Arno Penzias and Robert Wilson stumbled upon the signal with their 15 m radio horn antenna and (ironically) Dicke radiometer, with which they were trying to study satellite communications [14]. 13 years later Penzias and Wilson received a Nobel Prize in physics for their discovery.

Ground-based experiments in the 1980s provided support for the idea that Penzias and Wilson's ~3.5 K background was consistent with the cosmic background radiation expected from a hot big bang, and began to refine the temperature estimate [15]. Results from the COBE satellite [2], launched in 1989, confirmed that the background followed a perfect 2.7 K blackbody spectrum, and put the final nail in coffin for the steady-state model. The COBE PIs, John Mather and George Smoot, were awarded the 2006 Nobel for their work. WMAP, launched in 2001, followed in COBE's footsteps, making more precise measurements of the CMB with much finer angular resolution [3]. In addition to making a finer-grained map of CMB temperature anisotropy, WMAP's angular resolution allowed it to make the first high-quality measurement of the temperature angular power spectrum (see section 1.2 for more detail). WMAP also made the first whole-sky CMB polarization map. The satellite made its final observations in August 2010 and was moved to a graveyard orbit later that year. Meanwhile, the Planck satellite was launched in 2009 and decommissioned in 2013 [16]. Planck made similar measurements to WMAP, but with higher sensitivity and resolution. In addition to refining measurements of many CMB and cosmological parameters, Planck data was key in understanding the 2014 BICEP2 results as a detection of polarizing dust rather than primordial B-modes [17].

1.1.1 Current state of the field

In the more than 50 years since the first CMB measurements, a great deal has been learned. The spectrum points to a Big Bang origin of the universe. The anisotropies provide clues to both
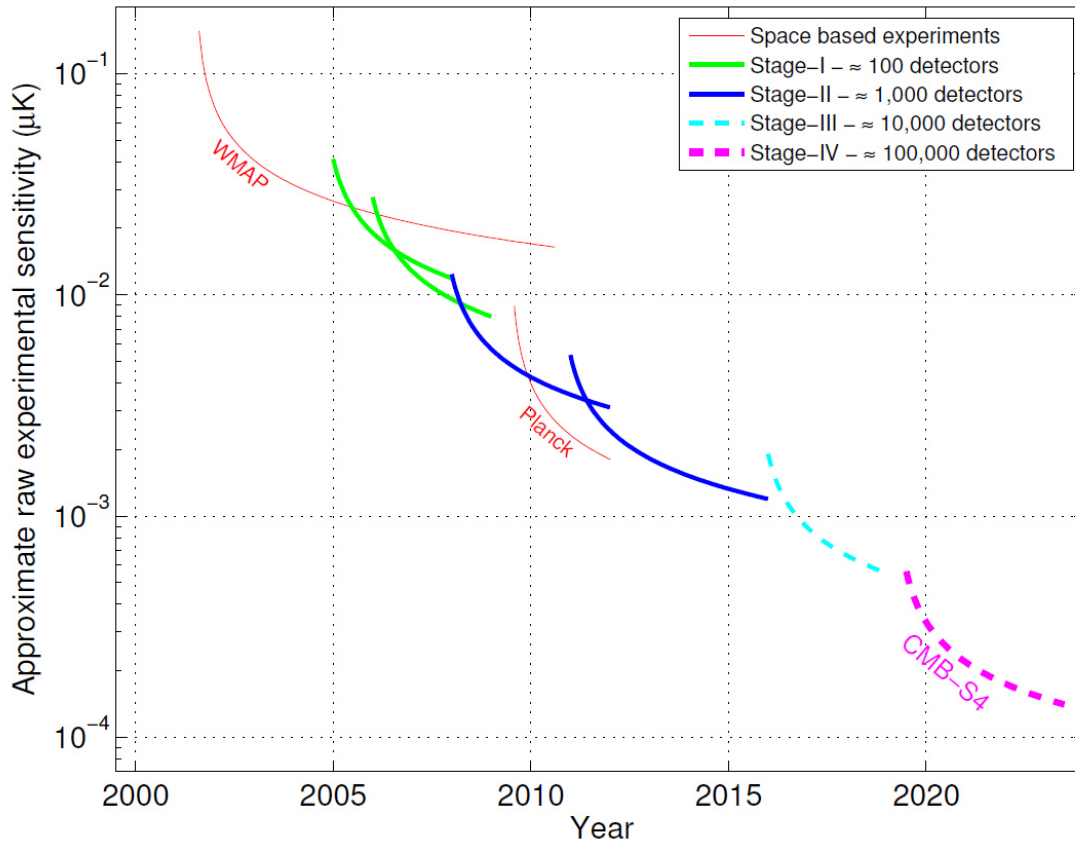
Figure 1.1: CMB experiments' sensitivity over time. Figure from [1].

late-time large structure evolution and also to primordial quantum fluctuations. The scale of the anisotropies also tell us about the composition of the universe and its geometry. Still, open questions remain. Most acute is the question of whether it encodes an imprint of primordial gravitational waves, a 'smoking gun' for inflation. If inflation did happen, what was the spectral tilt? And either way, are there any distortions or deviations from a perfect blackbody spectrum?

CMB research has benefited from a long history of ground-, balloon-, and space- based instruments, from Penzias and Wilson's 15 meter horn antenna in the 1960s, to the Soviet single-detector RELIKT-1 satellite in the early 1980s, to current instruments with over 10,000 detectors. CMB instruments have advanced roughly in three (soon to be four) stages, with an order-of-magnitude jump in detector-count with each stage (see figure 1.1).

Presently, the first 'stage 3' instruments are being deployed or processing their first data sets

taken with arrays of $\mathcal{O}(10,000)$ detectors. BICEP was upgraded from version 2 to 3 last year, and the Keck array will be upgraded to the BICEP Array in ~2018, with a total of about 30,000 detectors between the two instruments. The South Pole Telescope is currently being upgraded from ~1500 detectors to ~ 15,000 detectors. When the full six-module QUBIC instrument is deployed, it will have over 12,000 detectors. Several other current ground-based instruments have recently upgraded or have near-term plans to upgrade from stage 2 to stage 3 instruments, including ACT and POLARBEAR.

One of the most recent major results is the 2015 joint BICEP2/Keck/Planck analysis. The results presented in their paper [17] are especially interesting because they combine the most recent data from the most sensitive CMB satellite with two of the most sensitive ground-based CMB telescopes. BICEP2 and Keck together reach a depth of 57 nK deg in Stokes Q and U at 150 GHz, while Planck alone reached only 1.2 μK deg in Q and U at 143 GHz, but observed seven different frequencies. The 2015 Planck results [16,18] on their own offer the most sensitive constraints yet on a number of cosmological parameters of interest, including the sum of the neutrino masses (< 0.23 eV), the effective number of neutrinos (3.046), the Hubble constant (67.8 ± 0.9 km s^{-1}Mpc^{-1}), scalar spectral index (n_s=0.968 $\pm$ 0.006), and others.

1.1.2   Future outlook

Looking forward, the CMB community is preparing to design and build a 'stage 4' (S4) instrument. This instrument will represent a pooling of funding and other resources from all of the major North American CMB research groups into a single project with multiple telescopes in both the northern and southern hemispheres and roughly 500,000 detectors in total. It will represent a significant stride towards the limits of what can be achieved with observations from the ground, with a target tensor-to-scalar ratio sensitivity of σ(r)=0.0005, roughly an order of magnitude improvement over stage 3 instruments. The present goal of inflation research in the CMB field is to measure the tensor to scalar ratio, so-called 'little r', a measure of inflation, or to push the upper bound down to the limits of detectability and below the bounds of what can be described by reasonable slow-roll

inflation models.

1.1.2.1 Beyond little r

If r is measured, the next frontier in the field will be to measure the most detailed possible whole-sky primordial B-mode statistics in an effort to measure the spectral tilt of inflation, commonly called 'n_T'. In parallel with these efforts, instrument sensitivity is now reaching a level where small distortions in the CMB blackbody spectrum may be measurable. Some early-stage efforts are in discussion to measure these small 'wiggles' in the otherwise-perfect blackbody spectrum, which are expected to arise from free-bound transitions during reionization [19].

1.2 CMB Cosmology

The most fundamental principle which governs our understanding of the universe and our place in it is the Cosmological Principle. Simply put, we believe that the universe is both homogeneous and isotropic; that there is no preferred direction nor any preferred point in the universe. While this is distinctly untrue on local scales (Earth's gravitational field, for instance, defines a local preferred direction, and this very dissertation, especially if you are reading it in hard copy, represents a significant local inhomogeneity), on scales the size of galaxy clusters and larger, observations have so far borne out the Cosmological Principle. Our place in the larger universe is utterly un-special, and as far as we can tell so is every other place.

As predicted by Alpher, Herman, Gamow, Zel'dovitch, and Dicke, the universe today is permeated by microwave radiation at a temperature of 2.7 K, almost perfectly isotropic down to 1 part in 10^5. The early universe was an extremely hot and dense plasma of photons, electrons, and protons. For the first 380,000 years, the universe was too hot to form neutral hydrogen and the photons and matter were tightly coupled via frequent Thomson scattering of photons with the free electrons. Since the ion density in this epoch was very high, the mean free path of photons was very short, making the universe essentially opaque. As the universe expanded and cooled, eventually temperatures were

low enough to allow for formation of neutral hydrogen. At that time, about 380,000 years after the Big Bang or at z≈1100, the universe went rapidly from being highly ionized to being almost entirely neutral. The photons, no longer having free electrons to scatter off of, decoupled from the matter and the universe became mostly transparent. When we image the microwave sky, we see a 'wall' far away (and therefore also in the distant past) where the universe transitions from being mostly transparent to being mostly opaque. This so-called 'surface of last scattering' is effectively an image of what the universe looked like when the primordial photons scattered one final time before the universe became neutral. Since that time, CMB photons have propagated largely unscattered, except for small perturbations by foreground structure.

Today, we observe an isotropic background of 2.7 K blackbody radiation (see figure 1.2) mottled with small anisotropies of one part in 10^5. These slight hot and cold spots originate from random quantum fluctuations in the primordial universe and represent slight under- and over- densities in the primordial soup at the time of recombination. Over billions of years, the over- and under-densities were amplified by gravitational infall and eventually formed the large-scale structure which spans the universe today. The angular scale of the anisotropies arise from the propagation of acoustic waves in the primordial universe. In the early universe, the interplay between radiation pressure and gravitational infall produced acoustic waves which permeated primordial space. The propagation speed of these acoustic oscillations (and therefore their size on the sky today) is set by the energy density and expansion history of the universe. When matter and radiation decoupled during recombination, the patterns of these waves were 'frozen in' to the CMB photons and can now be seen in measurements of the microwave sky. A convenient way to represent the acoustic waves' imprint on the CMB is to represent the pattern on the sky as a superposition of spherical harmonics. Then we can graph the 'angular power spectrum' by calculating the relative amount of power in each multipole moment. That the first peak in the angular power spectrum (see figure 1.3) falls at one-degree scales (ℓ=200) indicates that we live in a flat universe. The height of the second peak indicates the fraction of the energy density attributable to baryons.

Cosmic microwave background measurements are a rich probe of a variety of interesting and important parameters, most of which can be determined from the angular power spectrum. The
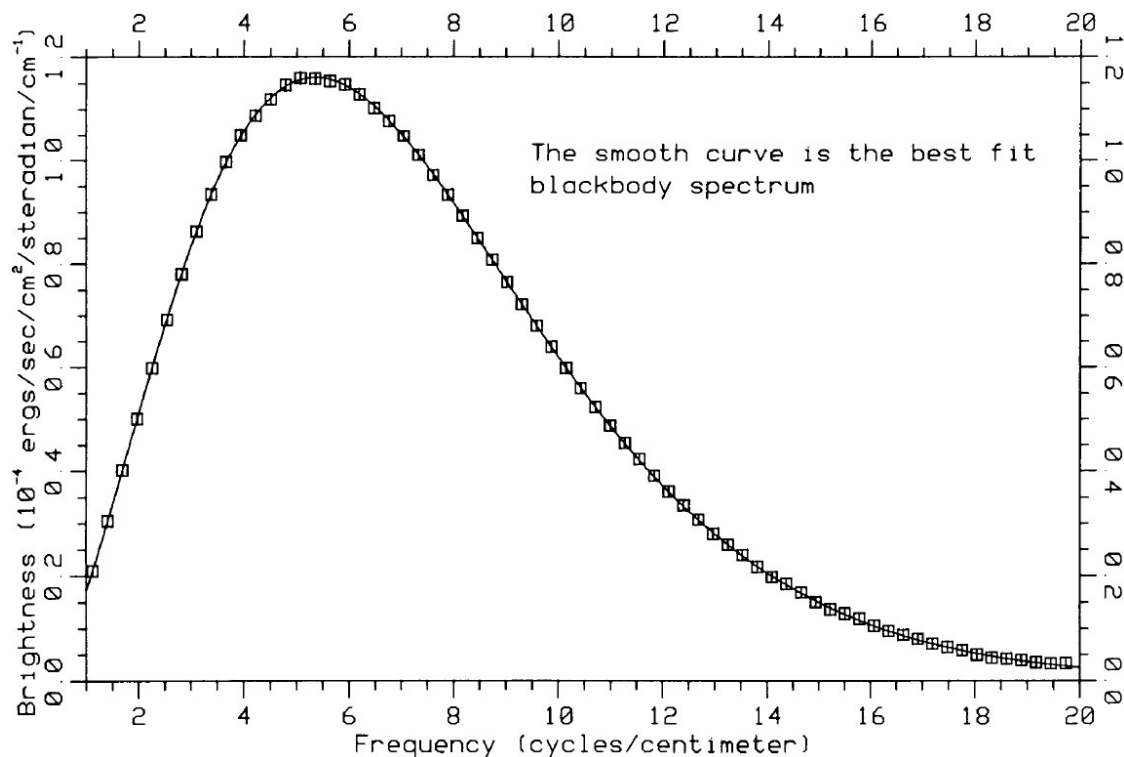
Figure 1.2: CMB blackbody spectrum as measured by FIRAS on the COBE satellite [2].

CMB offers a window into the details of primordial inflation, neutrino number and mass, dark matter, and dark energy.

1.3   Inflation

The discovery of the CMB put the final nail in the coffin of the steady state model of the universe, proving we live in a Big Bang universe. However, in answering one question, it left several more. Three 'paradoxes' soon became apparent. First, the 'horizon problem.' In the standard Big Bang model, the sky we see today is made up of many patches that were never in causal contact, so how could it be that the whole CMB, on the whole sky, is 2.73 K, with temperature variations of only 1 part in 10^5? Second, the 'monopole problem.' The existence of magnetic monopoles is suggested by (among other things) the structure of Maxwell's equations and the need for a monopole to set the size of electrical charge quanta (there is a formulation of electromagnetic theory which does not
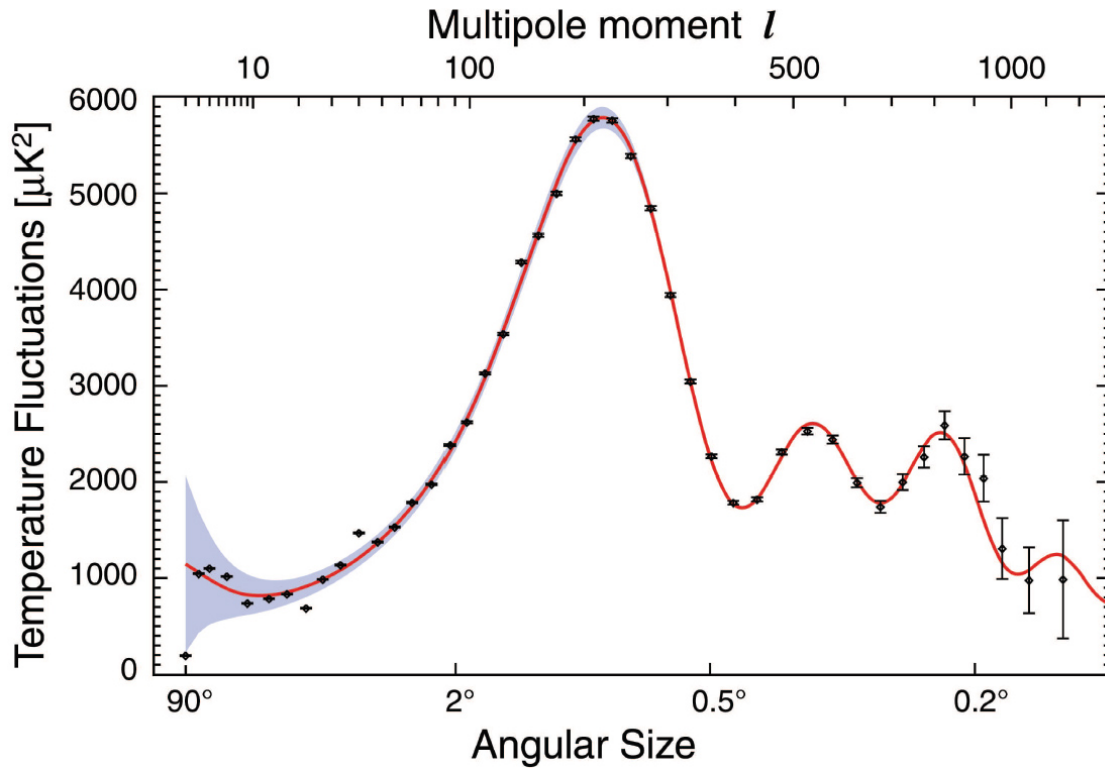
Figure 1.3: CMB temperature angular power spectrum from the WMAP 7-year data [3].

require magnetic monopoles to set the electric charge quantum, however monopoles are a *result* of this formulation anyway). Simple grand unified models predict monopole densities roughly 14 orders of magnitude greater than the current upper bound [20]. Despite the apparent theoretical need for magnetic monopoles, none have been detected; yet there was no compelling explanation for their scarcity. Third, the 'flatness problem.' Measurements of the angular power spectrum of the CMB indicate that the universe is perfectly flat, to within the uncertainty in the measurement, but to have a curvature of precisely zero is incredibly specific and presents a fine-tuning problem. In 1980, Alan Guth proposed a solution: inflation [20].

Inflation in this context refers to a very brief period in the very early universe, about $10^{-32} - 10^{-34}$ s after the Big Bang, during which the universe underwent extremely rapid expansion. During the roughly 10^{-32} s that inflation is believed to have lasted, the universe may have expanded by a factor of roughly 10^{26}. This brief, rapid expansion offers explanations for all three of the 'paradoxes.' Guth's model allows for a small, causally connected universe prior to the moment of inflation. In

the moment of inflation, formerly small regions of space rapidly expanded far beyond the horizon size of the early universe. Any inhomogeneities or curvature would have been smoothed out, and any monopoles would be widely dispersed, thus eliminating all three 'paradoxes'. In this model, quantum fluctuations in the pre-inflation universe were blown up by inflation into the small-scale anisotropies seen in the CMB and which were later amplified by gravitational infall to form the large-scale structure of the universe.

While inflation is largely accepted as the best idea so far of how to resolve these paradoxes, it has yet to be confirmed. There are, however, testable predictions which can be derived from the inflation hypothesis. Chief among these is the B-mode anisotropy. Light from the CMB is slightly polarized and that polarization is slightly anisotropic. One way to consider the polarization field on the sky is to decompose it into two components: E-modes, which are curl-less, and B-modes, which are divergence-less, so-named because of their visual and mathematical similarities to electric and magnetic fields. E-modes are primarily interesting because of the information about gravitational lensing that they can encode, but when it comes to inflation, B-modes are the focus. There are relatively few ways to cause B-mode polarization in the CMB. Late-time lensing can twist E-modes into B-modes, but this effect only affects relatively small angular scales since the lensing masses themselves are small in angular scale. B-mode polarization can also arise from dust and synchrotron radiation coming from our own galaxy. Since we have such a close-up view, these effects can appear on large angular scales, but have a distinctive spectral shape which allows them to be 'cleaned' from CMB maps if there is enough data available at a variety of wavelengths. The only other significant source of large-scale B-mode anisotropies is the imprint that would have been left on the CMB by inflation. Polarization in the CMB results from Thomson scattering during the epoch of recombination [21, 22]. Such scattering events in an isotropic medium would not result in polarized light, however random fluctuations in the density of the primordial plasma during the epoch of recombination set up quadrupole moments of hot and cold spots (over-dense and under-dense regions) which allowed the Thomson scattering to produce slight linear polarization. In particular, tensor perturbations seeded by inflation produce gravitational waves which stretch space in one direction and squeeze it in the orthogonal direction, giving rise to both E-mode and

B-mode polarization-producing quadrupole moments. Also important, though less interesting for inflation, are scalar perturbations, which produce over- and under- densities in the primordial plasma and produce E-mode polarization. It is a detection of these B-modes anisotropies from the tensor fluctuations, i.e. a measurement of the tensor-to-scalar ratio – 'little r', which is sought as a 'smoking gun' for inflation and a unique probe of physics at the extraordinary energy scale of inflation [21–23].

1.4 Other CMB observables

1.4.1 Dark matter

From the CMB temperature angular power spectrum we know the total matter content, the baryon content of the universe, and that dark matter makes up about 85% of the matter in the universe. Even though we don't know what sort of particle(s) it is made of, we know it must exist based on observations of galaxy rotation curves and gravitational lensing measurements. Weakly interacting massive particles (WIMPs) are the most well-studied candidate particle for dark matter, and many experiments are purpose-built to detect them. Some WIMP models allow for annihilation of dark matter particles into standard model particles. This process slightly distorts the CMB power spectrum [21, 23–25], which makes the CMB a useful probe of these processes. Planck has ruled out WIMP masses below 16GeV and CMB-S4 could probe WIMP masses two or three times higher [23]. Precise measurements of the CMB temperature and polarization power spectra can also constrain models for axion dark matter, an alternative to WIMPs [23].

1.4.2 Dark energy

Dark energy, or the cosmological constant, is an energy density which permeates all of space. Though it is poorly-understood, it is estimated to make up nearly 70% of the total energy density in the universe. Proposed as an explanation for the accelerating expansion of the universe discovered using

type 1a supernova observations in the 1990s, dark energy is presently the most widely-accepted possible explanation for this phenomenon. Understanding the reason for the accelerating expansion of the universe is critically important to forming a complete picture of the fundamental laws governing the evolution of the universe, and CMB probes of dark energy offer an important avenue towards greater understanding of dark energy phenomena. The thermal Sunyaev-Zel'dovich (SZ) effect, which refers to late-time distortions of the CMB resulting from inverse-Compton scattering of CMB photons off of hot gas in foreground masses, offers one method of probing dark energy using CMB measurements. The SZ effect can be used to determine the abundance of galaxy clusters as a function of redshift. Because the accelerated expansion affects the growth of cosmic structure, the cluster abundance and mass function is very sensitive to dark energy parameters [26], but these measurements require a good understanding of cluster masses; SZ surveys are the most efficient approach to studying massive clusters at z>1, while optical surveys provide the best probe of these clusters at lower redshifts [23]. In addition, the kinetic SZ effect is useful in constraining certain parameters which are important for breaking degeneracies between different ΛCDM models [27]. The kinetic SZ effect is similar to the thermal SZ effect except the distortions in the CMB arise from interactions with foreground matter that has high energy primarily due to its motion instead of primarily due to its temperature; the relative motion of a cluster relative to the CMB causes a Doppler effect which produces spectral distortions.

1.4.3   Neutrino number and mass

Neutrinos are the lightest of the standard model particles. They have the second-highest number density of any species in the universe (after the CMB photons), and aided by their mass have energy density at least 25 times that of the CMB today [1]. Because of their extremely small but non-zero mass, they have both radiation-like and matter-like properties which leave unique imprints in the CMB which can be used to constrain N_{eff}, the effective number of neutrino species, and Σm_ν, the sum of the neutrino masses. The number of neutrino species alters the photon diffusion scale relative to the sound horizon in the CMB, which can be observed as a suppression of power at

small angular scales and a shift in the location of acoustic peaks in the angular power spectrum, respectively [1]. The sum of the neutrino masses also affects the observable CMB. Deviations in Σm_ν would affect the CMB temperature and polarization via the integrated Sachs-Wolfe effect and via gravitational lensing by large scale structure [1, 28].

1.5 Measurement Efforts and Challenges

The primordial B-mode anisotropy is expected to be on the order of a few nanoKelvin. Compared to the several μK of the temperature anisotropy, this constitutes a significant measurement challenge.

In 2014, BICEP2 detected a B-mode anisotropy on large (degree) angular scales [29]. With the limited foreground data available at the time, they believed the detection could have been primordial B-modes. However when better foreground data at other wavelengths from Planck became available, it became apparent that their detection was within the bounds of what could be explained by polarization from foreground dust. A joint analysis of the Planck and BICEP2 data [17] placed a 95% CL upper limit on r of 0.12, with 7.0σ significance in their detection of lensing B-modes. The joint analysis puts the most likely value of r at about 0.05, but r=0 cannot be excluded with significance.

The dust confusion of the 2014 BICEP2 result emphasizes the importance of measuring the CMB at multiple wavelengths as an assurance against confounding variables. Measuring the same patch of sky at multiple wavelengths allows for improved foreground subtraction because polarizing foregrounds produce signals with a different spectral shape than the primordial signal.

To achieve the sensitivity required for detection and mapping of the primordial B-mode signal, future instruments will require on the order of 10^5 detectors across several wavelengths. The focal planes for these instruments will be a significant driver of the total cost and the primary driver of the ultimate experimental sensitivity. Therefore, the need for well-understood, inexpensive, high-yield, background-limited, scalable detectors at CMB frequencies is acute. As the Snowmass CF5 Neutrino Planning Document [1] puts it, "scaling is the primary technical challenge of CMB-S4"; to achieve the sub-μK-arcmin sensitivity goal for a stage four CMB instrument will require about 500,000

detectors.

Transition edge sensors (TESs) are well-understood and nearly background limited, and have been the leading-edge technology for CMB detectors for more than 15 years. However, because of their complex, many-layered fabrication requirements, many readout wires per detector, and need for SQUID (superconducting quantum interference device) amplifiers, their yield, scalability, and cost are suboptimal when facing the prospect of producing such a large number of detectors. Kinetic inductance detectors (KIDs) are a newer technology and therefore less well-understood, but they potentially offer equal or better sensitivity, higher yield at a lower cost, and greater scalability compared to the best TESs currently available. Study of KIDs at CMB frequencies, therefore, is important in the push towards higher detector-counts in future CMB instruments.

1.6   Thesis Summary

In the chapters that follow, I will provide theoretical and practical motivation for the detector designs described, outline the fabrication and testing process, and discuss the measurements made and the conclusions that can be drawn from them. Chapter one has provided a background in the relevant cosmology and has motivated the need for high-yield, scalable, inexpensive microwave detectors. Chapter two will discuss the theory and operational principles of both kinetic inductance detectors and their primary competitor, transition edge sensors, and will compare the theoretical best-case performance of these two detector styles. Chapter three describes the QUBIC telescope, which motivated some of the detector design choices. Chapter four discusses the design process including the simulations and calculations that informed the final chip geometry, as well as a discussion of material choices. In chapter five, I explain the fabrication processes used to produce the detectors. Chapters six and seven describe the testing apparatus and measurements. Finally, conclusions and suggestions for future work are presented in chapter 8. The appendices are directed primarily at any future graduate student trying to replicate this work on the same apparatus; a cryostat pinout and cooldown procedure are provided as well a schematic for using the IQ demodulator to make noise measurements and a summary of all of the runsheets used in the wafer fabrication process.

All of the design, fabrication, testing, and analysis described herein is my own work, except in a few cases where contributions by others are specifically noted in the text.

CHAPTER 2

———

DETECTORS

2.1 A Brief History of Light Detection

Strictly speaking, humans have been detecting visible light for as long as they've been able to see. We've been detecting ultraviolet light for as long as we've suffered from sunburns. We've been detecting visible and infrared light for as long as we've felt the warmth from the sun or from a fire. Our plant and cyanobacteria cousins have been photosynthesizing for at least 2.3 billion years. Detecting light outside of the IR-UV range, or using chemicals or electronics to detect any frequency of light took quite a lot longer to achieve.

Human-engineered recording of light by chemical means dates to the mid-1820s, to a crude camera and film developed by Nicéphore Niépce. The earliest surviving example of his work dates to 1826 or 1827, and was a crude pewter photographic plate treated with a photosensitive naturally-occurring asphalt exposed over the course of several days and developed with a mixture of lavender oil and mineral spirits [30].

Almost as soon as the photographic process was invented, early photographers turned their cameras to the skies. In the 1830s, Louis Daguerre invented the daguerreotype, which used sheets of coppper coated in silver iodide as photographic plates. The plates were developed by exposing them to mercury vapor and fixed with salt water or, later, sodium thiosulphate [30]. By the late 1930s, Daguerre was experimenting with making daguerreotypes of the moon, though the first success wasn't until March 1840, by John William Draper, using a 13 cm reflector and 20 minute exposure. The first stellar photography was by George Phillips Bond, in 1857, of the double star Mizar and Alcor, and thus was astrophotography born [30, 31].

The first human-engineered recording of light far outside the visible spectrum was in the mid-1890s when Wilhelm Röntgen began recording X-ray shadows on photographic plates [31]. While the

CCD, useful in astrophotography from the x-ray to the infrared, wasn't invented until the late 1960s at Bell labs by Willard Boyle and George Smith [31], early 'electronic' light detection technology began even earlier. The transition edge sensor (TES) was invented in the 1940s, just 30 years after Onnes's discovery of superconductivity [32]. Originally used for infrared imaging, today TESs are useful across the spectrum from microwave to x-ray frequencies.

2.2 Low Temperature Detectors

The earliest bolometers date to the 1880s, and were invented by Samuel Langley who used them to measure infrared light from the sun [33, 34]. By the mid 1930s Simon and Karti were cooling thermal detectors to 50 mK to improve their sensitivity [35] following the suggestion by Francis Simon in 1935 [34, 36]. In the early 1940s, DH Andrews invented the first *fundamentally* cryogenic detector, the superconducting transition edge sensor [32].

Perhaps the largest class of cryogenic detectors in common use today is the bolometer. Broadly, a bolometer consists of an absorber weakly coupled to a cold bath. A sensitive thermometer monitors the temperature of the absorber and any change in temperature can be mapped to an incident power. The chief difference between different types of bolometer is the type of thermometer used to monitor the absorber temperature. Common thermometers for this purpose are doped semiconductors, superconductors (bolometer using superconductor thermometers are commonly called transition edge sensors, see section 2.5), and metallic paramagnets [34]. Another class of cryogenic detectors is the pair-breaking detector, including superconducting tunnel junctions and kinetic inductance detectors, which are the primary focus of this document and are discussed in detail in the sections and chapters that follow.

2.3 Kinetic Inductance Detectors

Kinetic inductance detectors (KIDs) were invented at Caltech and JPL in the early 2000s, primarily by Ben Mazin, Jonas Zmuidzinas, Peter Day, and Rick Leduc. The earliest and most basic designs
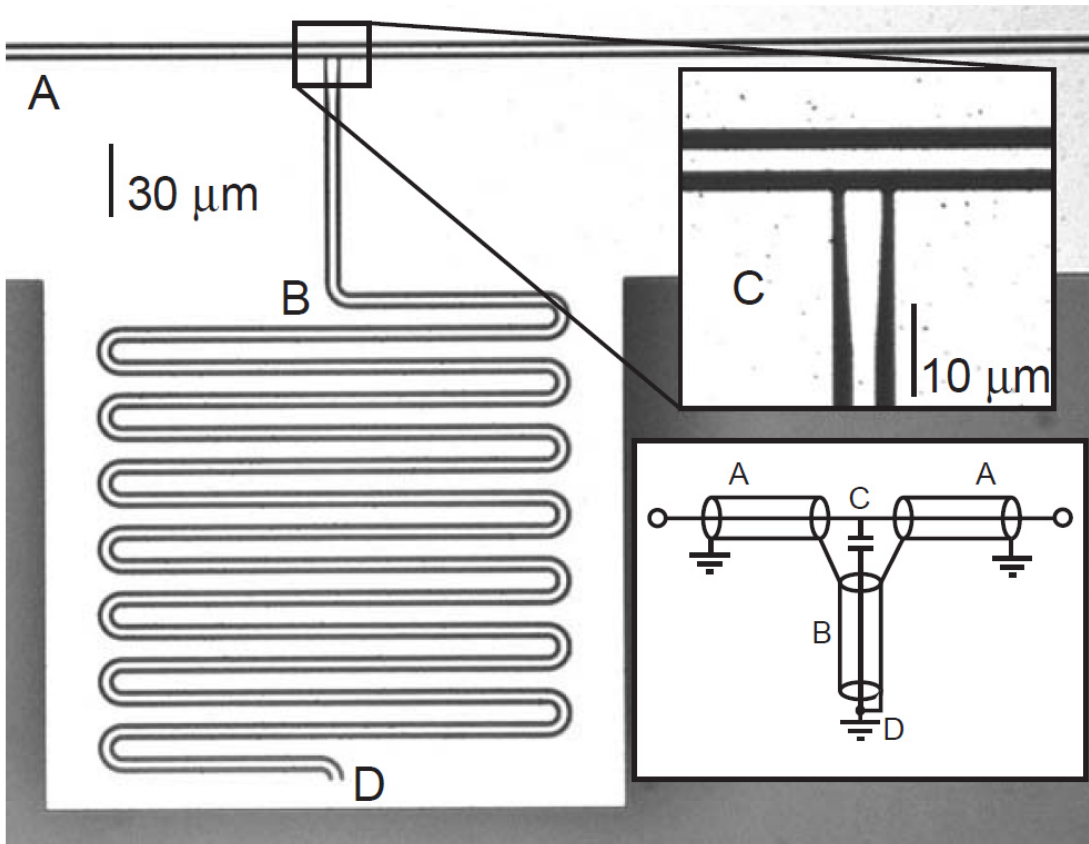
Figure 2.1: Micrograph of Ben Mazin's CPW quarterwave distributed KID (left and inset). Schematic of the an equivalent circuit (right). Figure adapted from [4].

consist of a planar distributed superconducting resonator circuit weakly coupled to a microstrip or coplanar waveguide (CPW) transmission line (see figure 2.1). In early designs, the resonator would be tuned to a resonant frequency in the low GHz range. A band of frequencies is passed through the transmission line and the on-resonance energy is dissipated in the weakly-coupled resonator producing a resonant 'dip' in the output of the transmission line at the resonator frequency. Incident photons of sufficient energy can break Cooper pairs in the resonator resonator, which slightly affects the resonance of the microwave circuit. This perturbation of the resonance can be read out by measuring the change in position and depth of the resonant dip on the transmission line output.

To develop the design principles of kinetic inductance detectors requires an understanding of a number of aspects of superconductivity and microwave engineering which are outlined in the sections that follow.

2.4   Superconductivity

Discovered in 1911 by Kamerlingh Onnes when he noted the absence of electrical resistivity in sufficiently cold mercury samples [37], superconductivity is a phenomenon occurring in certain metals and ceramics wherein the material loses all DC electrical resistivity below a certain characteristic 'critical temperature,' T_c. In addition to perfect DC conductivity, another hallmark of superconductivity is perfect diamagnetism (in bulk samples) [38, 39]. On a microscopic level, when a material becomes superconducting, the conduction electrons form Cooper pairs, bound by a weak attractive interaction mediated by the electron-phonon interaction. These Cooper pairs all live in the ground state, separated from the conduction band by a gap energy, 2Δ. In a normal metal, most of the electrical resistance arises from scattering events of the conduction electrons with vibrations, impurities, and defects in the lattice. However these scattering events have energy scales smaller than the superconducting gap energy, so for electrons bound in Cooper pairs, there are no available energy states for them to scatter into. Therefore they propagate ballistically without scattering and without resistive losses.

For bath temperatures well below the superconducting critical temperature, the gap energy is roughly

$$2\Delta = 3.528 k T_c. \tag{2.1}$$

Δ is nearly constant until a significant fraction of the conduction electrons have been thermally excited over the superconducting gap into unbound 'quasiparticles'. In the limit where $T \to T_c$, $\Delta \to 0$ and the material ceases to be superconducting since there is no longer an energy gap. For bath temperatures near the critical temperature, the gap energy can be estimated as follows [38]:

$$\Delta_T \approx 1.74 \Delta_0 \left(1 - \frac{T}{T_c}\right)^{1/2} \tag{2.2}$$

where Δ_T is the gap at a particular temperature, T, and Δ_0 is the gap energy at $T = 0$.

Superconductivity is a fundamentally non-local effect. Paired electrons propagate separated

by a characteristic coherence length. On length scales smaller than the coherence length, contact with other metals allows for 'sharing' of superconducting properties [40, 41]. This phenomenon, called the proximity effect, can be exploited to 'tune' the critical temperature of a superconducting structure by making it out of thin layers of materials with properties close to the desired final material characteristics [42, 43].

2.4.0.1 Kinetic inductance

In general, inductance is the tendency for a circuit to resist changes in current. A change in current induces a proportional response in the voltage across the inductor, and the constant of proportionality is the inductance, L. Typically, we only deal with magnetic inductance, L_m, which is associated with the energy of the magnetic field that arises from a flowing current and the voltage induced in nearby conductors by a time-varying magnetic field. In most cases, kinetic inductance, L_k, which arises from the translational kinetic energy of charge carriers of finite mass, can be neglected because their energy is quickly dissipated via collisions. However, in high carrier mobility conductors and at very high frequencies, the contribution from kinetic inductance becomes important.

Consider a wire of cross-sectional area A, with charge carriers of mass m and charge e with number density n_c and average velocity v. The current flowing through the wire is $I = An_c ev$ or, rearranging, the average velocity of the charge carriers is $v = \frac{I}{An_c e}$. The total mass of the charge carriers in a given length, l, of such a wire is $M = mn_c Al$. Thus the total kinetic energy of all of the charge carriers in a length, l, of wire is $E = \frac{1}{2}Mv^2 = \frac{1}{2}(mn_c Al)\left(\frac{I}{An_c e}\right)^2$. Rearranging, we see that

$$E = \frac{1}{2}\left(\frac{lm}{An_c e^2}\right)I^2. \tag{2.3}$$

Recall that the energy stored in an inductor is in general

$$E_L = \frac{1}{2}LI^2. \tag{2.4}$$

Comparing equations 2.3 and 2.4, it is clear that the factor $\frac{lm}{An_c e^2}$ is an inductance arising from the

kinetic energy of the charge carriers - the kinetic inductance.

2.4.0.2   Kinetic inductance detectors

Because of the high carrier mobility in superconductors, the kinetic inductance can make a significant contribution to the total inductance of a superconducting circuit. In a superconductor, the charge carrier is a Cooper pair, with mass $2m_e$, twice the mass of an electron, and charge $2e$, twice the charge of an electron. The sheet resistance, neglecting second-order effects for very thin films, is $R_s = \frac{\rho}{t}$ where ρ is the bulk resistivity and t is the film thickness. Then the kinetic inductance per square of a superconducting film is

$$L_k/\square = \frac{R_s}{\rho} \frac{m_e}{2n_{cp}e^2} \tag{2.5}$$

where n_{cp} is the number density of Cooper pairs. The kinetic inductance increases as the carrier density decreases.

In a kinetic inductance detector (KID), a resonant LC circuit is made of a superconducting film. Photons with energy $h\nu \geq 2\Delta$ can excite Cooper pairs into quasiparticles, decreasing the carrier density, which increases the kinetic inductance, decreasing the resonant frequency, f_{res} of the circuit. The change in frequency is monitored by passing a band of frequencies around f_{res} through a transmission line weakly coupled to the resonant circuit. Similarly, increased quasiparticle density causes increased dissipation in the resonant circuit, which can also be measured. See figure 2.2 for schematics of Cooper pair breaking in a KID and frequency and dissipation readout.

The primary competitor technology for KIDs are TESs (see section 2.5). While TESs are a more established, well-understood technology, KIDs offer advantages in several areas. Most importantly, multiplexing for TESs is somewhat cumbersome. Multistage SQUID (superconducting quantum interference device) amplifier schemes currently offer multiplexing factors up to 32 X, but SQUIDs are expensive and offer their own set of technical challenges, and even with 32x multiplexing, for very high pixel-count arrays the number of wires required is still cumbersome. KIDs, on the other hand, lend themselves naturally to passive frequency domain multiplexing. Each KID resonator is
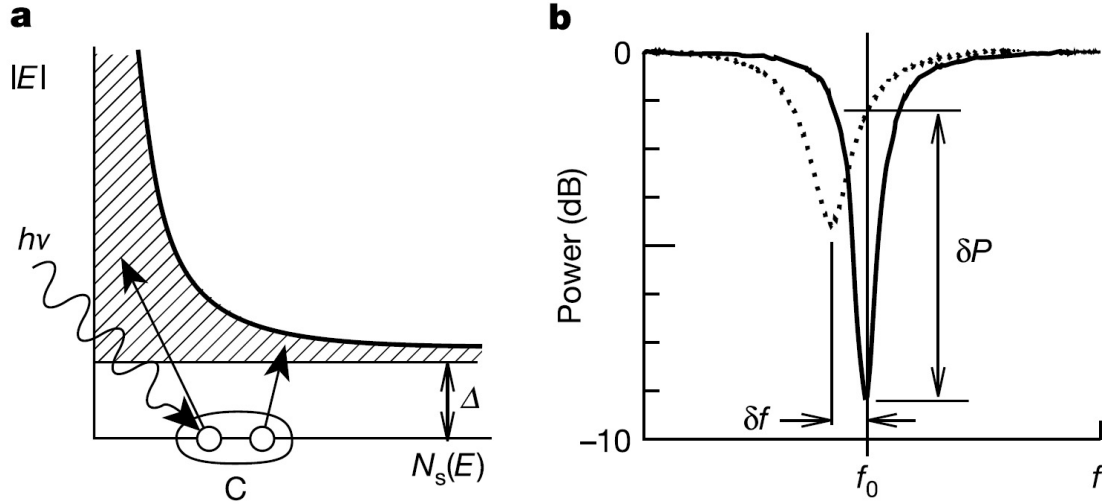
Figure 2.2: **a)** Schematic of Cooper pair breaking in a KID. Photons with energy greater than the superconducting gap energy can break Cooper pairs, exciting them into two quasiparticles. **b)** Schematic of readout for a single KID resonator. When illuminated, the resonance shifts to lower frequency and increased dissipation (lower resonator quality factor, shallower resonance). Figure adapted from [5].

tuned to a slightly different resonant frequency and the weakly-coupled transmission line carries the whole band spanning from the lowest to the highest frequency resonator, producing a comb of resonances at the output (see figure 2.3). If the resonators are spaced far enough apart in the frequency domain (at least several times the FWHM of the resonance), they can all respond independently to illumination without running together (though crosstalk is an ongoing challenge for certain KID designs, as discussed further in section 2.7). Up to ∼2000 KID resonators can be read out on a single line with a single cold amplifier. KIDs also benefit from simpler fabrication than TESs for typical designs. Science-grade KIDs can be made with as little as a single layer of lithography. The design described in this dissertation has four layers of lithography, only two of which are critical for operation. TES designs typically have at least ten layers of lithography usually including thin, micromachined thermal isolation structures and often with much smaller minimum feature-sizes than comparable KIDs, all of which make TESs more difficult and more expensive to fabricate and make producing high-yield arrays much more challenging compared to KIDs.
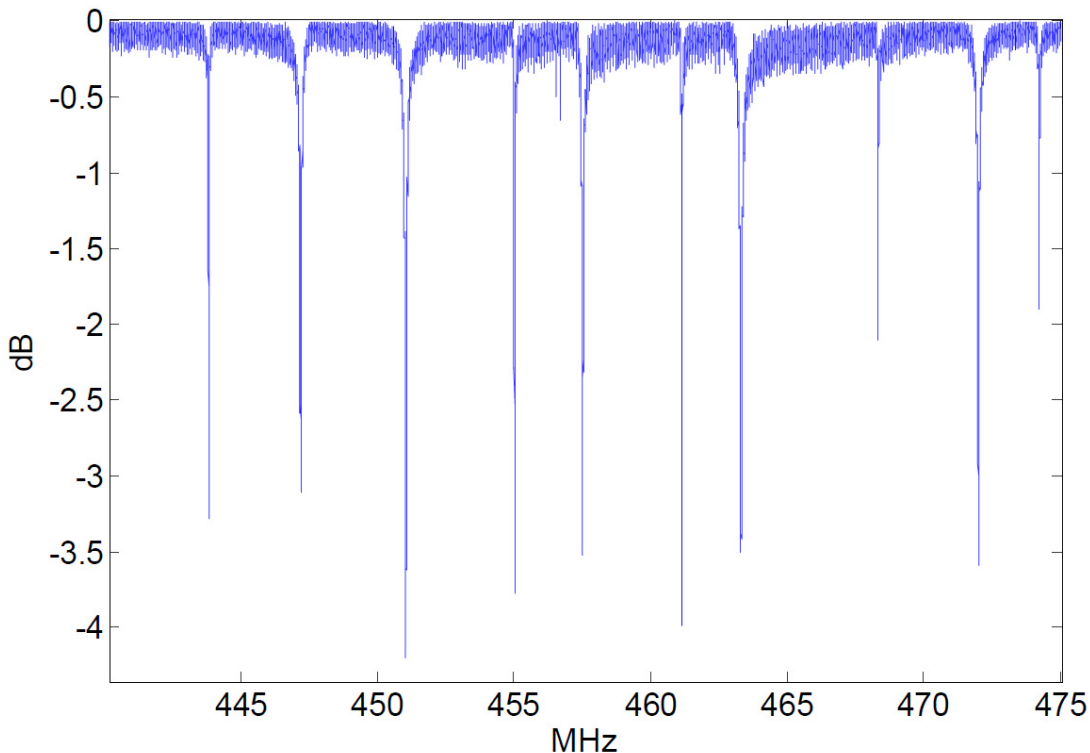
Figure 2.3: Comb of frequency-domain miltiplexed KID resonators.

2.5   TESs

Transition edge sensors (TESs) are the leading detector technology currently used in CMB instruments. Invented in the 1940s by D.H. Andrews using a fine tantalum wire held at 3 K [32], today they offer nearly background-limited sensitivity from microwave to X-ray frequencies. The general principle of operation is as follows:

Light impinges on an absorbing material which heats up slightly in response to the incident photon power. Tightly thermally coupled to the absorber is a small piece of superconducting material which is electrically biased such that it sits exactly at its superconducting critical temperature, near the middle of the steep slope on the R vs T curve (see figure 2.4). Small changes in temperature produce large changes in resistance, allowing the superconducting material to act as a highly sensitive thermometer. To provide a sink for the incident power, the superconductor/absorber system is
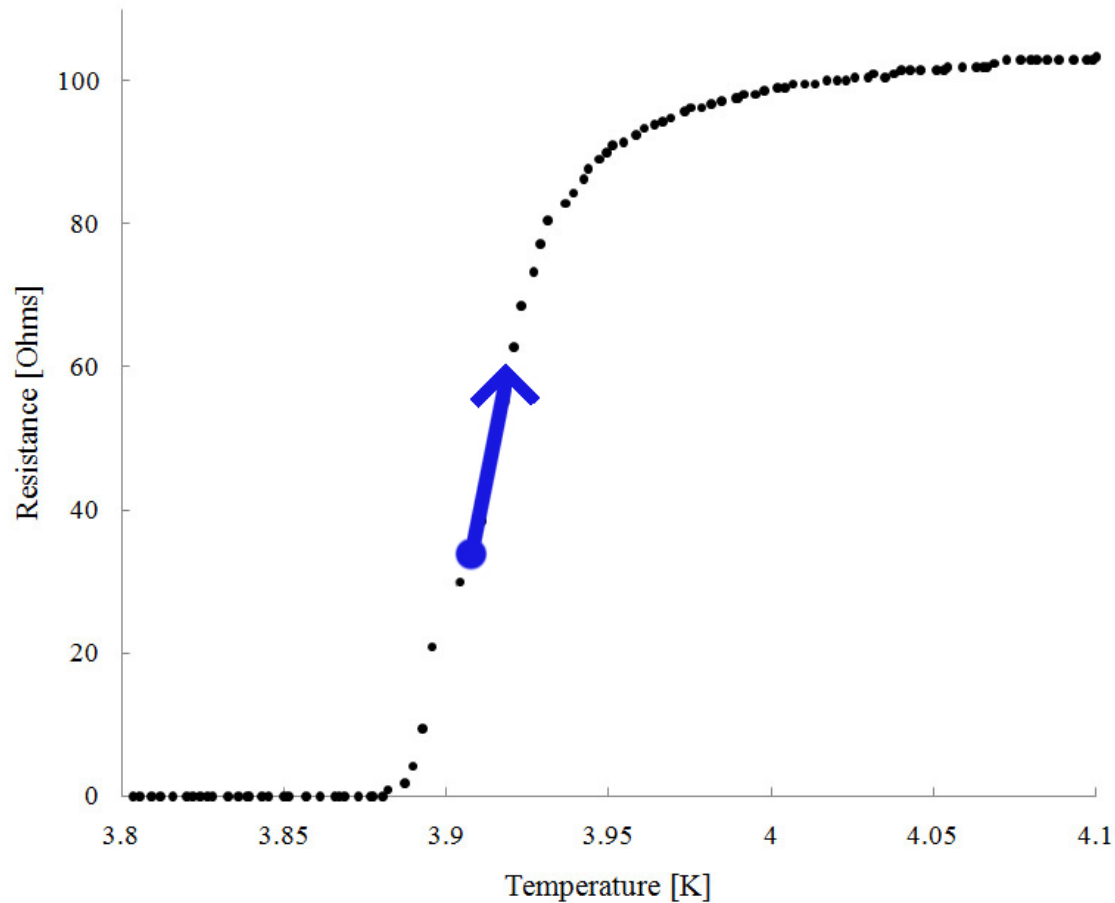
Figure 2.4: Superconducting transition of a titanium nitride sample (small black dots are measured data points). The overlayed arrow indicates the operational principle of a TES; the TES is electrically biased so that it sits near the middle of the superconducting transition (large blue dot). Any incident power produces a small change in temperature which precipitates a large change in resistance (blue arrow).

connected by a weak link to a cold bath well below the superconductor's critical temperature. The resistance of the superconducting material is read out using a 2- or 4- wire measurement and SQUID amplifiers.

2.6   A Comparison of Noise Properties in TESs and KIDs

TES arrays of 1000s of pixels with micromachined thermal isolation structures have been developed which approach background-limited sensitivity for both ground-based and space-based observations

of faint sources such as the CMB. KID arrays with similar pixel counts have been deployed in instruments such as MUSIC [44] and DARKNESS [45], but they have not yet reached these same sensitivity levels. However, the simplicity of fabricating and multiplexing KIDs has sparked considerable interest and naturally invites comparison with TES arrays in terms of their ultimate sensitivity.

For an optimized TES, fundamental noise limits arise from two sources: photon noise from the astrophysical sources or backgrounds under observation, and thermal noise caused by fluctuations in thermal carriers (typically phonons) passing through the weak thermal isolation link from the bolometer's absorbing structure to the thermal bath and by Johnson noise from the thermometer's resistance. For KIDs, photon noise is also present, as is generation-recombination (g-r) noise, caused by fluctuations in the number density of quasiparticles in the device from optical or thermal excitations. Currently, KIDs are limited by non-fundamental noise sources, such as two-level system noise in the dielectric substrates, but rapid progress is being made in understanding and reducing these noise contributions [46].

2.6.1 Recombination noise from optically and thermally generated quasiparticles in KIDs

The NEP from recombination noise in a superconducting system is [47]:

$$NEP_r = \frac{2\Delta}{\eta_{pb}}\sqrt{\frac{N_{qp}}{\tau_{qp}}} \tag{2.6}$$

where η_{pb} is the efficiency of converting energy into quasiparticles. N_{qp} is the number of quasiparticles in the superconducting film, and τ_{qp} is the time constant for quasiparticle recombination into Cooper pairs. The general behavior of η_{pb} is known from Monte Carlo simulations [48] and was recently measured [49]: the efficiency approaches 1 when the photon energy is matched to 2Δ, and approaches 0.57 when the photon energy is much larger than 2Δ.

2.6.1.1 A simplified derivation of optical quasiparticle recombination noise

Consider the following simple model of optical quasiparticle creation and decay:

$$\frac{dN_{oqp}}{dt} = \frac{P\eta_{pb}}{\Delta} - \frac{N_{oqp}}{\tau_{qp}} \tag{2.7}$$

where N_{oqp} is the number of optically-excited quasiparticles and P is the optical power absorbed by the detector. The first term on the right side of the equation describes optical quasiparticle generation. The amount of energy per time that contributes to breaking Cooper pairs is $P\eta_{pb}$, and the amount of energy required to excite each quasiparticle is Δ. The second term on the right side of the equation describes quasiparticle decay. The rate of quasiparticle decay is $\lambda_{qp} = 1/\tau_{qp}$, and the number of quasiparticles decaying per time scales with the number of quasiparticles present, N_{oqp}. In the steady-state, $dN_{oqp}/dt = 0$, so $\frac{P\eta_{pb}}{\Delta} = \frac{N_{oqp}}{\tau_{qp}}$. Simplifying, $N_{qp} = \frac{P\eta_{pb}\tau_{qp}}{\Delta}$. Using this result in equation 2.6 gives the following for the optical recombination noise, independent of τ_{qp}:

$$NEP_{or} = \sqrt{4\Delta P/\eta_{pb}} \tag{2.8}$$

which is consistent with the result obtained by Zmuidzinas [46] and others.

2.6.1.2 Thermally generated quasiparticles

As in equation 2.6, the thermally generated recombination noise is

$$NEP_{tr} = \frac{2\Delta}{\eta_{pb}} \sqrt{\frac{N_{tqp}}{\tau_{qp}}}. \tag{2.9}$$

The number of quasiparticles arising from thermal excitations is [50]:

$$N_{tqp} = 2N_0 \sqrt{2\pi k_B T_{bath}\Delta} \exp(-\Delta/k_B T_{bath})V, \tag{2.10}$$

where N_0 is the single spin electron density of states at the Fermi level and V is the volume of the device. τ_{qp} can be calculated from τ_0, the material-dependent characteristic quasiparticle recombination time, as follows [51]:

$$\tau_{qp} = \frac{\tau_0}{\sqrt{\pi}} \frac{N_0(k_B T_c)^3}{2\Delta^2}. \tag{2.11}$$

2.6.2 Optimization scheme and calculation of the fundamental noise for a typical KID

2.6.2.1 Optical Recombination Noise

To calculate the optical recombination noise we begin with equation 2.8 with the approximation that for $T_{bath} \ll T_c$, $2\Delta = 3.53 k_B T_c$. The energy gap also determines the pair-breaking efficiency, η_{pb} [48].

2.6.2.2 Thermal recombination noise

Equations 2.10 and 2.11 can be used to calculate the thermal noise. We have calculated the thermal recombination noise for a lumped element titanium nitride (TiN) KID designed to absorb millimeter-wave radiation, with an absorber volume of $\sim 30,000 \ \mu m^3$ (for an inductive meander of length ~ 4.3 cm, width $45 \ \mu m$, and thickness 16 nm, covering an area of ~ 14 mm^2). See chapter 4 for the design considerations used to generate these parameters. NEP dependence on volume is complicated but weak. Results are qualitatively similar for an order of magnitude range of volumes; for example, an order of magnitude decrease in volume shifts the value for the TiN ground-based case at 100 GHz in figure 2.5 by 2%. TiN offers several advantages over other common superconducting films such as aluminum, including high internal quality factor, long characteristic quasiparticle recombination time, and tunable critical temperature. For TiN, we have used $N_0 = 3.9 \times 10^{10}$ eV^{-1} μm^{-3} and $\tau_0 = 13.7$ ns at 1 K [52] and scales as $1/T_c^2$, which are reasonable current estimates for these values [53].

In these calculations of optical and thermal noise, we allow T_c to float across all reasonable values and select the T_c which gives the lowest total noise. We call this the "optimal T_c." Parameters dependent on T_c, such as Δ, τ_{qp}, and η_{pb}, are adjusted accordingly as part of determining the optimal T_c.

2.6.3   Thermal noise in TESs

Neglecting readout and Johnson noise contributions, TES bolometer noise is fundamentally limited by the thermal fluctuation noise occurring across the bolometer thermal weak link. This noise scales with the temperature of the detector and the temperature-dependent thermal conductance of the weak link, $G(T)$, between the hot absorbing region of the bolometer (T_{bolo}) and the cold bath (T_{bath}). For $T_{bolo} \sim T_{bath}$, $NEP_t = \sqrt{4k_B G(T_{bath})T_{bath}^2}$. However, for CMB optical loading, the TES bolometer experiences a relatively large heating due to the optical and bias loading power, and $T_c \gg T_{bath}$. In this case, bolometer thermal noise includes an additional term accounting for the thermal gradient across the link as follows [54]:

$$NEP_t = \sqrt{4k_B T_{bath}^2 G(T_{bath}) \frac{n}{2n+1} \frac{\left(\frac{T_{bolo}}{T_{bath}}\right)^{2n+1} - 1}{\left(\frac{T_{bolo}}{T_{bath}}\right)^{n} - 1}} \tag{2.12}$$

where n is the index of thermal conductivity of the bolometer. Here we have considered the case of diffuse conduction in the thermal link for the typical case of phonon-phonon scattering across a geometrically long weak link. Finally, bolometer thermal conductance is defined as:

$$G(T_{bath}) = \frac{\partial P_{tot}}{\partial T_{bath}} = n\kappa T_{bath}^{(n-1)}. \tag{2.13}$$

$$P_{tot} = \kappa(T_{bolo}^n - T_{bath}^n) \tag{2.14}$$

is the total power, including optical power and bias power which flows across the bolometer thermal weak link, and κ is the temperature-independent thermal conductance coefficient.
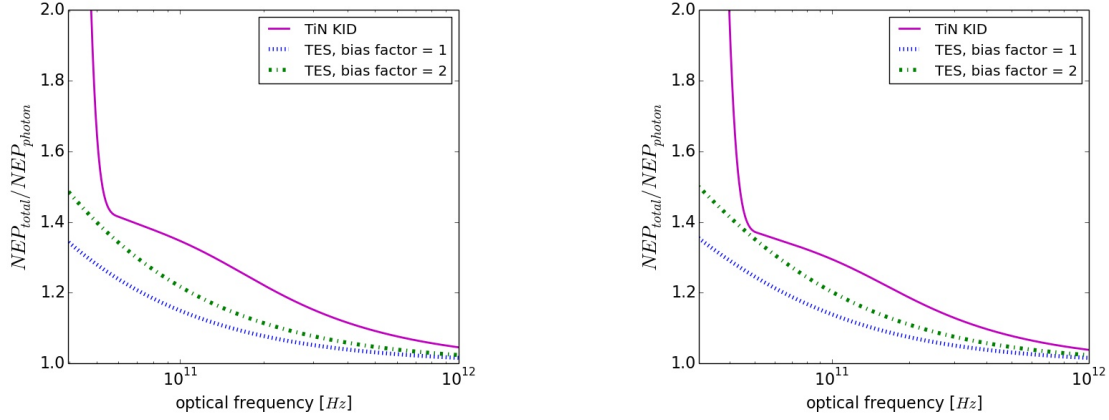
Figure 2.5: Ratio of total NEP to photon NEP as a function of optical frequency for ground-based (left) and space-based (right) observations with a 100 mK bath temperature.

2.6.4   Optimization scheme and calculation of the fundamental noise for a typical TES

Begin by assuming an optical loading and a bias power, which determines P_{tot} as follows: $P_{tot} = P_{opt}(n_{bias} + 1)$, where n_{bias} is the bias factor. For a chosen T_{bath}, the design requirement T_{bolo} (approximate T_c) is then constrained by the choice of κ via equation 2.14. For each of the loading and T_{bath} scenarios which follow, we choose κ to optimize NEP. These calculations use a thermal conductivity index of $n = 4$, characteristic of a thermal weak link controlled by phonon-phonon scattering, which is the most common TES bolometer design. A bias factor of 2, which is typical to ensure the TES will not be saturated if the optical loading is higher than expected [55, 56], is used.

2.6.5   Photon noise and optical loading

Begin with the usual expression for photon noise, $NEP_{photon} = \sqrt{2Ph\nu(1 + mB)}$, where ν is the center frequency, B is the photon occupation number per mode, and $m = \epsilon\eta$ is the efficiency from emission to detection of one mode. Results assume optical loading with 30% bandwidth and optical efficiency of 40%. The optical power is $P = h\nu^2\eta B\frac{\Delta\nu}{\nu}$, where η is the optical efficiency, and $\frac{\Delta\nu}{\nu}$ is the fractional bandwidth. In the space-based scenario, a 2.7 K sky temperature with emissivity of 100% is used. In the ground-based scenario, a 250 K sky temperature with 4%
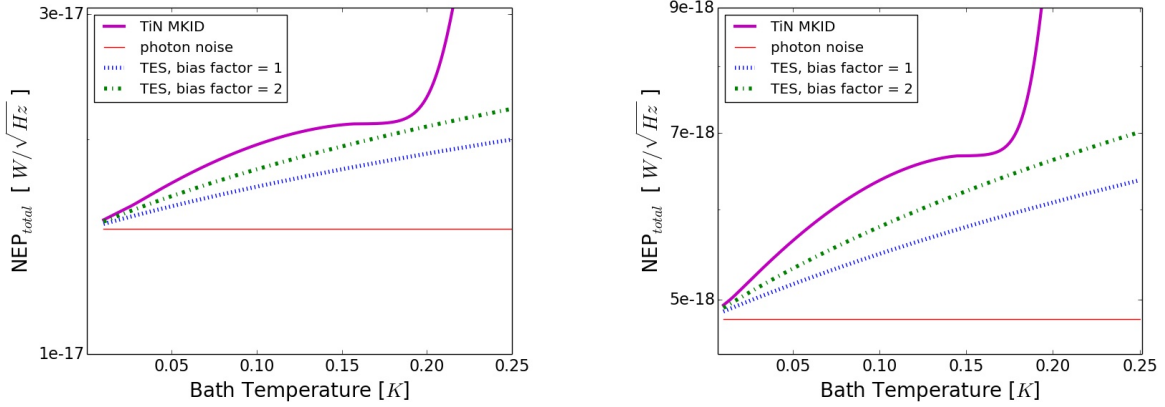
Figure 2.6: Total NEP as a function of bath temperature for ground-based (left) and space-based (right) observations at 100 GHz

emissivity (10 K Rayleigh-Jeans equivalent) is used. The total noise is simply each noise source, added in quadrature: For KIDs, $NEP_{tr+or+photon} = \sqrt{NEP_{tr}^2 + NEP_{or}^2 + NEP_{photon}^2}$. For TESs, $NEP_{t+photon} = \sqrt{NEP_t^2 + NEP_{photon}^2}$.

2.6.6 Results

First, consider how the NEP varies with optical frequency for TESs and KIDs. Figure 2.5 shows the ratio of the total NEP to the photon NEP as a function of optical frequency with a bath temperature of 100 mK for ground- and space- based scenarios. Under these conditions, across the range of frequencies considered, the KID has slightly higher noise than the TES with a bias factor of 2. At 100 GHz, the KID pays an 11% penalty in noise compared to the bias factor 2 TES in the ground-based case and an 8% penalty in the space-based case. Figure 2.6 shows the total NEP versus bath temperature with an optical frequency of 100 GHz. Again, the KID has slightly higher noise under these conditions for the range of bath temperatures considered here.

While KIDs have slightly higher noise in all of these cases, it is important to consider that KIDs can enjoy significant advantages over TESs in fabrication simplicity, multiplexing, focal plane coverage, and tolerance of T_c variation, depending on design.

2.7   Current Efforts and Challenges

The past several years have seen fielding of the first KID-based science-grade instruments, including NIKA [57], MAKO [58], ARCONS [59], MUSIC [44], DARKNESS [45], and others. Nonetheless, a number of challenges remain in advancing KID development.

Readout is a challenge across all optical and carrier wavelengths. While KIDs naturally lend themselves to passive frequency domain multiplexing and don't require complex cryogenic multiplexing schemes as TESs do, all of this complexity is instead placed on the room temperature readout electronics. Readout schemes are still constrained by bandwidth and processing power limitations, but this is an active area of research and significant progress has been made in the past several years [60, 61].

KIDs aimed at CMB observations are especially concerned with polarization sensitivity. While polarization can be modulated in the optical chain before the focal plane (such as with a rotating half wave plate), this effectively cuts the integration time in half for each orthogonal polarization. This motivates efforts to build on-wafer dual-polarization KIDs. In these designs, a single pixel contains two overlapping or stacked detectors, each sensitive to one polarization direction. A similar challenge is posed by efforts to build multichroic arrays, where a single pixel can contain multiple detectors each sensitive to photons in a different frequency band. Dual polarization and multichroic pixels have significant spatial and integration time advantages, but pose substantial challenges in terms of fabrication, optical efficiency, and crosstalk [62–64].

Crosstalk is a challenge not limited to dual-polarization and multichroic pixels. Any array of KIDs may suffer from crosstalk or frequency 'collisions' between pixels which are close together either in frequency space or physical space. Carefully designed grounding schemes, well-designed pixel geometries, and careful layout of pixels in the array to keep frequency-adjacent pixels as spatially far apart as possible all mitigate crosstalk at the source [46, 65].

Finally, material development is a major challenge in KID research, especially at the longest wavelengths, as will be discussed in more detail in chapter 4.

2.8   Applications of Kinetic Inductance Detectors

Most KID arrays in development are focused on relatively standard astronomical imaging at a variety of wavelengths. The bulk of KID development efforts have been aimed at millimeter and sub-millimeter wavelengths. Virtually all varieties of infrared and microwave astronomy are natural applications of the technology. In addition, extensive work has also been done in the terahertz range [66, 67], and with the addition of carefully-engineered x-ray absorbers they even show potential in the soft x-ray regime [68, 69]. KIDs can also be used as single-photon counters [52]. Superconducting resonators of the sort used in KIDs also have applications in parametric amplifiers [70], quantum computing [71], and TES multiplexing schemes [72].

CHAPTER 3

THE QUBIC TELESCOPE

The Q and U Bolometric Interferometer for Cosmology (QUBIC) is a ground-based telescope which will incorporate an array of highly-sensitive detectors into an interferometer designed to measure the polarization anisotropy of the cosmic microwave background. Q and U refer to the Stokes parameters measured by the instrument, which can be used to calculate B-mode and E-mode polarizations. As discussed in section 1.3, the large angular scale B-mode anisotropy is of particular interest because it is a probe of primordial inflation.

3.1   Interferometry

Interferometry has been an important technique in astronomy and cosmology for over 100 years. One of the earliest examples in cosmology is the Michelson Morley experiment [73]. Published in 1887, Michelson and Morley were trying to measure the motion of Earth relative to the proposed 'luminiferous ether'. Fizeau was the first to propose using an interferometer for astronomical observations [74]. Michelson later refined the idea and proposed a design for a stellar interferometer which could be used to measure the diameter of celestial objects by measuring very small angles. A small version of the device was used in 1891 to measure the diameters of some of the moons of Jupiter [75] and in 1920 the full size interferometer, with a maximum baseline of 20 feet, was used to measure the diameter of Betelgeuse [76].

In more recent history, CMB instruments including PIXIE [77], DASI [78], MBI [79], and QUBIC [80] have continued the tradition of interferometry in cosmology.

While interferometry poses certain challenges both instrumental and computational, it also offers a number of advantages which cannot be equaled with traditional direct imaging techniques. Direct imagers are limited in angular resolution by the practicality of constructing extremely large

mirrors. In addition to the challenge of the initial construction, it is also hard to limit thermal warping and sagging over time of very large mirrors, yet any deformation of the mirror will result in aberrations that decrease the ultimate sensitivity of the telescope. Interferometry benefits from its ability to create a large *effective* aperture using an array of relatively small *physical* apertures placed at large baselines. In this way, extremely fine angular resolution can be achieved using arrays of easily-fabricated parts. In addition to the advantages afforded by using large baselines to increase an instrument's effective aperture, interferometers also have advantages over traditional imagers in control of certain systematic effects. It is these advantages, rather than angular resolution, that have inspired the use of spatial interferometers for CMB applications.

One of the primary advantages of using interferometers for CMB applications is that each baseline naturally measures a Fourier mode of the sky. These modes are directly related to the angular power spectrum of the CMB fluctuations, which is the most convenient form to compare the CMB measurements with theoretical forecasts. A particularly important feature of the QUBIC telescope is the fact that individual baselines can be separately calibrated (see section 3.2.4.3). This feature will reduce the potential for leakage of the relatively strong E-modes into the far weaker B-modes, which might otherwise introduce a serious systematic effect [81].

3.2   A Technical Overview of the QUBIC Instrument

QUBIC (Q and U Bolometric interferometer for Cosmology) will study the polarization anisotropy of the cosmic microwave background (CMB) at large angular scales. It is designed to have sufficient sensitivity to detect a B-mode anisotropy corresponding to a tensor-to-scalar ratio of r < 0.008 (or r < 0.05 with a single module) at 95 % confidence with 2 years of observing time [82] [7]. The instrument will observe in broad bands centered at three frequencies: 97, 150, and 220 GHz. The final instrument will consist of six modules in total – each containing one or more frequency bands. Each module consists of an array of close packed primary and secondary horn antennas. The primary horns view the sky through filters, a half wave plate, and polarizing grid. The secondary horns, located directly behind the primary horns, look down into the cryostat at the 4 K primary

mirror. Between the primary and secondary horn arrays are electromagnetically actuated mechanical switches which can block and un-block individual horns. These are used for a unique self-calibration procedure that mitigates instrumental systematic effects (see section 3.2.4.3). The entire assembly is housed in a large pulse tube-cooled cryostat with a He^4+He^3 sorption fridge-cooled 320 mK cold stage. An earlier QUBIC design planned for an ADR-cooled 100 mK cold stage, and it is on this earlier design that we have based our KID design. Centered in Paris, the QUBIC collaboration includes institutions in France, Italy, the United Kingdom, Ireland, and the United States.

3.2.1   Optics

The first optical element encountered by incoming radiation is the HDPE cryostat window followed by the metal mesh rotating half wave plate (HWP). Rotation of the HWP provides polarization modulation and is achieved with a cryogenic stepping rotator which allows for eight discrete positions [81]. Following the HWP is a a series of filters, including thermal filters, band defining filters, and a polarizing grid, which is used to select one of the two orthogonal polarizations [6].

The primary horns view the sky through the window, filters, and HWP. The secondary horns, located directly behind the primary horns, re-emit down into the cryostat onto the 4 K primary mirror and 1 K secondary mirror. Between the primary and secondary horn arrays are electromagnetically actuated mechanical switches which can block and un-block individual horns. These are used for a unique self-calibration procedure that mitigates instrumental systematic effects (see section 3.2.4). The horn arrays consist of 144 close-packed pairs of horns for the 97 GHz modules and 400 pairs for the 150 and 220 GHz modules [83]. The horn arrays will be fabricated by stacking aluminum platelets with suitable holes formed by photochemical etching and milling [81].

After light reflects off of the secondary mirror, a dichroic filter separates the two frequency bands onto their respective focal planes, at 320 mK. The instrument is configured as an offset-Gregorian telescope, with the combined effect of the primary mirror, at 4 K, and the secondary mirror, at 1 K, serving as a beam combiner, allowing equivalent baselines to be coherently added at the focal plane as Fizeau interference fringes [84]. The system satisfies the Mizuguchi-Dragone condition, which
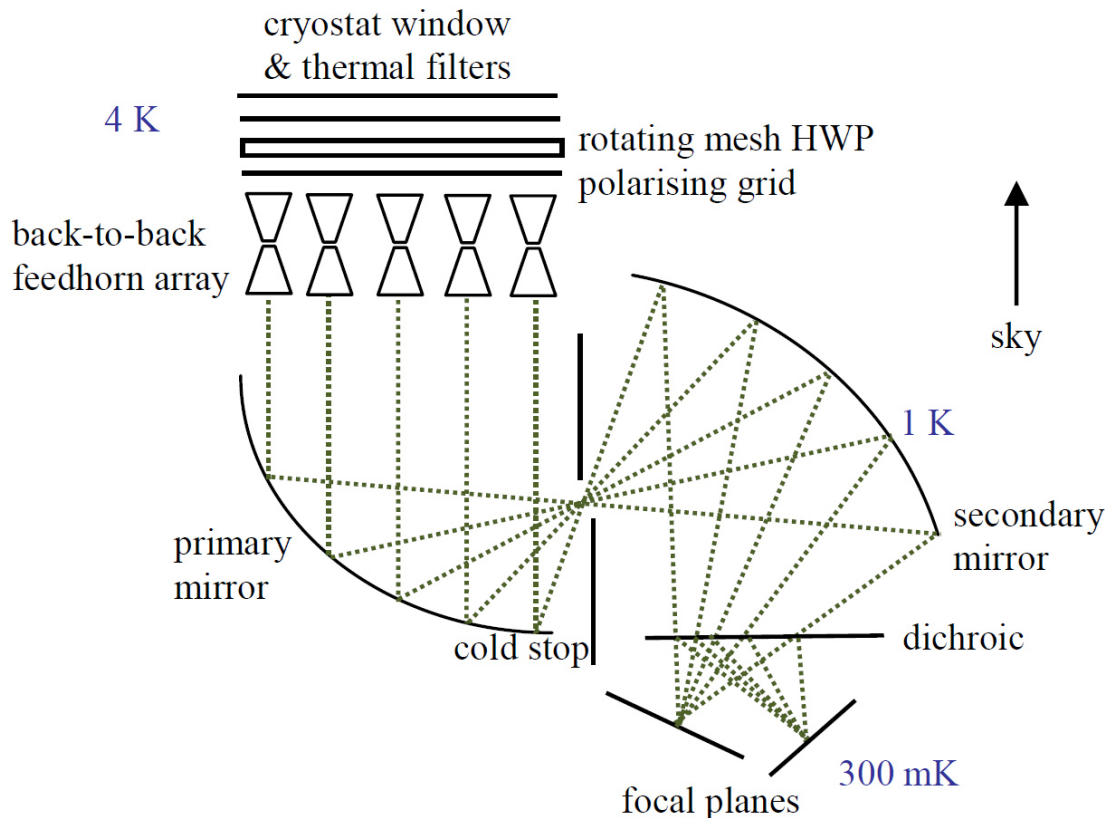
Figure 3.1: Schematic of the QUBIC optical chain. Image from [6].

controls spherical aberration and cross-polarization while maximizing the field of view [84].

3.2.2 Cryogenics

The original design for QUBIC called for a pulse tube pre-cooled cryostat with an ADR cooling the focal plane to 100 mK. It is on this earlier QUBIC design that we have based our detector design. A recent updated design calls for QUBIC to include a He^4+He^3 sorption fridge in lieu of the ADR. The expected focal plane base temperature in the current design is 320 mK. [85]

The filters, horns, and primary mirror operate at 4 K, while the secondary mirror is at 1 K and the focal planes are at 320 mK.
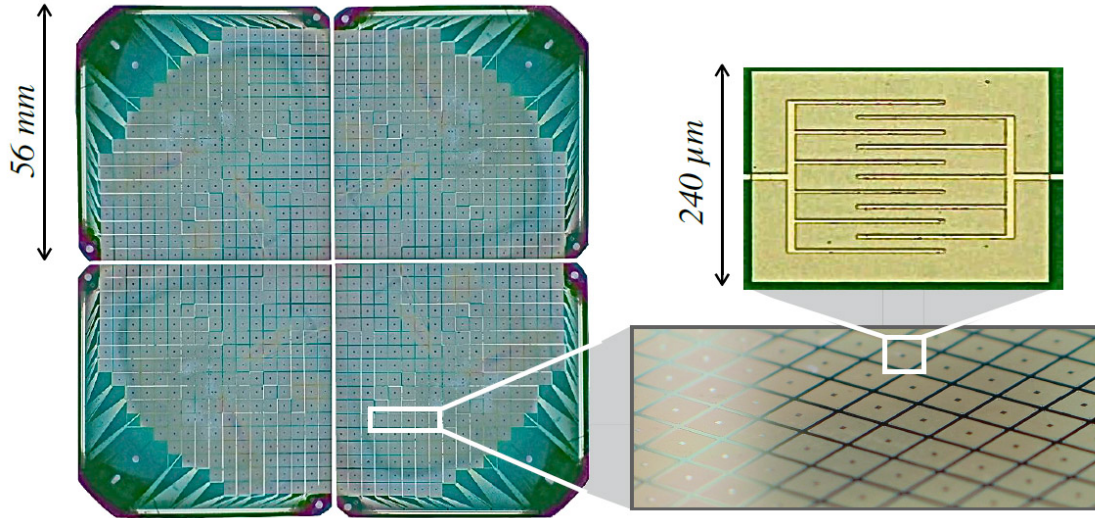
Figure 3.2: Micrograph of an early prototype array of TES bolometers. Upper left inset shows a close-up of the Nb_xSi_{1-x} thermistor electrode geometry. Image from [7].

3.2.3 Focal plane

Each module of QUBIC will be equipped with two 1024-element close-packed arrays of incoherent background-limited detectors. Originally designed with TES bolometers in mind, in this thesis I will present a proposed design for a KID array which could be installed on the 97 GHz module. It could also be scaled relatively simply to be compatible with the higher-frequency modules. The detectors must be close packed in order to Nyquist sample the interference fringes imaged on the focal plane and must achieve a noise equivalent power of $4 \times 10^{-17}\ W/\sqrt{Hz}$ with a time constant of less than 20 ms in order to achieve the performance required to meet QUBIC's sensitivity goals [7]. At the time we began the design and fabrication of the detectors discussed in this work, QUBIC planned to have a 100 mK focal plane, therefore all of our designs are based on that parameter, rather than the recently-updated 320 mK focal plane temperature.

150 and 220 GHz TES arrays are currently being fabricated for the first QUBIC module. Titanium-vanadium absorbing grids are coupled to Nb_xSi_{1-x} superconducting thermistors. The TES is suspended on SiN_x membranes with four micromachined legs which provide a weak thermal link to the bulk Si. The relative amounts of Si and Nb in the thermistor can be adjusted to tune

the critical temperature (T_c) to the target value of 0.4 K. Adjusting the geometry of the Nb_xSi_{1-x} electrodes tunes the normal resistance to the desired value of 200 mΩ [7]. The tuning of these parameters was chosen to select a satisfactory middle-ground between the conflicting goals of high sensitivity and high saturation power.

The TES array will be read out using SQUID time-domain multiplexing for the first stage, followed by a custom SiGe bipolar junction CMOS transistor ASIC. This scheme can achieve 128x multiplexing (32:1 from the SQUIDs and 4:1 from the ASIC) [86].

3.2.4 Observing strategy

3.2.4.1 Location

The first module of QUBIC, observing at 150 and 220 GHz, will be deployed at Alto Chorillos, Argentina in 2017. The proposed Argentinian QUBIC site is near the site of the LLAMA experiment, and will allow for sharing of resources and infrastructure between the two experiments. The site is located at an altitude of 4820 meters above sea level about 180 km south-east of ALMA, with atmospheric conditions similar to those for ALMA. While the goal is to eventually deploy the full instrument at Dome C in Antarctica to take advantage of the superior atmospheric conditions there, the initial deployment has been shifted to Argentina because if the complex logistics, high cost, and high bar for instrumental reliability required for an Antarctic deployment [81].

3.2.4.2 Field

QUBIC will focus one of two fields. The first field, centered on [Ra = 0 deg, Dec = -57 deg], has some of the lowest dust contamination of any part of the sky, and is also well-studied by a number of other CMB experiments, which will offer rich opportunities for comparison of results with other collaborations and joint analyses [81]. The second field, centered on [Ra = 8.8 deg, Dec = -41.7 deg] is a candidate low-dust field identified by the Planck satellite [87]. The final decision about which

field to observe will be deferred until QUBIC is ready to begin observations so that any additional data on dust contamination of these fields can be included in the final decision.

3.2.4.3 Self-calibration

One of the key advantages of interferometry over direct imaging is that individual interference fringes can be calibrated independently of other fringes [88]. The ability to individually measure single fringes is implemented in QUBIC using electromagnetically-actuated switches located behind the primary horns. Using these switches, any pair of horns can be selected as the only 'open' horns, and the focal plane response from that pair alone can be measured. The QUBIC self-calibration procedure consists of successively measuring the fringe pattern from every possible pair of horns while observing a man-made ground-based polarized source. In a perfect instrument, redundant baselines correspond to the same mode and should produce the same response. Any differences in the calibration measurements between redundant baselines in the real instrument (beyond that which can be explained by simple photon noise) must arise from instrumental systematics. It has been shown [89] that it is possible to significantly reduce instrumental cross-polarization systematics by combining these calibration measurements with a detailed model of the instrument. Using this procedure, E to B leakage can be reduced enough to measure B modes down to the r=0.05 level if 2.5% of the observing time is dedicated to calibration [81].

3.2.4.4 Foreground Removal

Because the anticipated magnitude of the B-mode anisotropy is extremely small (if r=0.01, the polarization will be on the order of a few nK), accurate foreground subtraction is essential for any instrument pursuing a B-mode measurement. Thermal emission from galactic dust, which has a different spectrum than the CMB, can be cleaned using measurements at multiple frequencies; this was part of the motivation for including the 220 GHz channel in the first module (instead of two 150 GHz focal planes as prescribed in the original QUBIC design) [81]. Synchrotron emission also

has a different spectrum than the CMB, but the synchrotron power falls with increasing frequency and is not expected to be significant at 150 or 220 GHz. Atmospheric polarization has been shown to be negligibly small [90].

3.2.5   Anticipated results and sensitivity

The first module of QUBIC is expected to be able to detect tensor-to-scalar ratios as small as r=0.05 with 95% confidence within two years of observing at 30% efficiency [82]. The full 6-module instrument will be able to reach tensor-to-scalar ratios as low as r = 0.01. The anticipated sensitivity of the instrument varies significantly depending on the deployment location: the expected noise equivalent temperature (NET) at 150 GHz at the Argentinian location is 305 $\mu K \sqrt{s}$ and 552 $\mu K \sqrt{s}$ at 220 GHz. At Dome C, the expected NETs are 278 $\mu K \sqrt{s}$ at 150 GHz and 461 $\mu K \sqrt{s}$ at 220 GHz. Concordia also offers the potential for higher observing efficiency since both fields of interest are always between 30 and 70 degrees of elevation, whereas they are only in that elevation range 40% of the time in Argentina. Accounting for this as well as poor observing conditions in the summers in both locations, the Argentinian location will correspond to a reduction in sensitivity compared to the Dome C location by a factor of $\sim$1.4-2.8 depending on how much time is spent on calibrations (which can be done while the CMB field is not visible, since the calibrations use an artificial polarization source). Ultimately, the first module of QUBIC, deployed in Argentina for 2 years, is expected to reach a sensitivity corresponding to $\sigma(r)$=0.01 (or 0.006 neglecting foregrounds) [81].

CHAPTER 4

DESIGN

4.1   Design Objectives

The goal of the design of these detectors was to generate a simple, inexpensive, easy to fabricate, filled array of direct-absorbing pixels for detecting 100 GHz microwave radiation with a $\sim$30% bandwidth and noise performance on par with TESs in comparable observing scenarios. After several iterations in both geometry and materials, the final design was a close-packed array of TiN/Ti/TiN trilayer nearly-square pixels consisting of a meandered microstrip inductor and interdigitated microstrip capacitor weakly coupled to a Nb microstrip transmission line. Ti/Au pads provide additional heat sinking and on- and off- chip diagnostic features allow for probing of film properties without disturbing the detectors themselves.

4.2   Geometry

4.2.1   Pixel Geometry

Each pixel consists of a meandered microstrip inductor and interdigitated microstrip capacitor connected to form a high quality factor resonator. The resonator is weakly coupled to an adjacent 50 Ω microstrip transmission line. As a starting point, the pixel geometry was based on a simple lumped element KID (LEKID) design originated by Simon Doyle [91, 92]. The details of our final design (see figure 4.1 were driven by a number of considerations, outlined below.
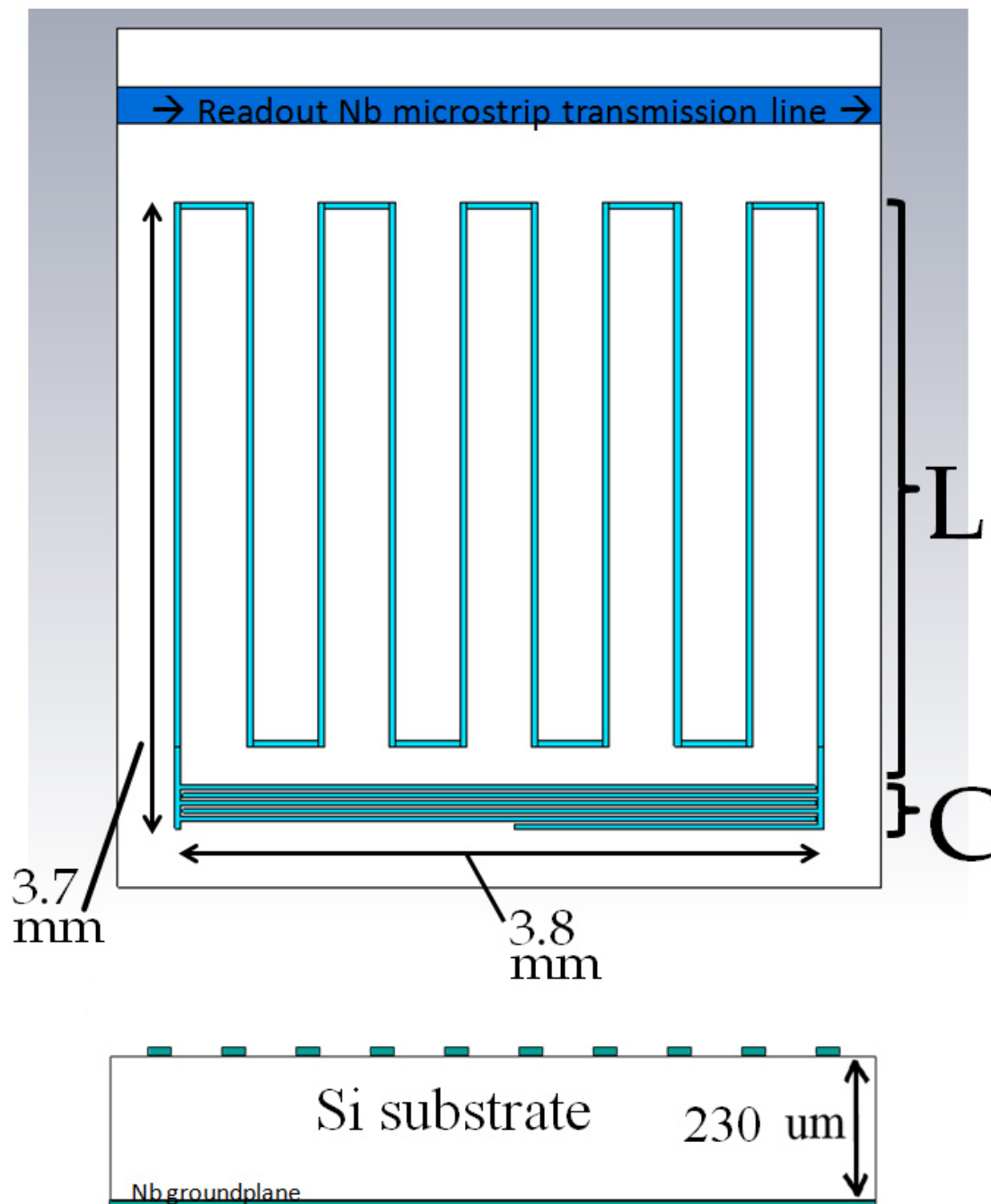
Figure 4.1: **Top:** CST model of geometry A. **Bottom:** side view of geometry A (not to scale).

4.2.1.1   Optical coupling

In order to couple efficiently to incoming microwave radiation, the pixel must be at least as large as one wavelength of the radiation to be detected. These detectors are designed to detect 100 GHz (3 mm) microwave radiation. The final pixel design was 3.7 mm × 3.8 mm including the inductor and capacitor.

The photosensitive portion of the detector is the inductor; the capacitor is entirely blind, so on the one hand it is important to make the capacitor take up as little area as possible compared to the inductor area. On the other hand, too little capacitance compared to the inductance will result in uneven current distribution in the inductor, which reduces the effective optical efficiency. In principle, one should simulate the current density in the inductor for various capacitances to optimize the balance between the two. However we lacked a computer with sufficient memory to fully simulate the pixel. Instead, we aimed for a capacitance to inductance ratio close to that of other similar lumped KID designs known to exhibit reasonable optical efficiencies. Ultimately, we settled on a capacitor which occupies about 5.5% of the total pixel area.

The geometry of the inductor is essential to the optical coupling. The meandered inductor is designed to have an effective sheet resistance matched to free space, 377 Ω. We aimed to use materials for the resonators with normal state sheet resistances (R_s) of 40 Ω/□. To match to free space, we need $R_{s_{eff}} = 377\Omega/\square = R_s p/w$, where p is the distance between inductor meanders (pitch) and w is the width of the inductor traces. The microstrip's groundplane on the backside of the wafer also acts as an integrated quarterwave backshort to aid in optical coupling. See section 4.2.2.1 for a more detailed discussion of the integrated backshort/groundplane.

4.2.1.2   Two-level system noise mitigation

One of the most significant challenges in KID design is mitigating noise arising from two-level systems (TLS) in the substrate. While TLS is not a fundamental noise source for KIDs, in practice resonator quality factors are often limited by TLS rather than by thermal loading, superconductor

impurities, or coupling [46]. The first line of defense is avoiding amorphous dielectrics, which are significantly more prone to TLS problems. This motivated the choice of <001> high resistivity Si wafers for all of the KIDs described in this work. TLS are excited by high electric fields [46], therefore it is helpful to avoid unnecessary high-field features in KID designs. The original KID design, referred to hereafter as 'geometry A,' tested in this work had sharp corners (up to the limits of the photolithography) on all of the pixel features. These sharp corners were likely to be areas of especially high electrical field magnitudes which could have excited excess TLS in the substrate (though we were never able to make that measurement with the original sharp-cornered design). In a later design, referred to hereafter as 'geometry B,' all of the sharp corners were replaced with curves and rounded-off corners. Finally, the highest fields in KID designs of this type often occur in the capacitor, due largely to the incentive to make the capacitor as geometrically small as possible (to minimize blind area) while making it as high-capacitance as possible (to keep the current density in the inductor as even as possible). The need for a small, dense capacitor must be balanced with the need to keep field magnitudes reasonable. We settled on a capacitor with trace widths and spaces of 20 μm.

4.2.1.3   Resonator coupling

The total quality factor, Q, of a KID resonator is determined by two factors: The internal quality factor, Q$_i$, and the coupling quality factor, Q$_c$. Q can be calculated from Q$_i$ and Q$_c$ as follows:

$$\frac{1}{Q} = \frac{1}{Q_c} + \frac{1}{Q_i}. \tag{4.1}$$

Responsivity is proportional to Q^2/Q_c (a detailed derivation of this can be found in chapter 4 of Jiansong Gao's thesis [93]). Therefore responsivity is optimized when $Q_c = Q_i$. Internal Q is affected by a number of factors including resonator film quality and loading or dissipation from any source, including thermal excitations, optical excitations, and excitations from TLS noise. Coupling quality factor is determined by the strength of the coupling between the pixel and the readout transmission

line. The stronger the coupling (the smaller the coupling distance, or the closer the pixel is to the readout line) the lower the coupling quality factor. Since it is difficult to predict Q_i in advance, the chips were designed to have pixels at a variety of coupling distances to increase the chances of having at least a few resonators for which Q_c was well-matched to Q_i. Coupling distances from 100 μm to 1000 μm were used in geometry A. Based on electromagnetic simulations (see section 4.3.1), the Q_cs were expected to be between 4000 and 790,000, however measured Q_cs were substantially higher (see chapter 7). In geometry B, we used empirical results from measurements of geometry A to choose updated coupling distances ranging from 100 to 340 μm to achieve coupling Qs between 6000 and 100,000.

4.2.1.4   Readout frequency

There were three primary driving factors in the decision to design the detectors' resonant frequencies in the few-hundred MHz range, as opposed to the few-GHz range which is another popular range for KID carrier frequencies. First, readout electronics are less expensive in the hundreds of MHz regime, and we already several essential pieces of equipment useful in the relevant frequency range. Second, as discussed in detail in [46] and [93], there are noise advantages associated with a lower-frequency readout. Finally, limiting ourselves to a pixel geometry of roughly this style, the range of resonance frequencies we can reach with good optical matching and reasonable feature sizes is fairly limited and happens to fall in the hundreds of MHz range.

4.2.2   Chip Geometry

4.2.2.1   Integrated groundplane/backshort

The chip design differs from many other similar KID designs in its inclusion of an integrated superconducting backshort/groundplane. Whereas most designs have bare, AR-coated silicon facing the illumination source, with resonators printed on the back side of the wafer, followed by a

vacuum gap to a $\frac{1}{4}\lambda$ backshort which is mechanically part of the chip holder/package, our design has the resonators on the front (illumination-facing) side of the wafer and an unpatterned Nb backshort/groundplane on the back side of the Si. This geometry offers several advantages. From a mechanical standpoint, no precision spacers are required on the chip package because the backshort distance is set by the thickness of th Si itself. This geometry also allows for efficient optical coupling without the necessity for either AR coatings or thin membranes. Additionally, we were able to design the chip such that the ground plane is completely unpatterned, affording us the advantages of a microstrip geometry while avoiding the financial and logistical costs of an additional lithographic layer (and one requiring backside alignment, which further complicates fabrication).

The integrated groundplane design does have some drawbacks. Since the Si thickness sets the backshort distance, Si wafers with a thickness of $\frac{1}{4}\lambda$ at 100 GHz (130 μm) had to be special-ordered, which represents a substantial increase in cost compared to standard-thickness Si wafers of the same grade. The relatively thin Si wafers also pose a mechanical challenge; while vastly less delicate than the few-micron membranes often used in TES designs, these wafers nonetheless require special care during processing to avoid breakage. During the first fabrication run, we were especially conservative with the Si wafer handling, choosing to wax-bond Pyrex handle wafers to the Si wafers immediately after the Nb groundplane deposition step. The Pyrex backing wafers remained in place through the entire remainder of wafer processing, and were removed only after dicing. No Si wafers handled with Pyrex backing wafers broke during processing, however the resonator material (molybdenum) on one was destroyed during an attempt to release the wax bond by soaking in acetone for an extended period of time.

In subsequent processing runs, we made the decision to be slightly more cavalier with wafer handling and skip the Pyrex backing wafer step because the introduction of sticky wax onto the wafers and the exposure of the wafers to the relatively dirty wax room invited a lot of undesirable dust and dirt which substantially increased our rate of lithographic flaws. Additionally, the practicalities of releasing the wax-bonded backing wafers proved to be more difficult than anticipated. Releasing in acetone is incompatible with the molybdenum resonator layer; we learned the hard way that acetone is a molybdenum etchant, albeit a relatively slow one. To release the wafers without solvents

requires heating, but we were concerned the heating might have been damaging the Mo films as well. In subsequent runs, we forewent the Pyrex and were simply "extra careful" with the wafers. Using this method, we saw a reduction in the rate of lithographic flaws and of general wafer dirtyness, but did have three (out of 10) wafers break during processing. In two breakage instances, only two of the six detector chips and none of the diagnostic chips were damaged. In the case of the third broken wafer, the entire wafer was destroyed, however in that particular instance, it's possible the level of damage would have been similar even with a Pyrex backing wafer. Despite the three broken wafers, the overall yield of usable pixels and usable chips was higher without the Pyrex backing wafers because of the significant reduction in lithographic flaws.

Broadly, in this case the advantages of the integrated groundplane/backshort design outweigh the disadvantages. Even though the integrated ground plane results in more expensive wafers which are more likely to break, the straightforward and simplified lithography and the elimination of the need for AR coatings, precision spacers in the chip package, or a patterned groundplane more than compensates for the disadvantages. The straightforwardness of this geometry was central to the "keep it simple" design philosophy.

4.2.2.2   Heat sinking

Keeping the detectors in good thermal contact with the cold bath is essential to achieving high sensitivity and avoiding excess thermal noise. There are three primary ways for excess heat (such as from incident microwave radiation and from any readout power dissipated in the chip) to escape the chip:

1) Through the transmission line wirebonds: Thermal contact to the cold bath via the transmission line wirebonds is insufficient for three reasons. First, the bond wire is just 0.001" in diameter, and the bonds are long compared to their width. Second, aluminum wire was used. Since aluminum is a superconductor, thermal conductivity below its critical temperature of 1.2 K is relatively low. Third, the transmission line wirebonds are all on one edge of the chip, so depending on those bonds for thermal sinking has the potential to produce a thermal gradient across the chip.

2) Through the back of the chip: Thermal conduction through the back of the chip might be adequate on its own to thermally sink the detectors. While the thick Nb groundplane is a superconductor, and therefore not especially thermally conductive at the relevant temperatures, the large total area compensates for this, and in principle, with good contact between the chip and the chip package, the thermal conductance through the back of the chip is adequate to conduct away the estimated few pW of optical power + readout power being dissipated in the chip. However, there are several complications. The plane of the package where the chip sits is not perfectly flat (it has milling lines which have been partially, but not perfectly, sanded away), making it difficult to guess how much contact the chip is making with the package. Second, while the package is gold plated, the thickness, quality, and surface roughness of the gold plating are not known, making assessment of the Kapitza resistance between the Nb, Au, and Cu difficult to assess. Finally, at low temperatures, thermal conductance between metal pieces is dominated by the force with which they are held together, but the clamping force of the package spring clips is not known (and likely varies a fair amount from one installation to the next since the clamping force is determined by the tightness of the screws and by the precise shape of the clips, which may be slightly reshaped during each installation). Since it is difficult to be certain of the thermal conductance through the back of the chip into the package, additional measures were taken to ensure adequate thermal contact.

3) Through gold pads on the corners of the chip: The chips were designed with large Ti/Au pads in the corners, 5000 $\mu m \times$ 2000 μm. The gold pads are connected to the package (and therefore the cold bath) through gold wirebonds going from the gold pad to the package. The bonds are kept as short as possible to minimize the thermal length, and a minimum of four bonds were placed on each of the four pads to be certain of getting adequate thermal contact to the cold bath. The gold bond wire used was 0.001" in diameter, and while the bond lengths varied, I estimate they were about 1 mm in length, on average. Gold has a conductivity of order 10 W/Km at 100 mK, so for sixteen 1 mm bonds, the thermal throughput is of order 10^{-7} W/mK, which is more than adequate for the anticipated thermal loads.

4.2.2.3   Transmission line

The readout transmission line must pass next to each pixel. To achieve this, the line passes between the first and second row and then between the third and forth row of pixels, connected by a 'flattened U' shaped structure (see figure 4.2). The carrier signal passes both onto and off of the chip on the same side, which simplifies the chip package design and fabrication because only one transition circuit board is required and because precise alignment with the package is only required on one side of the chip. The line is 50 Ω microstrip to achieve good matching with standard 50 Ω SMA connectors, coaxial lines, and test equipment. Since the Si thickness is set to 230 μm by the optical wavelength, this impedance choice sets the readout line width to 189 μm.

The readout line needs to be superconducting at our bath temperature of 150 mK to minimize loss, but there are no stringent requirements for other properties, such as quasiparticle time constant, density of states, or normal state sheet resistance, as there is for the resonator material. Niobium was selected since it is reasonably inexpensive, high-quality films are relatively easy to grow, and processes for patterning it are compatible with the other lithographic layers in the design. Since there are no requirements for high sheet resistance or kinetic inductance, the Nb films can be made quite thick to increase the probability of getting a good-quality film. We chose to use a film thickness of about 2000 Å for the frontside Nb. The backside Nb, which forms the groundplane for the microstrip and also acts as a quarterwave backshort, must be thick enough to isolate the chip from the non-superconducting copper chip holder to avoid unncecessary electrical loss. To this end, the backside Nb is about 5000 Å thick.

4.2.2.4   Resonator layout

Several factors come into play when deciding the physical spacing and frequency spacing of the resonators. First, the frequency spacing needs to be large enough that they don't overlap under dark conditions. It is important that they not only avoid actual overlap, but that they are spaced several times the resonances' FWHM apart to minimize pixel-pixel cross-coupling. Since we didn't know in

advance what resonator quality factor to expect, the prototype array design aimed for large readout spacing, though in a larger array one would want to more carefully optimize frequency spacing to conserve readout bandwidth. The resonator frequency is varied by changing the number of inductor meanders and by adjusting the length of the last capacitor finger. The number of meanders makes relatively coarse-grained changes in the resonator frequency since geometric limitations require that the number of meanders is always even. The length of the 6th capacitor finger is used for fine-grained adjustments. It can be varied continuously from a length of zero (effectively making the capacitor a 5-fingered capacitor instead of a 6-fingered capacitor) up to the full length of the other capacitor fingers. The 20 pixels were designed to be evenly spaced between about 420 MHz and about 530 MHz. This corresponds to the frequency range from 14 inductor meanders with six capacitor fingers to ten inductor meanders with 5 capacitor fingers. Later, in geometry B, changes in frequency spacing were made based on empirical results from testing of the geometry A. Geometry B was designed to have 20 pixels evenly spaced between 380 MHz and 477 MHz, which corresponds to the range from fourteen meanders with six capacitor fingers to twelve meanders with five capacitor fingers.

Having the resonators spaced far apart in frequency space is important for limiting 'frequency collisions' between pixels and pixel-pixel cross-coupling, but cross-coupling can be further reduced by careful layout of the resonators on the chip. Naïvely, one might be inclined to place the resonators on the chip in order of frequency. Certainly, this results in the simplest mapping of resonances to geometric positions on the chip. However, to minimize cross-coupling it is best to place frequency-adjacent resonators as far apart on the chip as possible. I wrote a simple script to search through possible resonator layouts. Using a true brute-force approach and requiring an optimal solution – rather than a solution that merely meets 'sufficiency' parameters – runs in factorial time. However, by making simple cuts based on symmetries of the array layout, by requiring that the solution be merely sufficient rather than optimal, and by using a depth-first binary search algorithm, it took only a few hours to find a solution on a single core of a consumer-grade processor. It is actually easier to find sufficient solutions for larger arrays because there is more room to spread out frequency-adjacent pixels (though of course it takes much longer to find optimal rather than sufficient
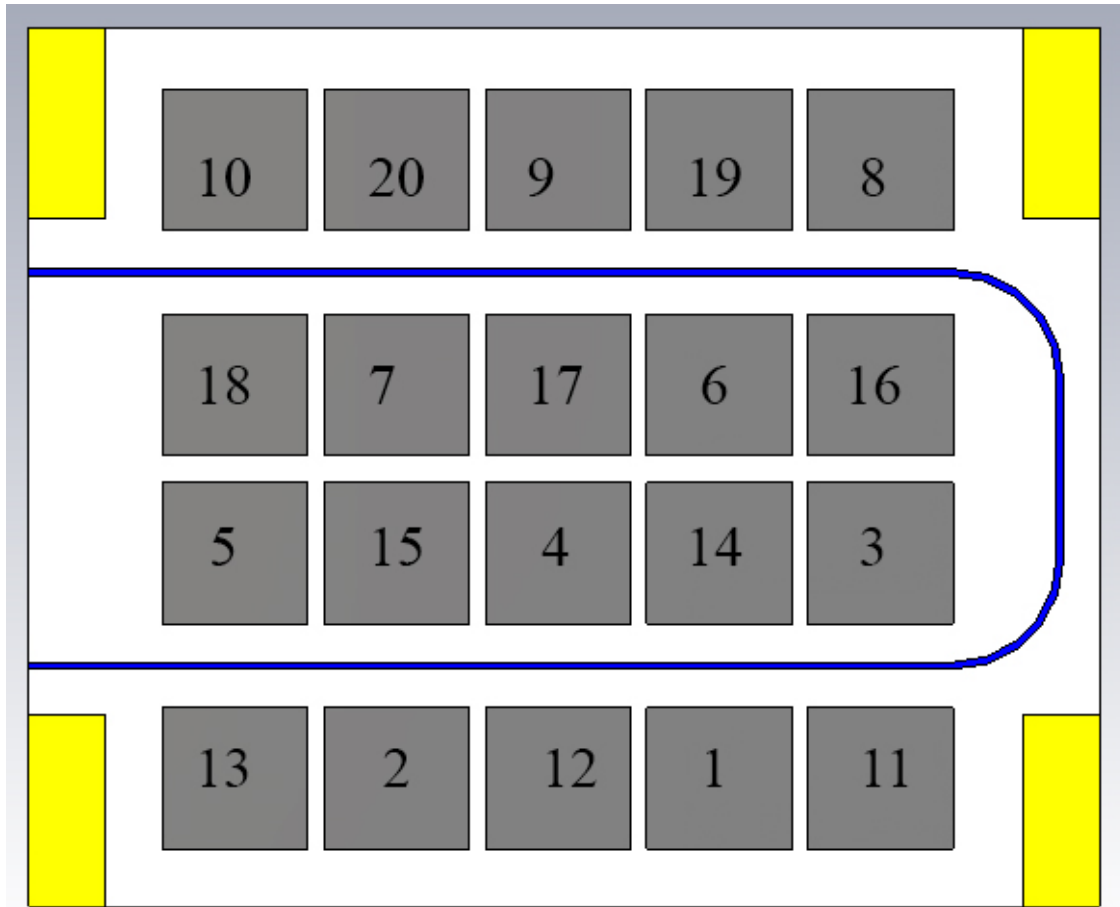
Figure 4.2: Layout of pixels on the 28 mm × 23 mm chip. The blue line is the readout microstrip line. The yellow pads are thermal contacts for cooling the chip. The resonator marked '1' is the lowest frequency, '2' is the second lowest, and so on up to the highest-frequency resonator, which is marked '20'. On chips with a Nb test resonator, the Nb resonator is in position 20.

solutions for larger arrays). For this array, I defined 'sufficiency' as geometrically neighboring pixels (whether side-to-side, above/below, or diagonal) being a minimum of two frequency steps apart. The determination that this condition was sufficient was driven by electromagnetic simulations (see section 4.3.1) and also by the fact that there were no solutions for this array size meeting more stringent requirements. See figure 4.2 for a schematic of the final pixel layout.

4.2.2.5   Chip size

The prototype arrays described in this work are 20-pixel (4×5) arrays. This chip size arose as a balance between two competing goals. On one side, we wanted large enough arrays to have a good variety of detectors to test on a single chip and to have many resonances so that any possible problems with cross-coupling or frequency collisions would become apparent. On the other side was a desire to fit many chips on each wafer to increase the probability of having chips with high detector yields. We could not simply increase the wafer size to achieve the latter goal since the NASA Goddard Detector Development Laboratory is nominally configured to process 100 mm diameter wafers. See figure 4.9.

4.3   Design Methodology

4.3.1   Simulations

Simulations of the resonator geometry were carried out using the commercial EM simulation software package CST Microwave Studio.

The bulk of our simulation efforts were directed towards understanding he RF behavior of our resonators. We investigated the effect of various geometric changes on center frequency and coupling to the readout line. We also made a study of crosstalk between neighboring pixels. In addition to the RF simulation work, we also studied the microwave properties of our geometry.

4.3.1.1   Resonator frequency

A model of the pixel design was drawn in CST microwave studio and simulated using the frequency-domain solver included in the CST software package. Unfortunately, the version of CST we had was not able to account for kinetic inductance; in comparing the RF frequency simulations with the

semi-analytic calculations, the kinetic inductance was removed from the semi-analytic calculations (and then added back in to come up with a final frequency estimate).

We found the simulated resonator frequency was somewhat sensitive to the meshing of the model, but with careful attention to CST's automatic meshing parameters, we were able to generate results which had close agreement with both the semi-analytic results and with the actual measured results. For example, for the lowest-frequency resonator, with six full-length capacitor fingers and fourteen meanders in the inductor, the model simulation suggested a resonant frequency between 554 MHz and 565 MHz depending on meshing details. The semi-analytic calculation with kinetic inductance removed estimated a resonance frequency at 544 MHz. With kinetic inductance added back in, the semi-analytic calculations estimated a resonant frequency of 380 MHz. The measured frequency for this resonator in geometry B was measured at about 388 MHz at 277 mK. In summary, while there is not perfect agreement between the simulations, semi-analytic results, and actual measuremnts, they are all within about 2% of each other.

4.3.1.2   Coupling to readout line

As discussed in section 4.2.1.1, we ideally seek to match the coupling quality factor to the internal quality factor. Since we couldn't predict film qualities in advance, we aimed for a wide range of coupling quality factors, and since the pixel geometry is fairly complicated, we chose to simulate the coupling to the readout line rather than attempting to calculate it analytically or semi-analytically. Unfortunately, the simulated coupling quality factor was highly sensitive to the simulation meshing. This issue was partly mitigated by making the model of certain parts of the pixel out of many smaller pieces, which forces the software to have mesh cell boundaries on the edges of these smaller pieces. Nonetheless, it was still not possible to get consistent results with this method. We were still able to estimate a ballpark range for the coupling Qs for different separations between the pixel and the readout line. Based on a best guess from the simulations, the expected range of Q_cs in geometry A (coupling distances 100 - 1000 μm) was 4000 - 790,000. Empirical Q_cs were a factor of a few higher (see chapter 7).

4.3.1.3 Pixel-pixel cross-coupling

To evaluate the coupling between neighboring pixels, I placed two identical (same nominal resonant frequency) pixels next to each other (side-to-side, above/below, or diagonal) in the CST simulation environment and ran the frequency domain simulator. Since the two pixels should nominally have exactly the same resonant frequency, any 'splitting' (shifting of the two resonators' resonance frequencies apart from each other) between the resonances arises from cross-coupling between the two pixels. The amount of coupling is proportional to the fractional frequency splitting, Δ_f/f_{avg} or $\frac{2(f_2 - f_1)}{f_1 + f_2}$. The results of these simulations are shown in figure 4.3, and represent the worst-case scenario since the pixels in the simulation are at the same frequency. The farther apart adjacent pixels are in frequency space the lower the coupling will be. Additionally, generally coupling is stronger when two pixels have their inductors facing each other, and weaker when the capacitors are facing each other. We are aiming to keep coupling below a half percent, and even in the worst-case same-frequnecy scenario in the simulation, we are meeting that goal.

4.3.1.4 Microwave coupling

The microwave coupling depends on two geometric factors: first, the integrated quarterwave backshort must be, as the name suggests, one quarter wavelength away from the pixel, and second, the effective sheet resistance of the meandered inductor, R_s, must be as close as possible to 377 $\Omega/\Box$, the impedance of free space. To simulate the microwave coupling, the inductor was modeled as an infinite tiling of Si coated on the back with perfect electrical conductor and covered on the front with strips of metalization of width w and pitch p (see figure 4.4). Simulation results (see figure 4.5) show that for $p = 289\mu m$, $w = 31\mu m$, and $R_s = 40\Omega/\Box$, we reach $\gtrsim 40\%$ absorption in a 30% bandwidth around 100 GHz, and nearly perfect absorption at 100 GHz.
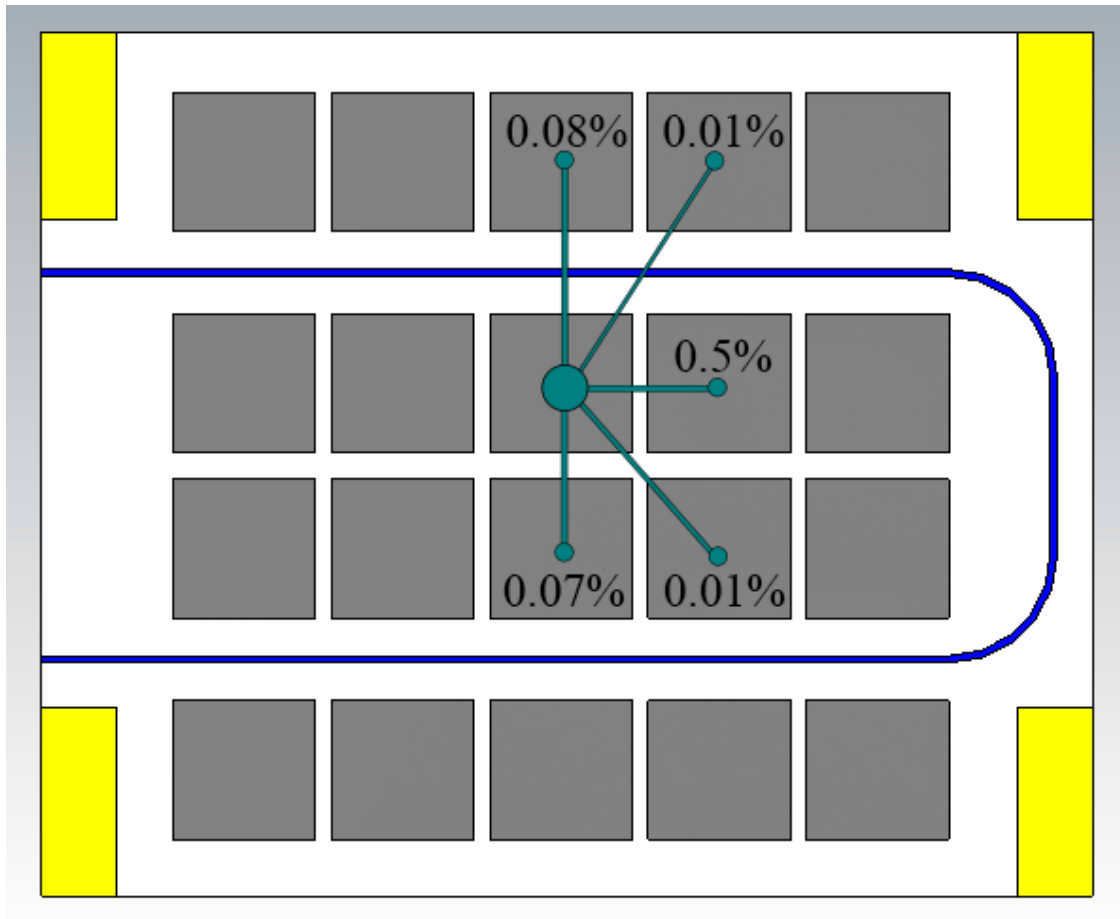
Figure 4.3: Results of cross-coupling simulations. The percent frequency splitting is shown between the center pixel (with the large teal dot) and the indicated surrounding pixels (with the smaller teal dots). Each pixel pair was simulated separately since there wasn't a computer available with enough RAM to simulate more than two pixels at a time.

4.3.2 Semi-analytic Calculations

The semi-analytic calculations focused on validating the results of the RF simulations and to calculate the effects of kinetic inductance, which could not be included int he simulations with the software we had available.
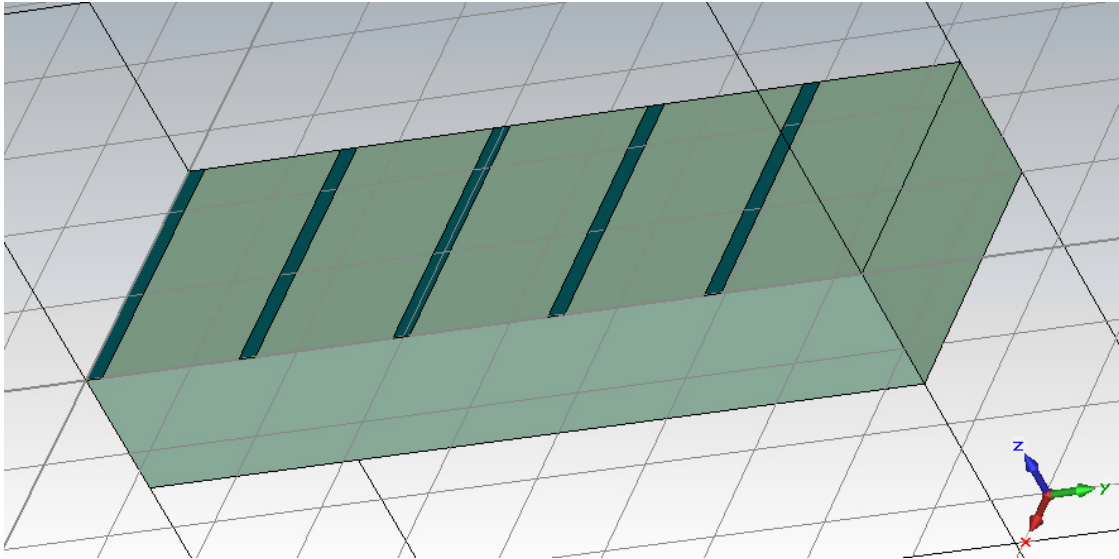
Figure 4.4: Unit cell used for optical coupling simulations. The width of the metallizations (shown in dark green) is 31 μm and the pitch is 289 μm with a sheet resistance of 40 $\Omega/\square$ to produce an effective sheet resistance of 377 $\Omega/\square$. The backside of the unit cell is covered in a continuous sheet of perfect electrical conductor. For the simulation, the unit cells are tiled infinitely in the x and y directions, and radiation is incident from the +z direction.
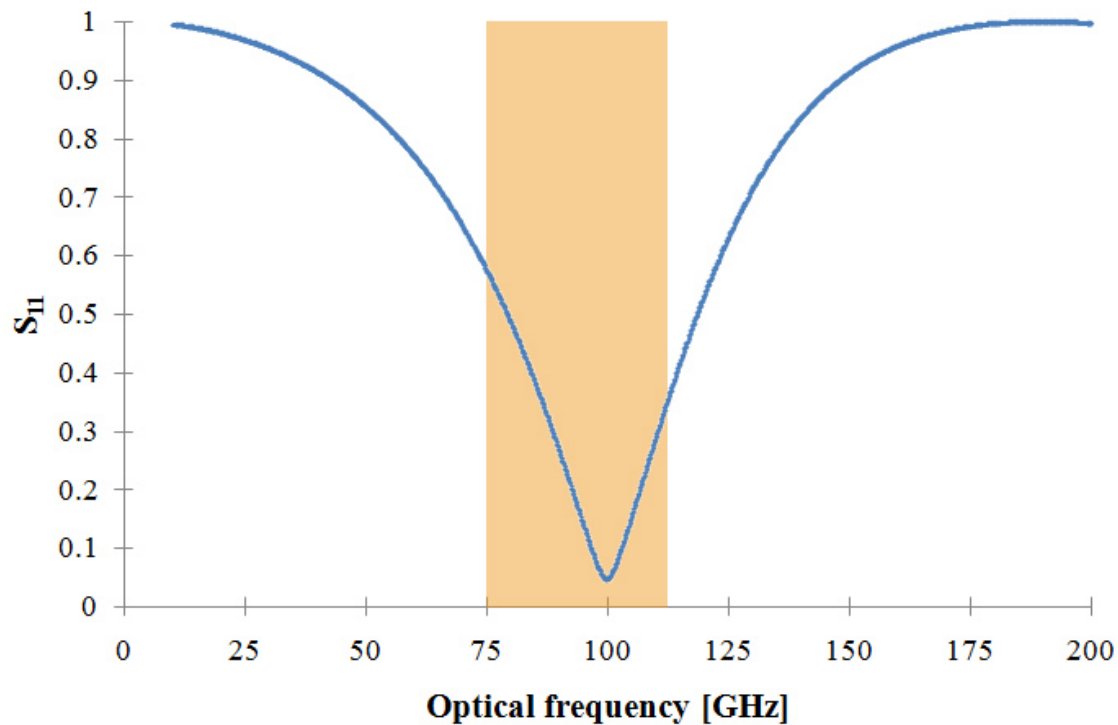
Figure 4.5: Simulated optical coupling of the unit cell in figure 4.4. Plotted is the fraction of normally incident power that is reflected. The W-band, from 75-110 GHz is highlighted.

4.3.2.1 Interdigitated capacitor

For an interdigitated microstrip capacitor on a substrate of thickness h, finger width w_c, inter-finger spacing equal to the finger width, N fingers of length ℓ_C, and relative permittivity ϵ_r, the capacitance can be approximated as [94]:

$$C = (\epsilon_r + 1)\ell_C[(N - 3)A_1 + A_2] \qquad [pF] \tag{4.2}$$

A_1 and A_2 can be approximated as follows [94]:

$$A_1 = 4.409 \tanh\left(0.55\left(\frac{h}{w_c}\right)^{.45} 10^{-6}\right) \qquad [pF/\mu m] \tag{4.3}$$

$$A_2 = 9.92 \tanh\left(0.52\left(\frac{h}{w_c}\right)^{.5} 10^{-6}\right) \qquad [pF/\mu m] \tag{4.4}$$

Using these equations with $w_c = 20\mu m$, $\ell_C = 3719\mu m$, $N = 6$, and $h = 230\mu m$, we get a capacitance of 1.00 pF. With 5 capacitor fingers, we get 0.81 pF.

4.3.2.2 Meandered inductor

The geometric self-inductance of a microstrip line of width w_L, length ℓ_L, and film thickness t (all measured in cm) can be approximated as follows [95]:

$$L_{geo} = 2\ell_L\left[ln\frac{2\ell_L}{w_L + t} + 0.50049 + \frac{w_L + t}{3\ell_L}\right] \qquad [nH] \tag{4.5}$$

With 14 meanders, the total inductor length is 4.9 cm, the width is 38 μm, and the thickness is 200 nm. This gives a geometric inductance of 85 nH. For 12 meanders, the total inductor length is 4.3 cm, the width is 45 μm, and the thickness is still 200 nm. This gives a geometric inductance of 71 nH.

Kinetic inductance for microstrip can be estimated for systems where the penetration depth is much smaller than the film thickness as follows [96]:

$$L_k = 0.64 R_s N_\square \hbar / 2\Delta \qquad [H] \qquad\qquad (4.6)$$

where $N_\square$ is the number of squares of the microstrip. $N_\square = \ell_L / w_L$. For the 12 meander inductor, $L_k = 66~nH$ and for the 14 meander inductor, $L_k = 89~nH$. Thus the kinetic inductance fraction for these devices ranges from about 48% to about 51%.

4.4   Materials

4.4.1   Resonator materials

4.4.1.1   Molybdenum

Molybdenum was used for the first two sets of resonators. It is an appealing material for use in KIDs because of its critical temperature (0.9 K is close to what we require to achieve a gap energy optimized for 100 GHz photons), long characteristic quasiparticle lifetime, and low electron single spin density of states. To have an elemental material exhibiting these properties makes fabrication significantly simpler compared to materials requiring tuning of proximitized layer thicknesses or gas flow rates, as with miltilayer materials or non-stoichiometric nitride materials. Two different molybdenum deposition recipes were used in the first two batches of resonators (see chapter 5 and appendix A for more detail). Unfortunately, as discussed in section 7.1, we were not able to achieve resonator quality factors greater than ~5000 with molybdenum and subsequently abandoned the material.

4.4.1.2   Titanium Nitride

After abandoning molybdenum as a candidate resonator material, we turned our focus to titanium nitride (TiN). Initially, with significant help from Ari Brown of NASA Goddard Space Flight Center,

we focused on identifying a suitable recipe for sub-stoichiometric monolithic titanium nitride. TiN has desirable features for KID resonators including a low single spin electron density of states at the Fermi level, long characteristic quasiparticle recombination time, and tunable T_c depending on the flow of nitrogen during film deposition (see chapter 5 for more detail). However, as outlined in chapter 7, in the limited time available we were not able to find a recipe that was both reliable and had the required film properties. In order to more easily produce films with the requisite critical temperature, we turned to TiN/Ti/TiN trilayers, based on earlier work by Mike Vissers [43] and again with significant help from Ari Brown in developing the recipe for our particular application. These materials use stoichiometric TiN proximitized with pure Ti to produce films that have the desired critical temperature without the careful nitrogen flow control required for sub-stoichiometric TiN.

4.4.2   Niobium

For the readout transmission line and the groundplane/backshort the material requirements were much less stringent than for the detector resonators. A material with a T_c reasonably far above the bath temperature is required to minimize electrical loss. Beyond that, the goal is merely to select a material that is relatively inexpensive, easy to fabricate, and which can be patterned using only processes compatible with the other layers. Niobium easily meets all of these requirements and was therefore selected as the transmission line and backshort/groundplane material. In geometry B, when a 'test resonator' was added, Nb was also used for the test resonator material since it could be fabricated as part of the transmission line layer, thus avoiding the addition of an extra layer of lithography. The groundplane needs to be thick enough to prevent electric fields from penetrating the film and interacting with the relatively lossy normal metal copper of the chip holder. The London penetration depth in Nb is 390 Å. The frontside Nb merely needs to be thick enough to be a high-quality continuous film. 5000 Å of Nb was deposited for the groundplane on the backside of the wafers and 2000 Å was deposited on the frontside of the wafers for the readout line and test resonator.

4.4.3 Ti/Au

As described in section 4.2.2.2, Ti/Au is used for the large heat sinking pads in the corners of each chip. Gold is used for its excellent thermal conduction and resistance to oxidation. However, gold on its own does not adhere well to silicon because of the mismatch in their lattice spacing. A very thin layer of Ti (about 60 Å in this case) is used as an intermediate layer to improve the gold adhesion. Because the Ti layer is so thin, it has a negligible effect of the ability of the pad to conduct heat away from the chip. The Au layer thickness seeks to balance the high cost of depositing gold films with the need for a layer thick enough to assure easy wirebonding and good thermal properties.

4.5   Diagnostic Features

4.5.1   Off-chip

Several diagnostic features are included in the mask design outside of the actual detector chips. The main diagnostic feature is a set of four diagnostic chips located near the outer edge of the wafer. Each diagnostic chip features one 20-square 4-wire resistance measurement structure for each front-side material (Ti/Au, Nb, and resonator material), one 5000 $\mu m \times$ 5000 μm square of Nb and one of the resonator material (useful for additional resistance measurements or miscellaneous other tests), and a critical linewidth feature made of a series of 2- and 4- μm lines and spaces used for evaluating photoresist over/under development and over/under etching.

In addition to the diagnostic chips, at the top of the wafer there are two large squares. One of Nb and one of the resonator material. These features are large enough to be used for ellipsometry measurements even after the wafer has been etched. They are visible at the top of figure 4.8.
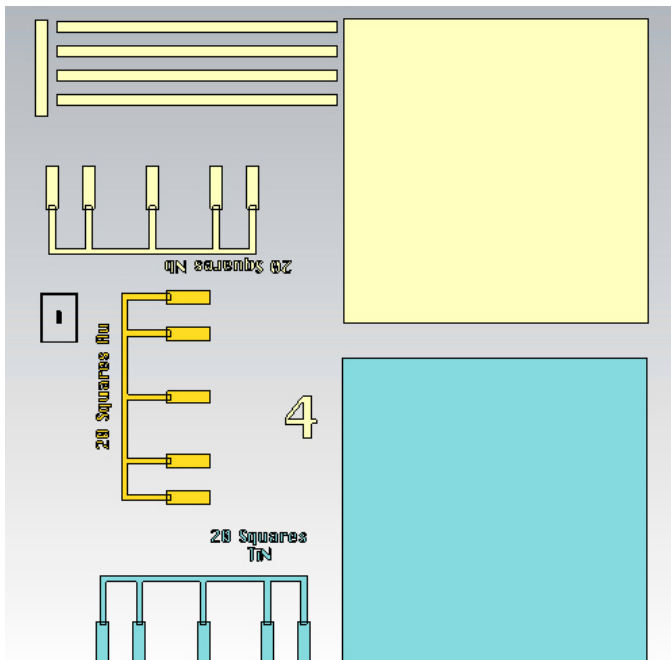
Figure 4.6: Diagnostic chip layout, including 4-wire structures for all three lithographed layers, larger squares for miscellaneous diaagnostic use, and critical linewidth features (small box in the center left).

4.5.2 On-chip

In addition to the off-chip diagnostic features, there are several diagnostically useful on-chip features. In both designs A and B there is a small rectangle, 1500 $\mu m \times$ 3200 μm, of resonator material away from the resonators, at the edge of the chip between the ends of the readout line. This has proven useful for miscellaneous checks of film quality or resistance in cases where there was concern there might be important differences between the film on the detector chip and on the diagnostic chip. In the same area, there are also a few small rectangles of Nb, with the same width as the readout microstrip line. These are useful for tuning wirebonding settings before attempting the connections from the chip to the Duroid circuit board which acts as an interface between the chip and the SMA connectors mounted in the wall of the chip package.

An additional on-chip diagnostic feature was included in design B only. One TiN/Mo resonator was replaced with a Nb resonator (of identical geometry). This is useful for diagnosing whether any
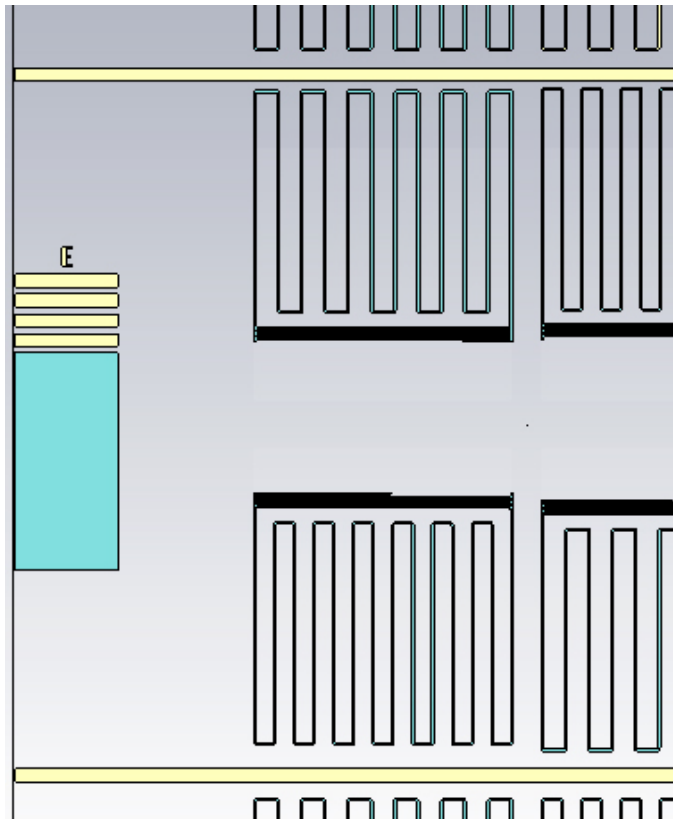
Figure 4.7: On-chip diagnostic features (center left), including a rectangle of resonator material (light blue) and four Nb strips for wirebonding practice (light yellow).

problems with resonator quality arise from a whole-wafer problem or from an issue just with the film quality of the resonator material. Nb was chosen for this "test resonator" for several reasons. First, we were already putting Nb on the frontside of the wafer for the readout line, so the diagnostic resonator is included in that mask, avoiding the need for an additional lithographic layer. Nb is also a relatively easy film to grow, isn't excessively sensitive to impurities, and reliably exhibits a very high internal quality factor. In other words, if the Nb resonator doesn't work, and there aren't any obvious lithographic flaws, chances are good that the problem is not with the Nb film but rather with one of the other layers or processing steps.

4.6   Fabricated designs

There were two geometries fabricated over the course of this project. The first geometry, called geometry A in this chapter and those following, was a first pass based on an earlier design by Doyle [91, 92], adjusted to meet our specifications. Specific geometric parameters were chosen based on the simulations and semi-analytic calculations described above. Later, a second geometry was designed and fabricated, called geometry B in this chapter and those following. Geometry B is a very close sibling of geometry A, but has a number of adjustments motivated by measurements of geometry A and various bits of wisdom that came with an additional year of thinking about KIDs.

4.6.1   Geometry A

Wafers in geometry A have six detector chips and four diagnostic chips. Each of the six detector chips has 20 detector resonators made of either Mo or TiN. Eight of the resonators have 14 meanders, one has 12 meanders, and eleven have 10 meanders. They all have between 5 and 6 capacitor fingers, and had anticipated frequencies between 422 MHz and 532 MHz, with anticipated coupling Qs between 4000 and 790,000. See figure 4.1.

4.6.2   Geometry B

After testing of geometry A, several potential improvements became apparent. In particular, the corners of the resonators were rounded off to reduce the high magnitude electrical fields produced at the sharp corners of geometry A. In addition, a niobium 'test resonator' was added, as discussed in section 4.5. Based on the empirical results from testing of geometry A, the coupling distances were adjusted and the resonators were placed closer together in frequency space. Finally, one of the six detector chips was fabricated with only 12 pixels instead of 20. The idea was that by spacing the resonators farther apart geometrically, we could compare to the closer-packed chips and evaluate the effects of pixel-pixel cross-coupling, however due to time constraints, this test was never performed.
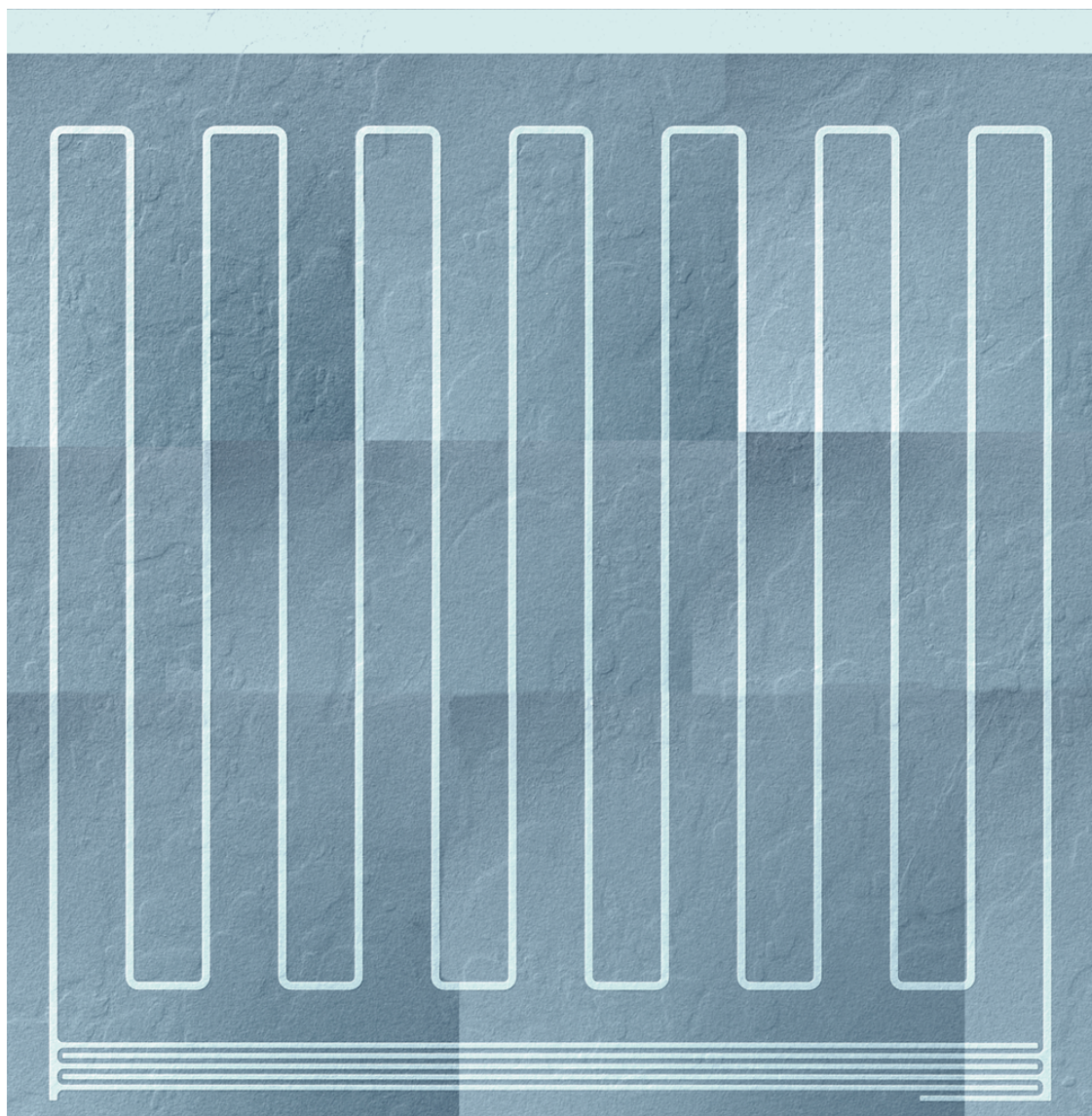
Figure 4.8: Composite micrograph of a pixel from geometry B.
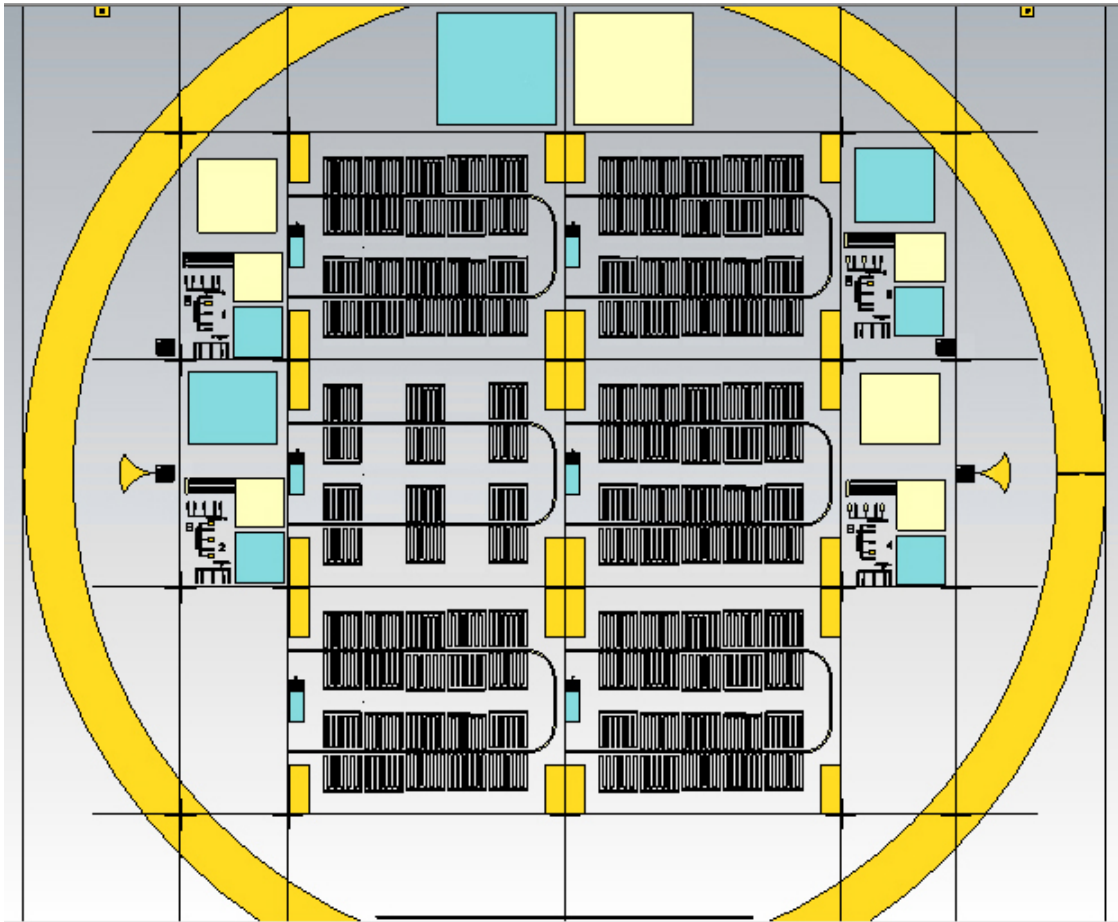
Figure 4.9: Layout of the full wafer for geometry B. Note the six detector chips in the center and four diagnostic chips on the sides. The long straight lines crossing the entire wafer are dicing guidelines which are part of the Ti/Au layer.

4.7 Package Design

In order to cool a chip and transmit RF power onto and off of it, one must have a way to hold the chip stably on the cold stage and a way to make electrical connections to and from the chip. To meet those needs, a custom connectorized chip package was designed. The package must make good thermal contact with both the chip and the cold stage and must have a minimal thermal time constant (high thermal conductivity compared to its heat capacity). To that end, OFHC (oxygen-free high conductivity) copper was selected for the bulk material of the package, with gold plating to enhance thermal contact. The package has a removable OFHC copper lid to allow for dark

tests (lid on) or illuminated tests (lid off). There is a "pocket" on the back side of the package to accommodate a piece of annealed Cryoperm magnetic shielding, and the OFHC lid can be replaced with another piece of cryoperm (with or without a beam waist-sized hole in the center to allow for illumination) to create a magnetically-shielded "sandwich" for the chip. Though we believe the field leakage from the ADR magnet's shielding is very small, especially in the direction normal to the surface of the chip, and we orient the Dewar so that the Earth's field is parallel to the surface of the chip, the Cryoperm sandwich cuts any remaining normal field component (either from ADR leakage or from imperfect Dewar orientation relative to Earth's field) by a factor of roughly three (see figure 4.10).

The package is connectorized with modified SMA connectors. We operate without the PTFE dielectric in the section of the connector that passes through the package wall (instead using just pin-in-vacuum) in order to increase the "give" of the pins at the solder connection to the Duroid board (described below). This makes it significantly easier to install the Duroid board and reduces strain on the pin-board connection. On the other hand, the pin may not sit perfectly centered in the outer conductor, which may cause a small impedance mismatch. Care is taken before closing the package to adjust the pin position with tweezers in order to minimize the off-center position and hence the mismatch. The biggest drawback to this design, however, is that because of the difference between the electrical permittivity of PTFE and the electrical permittivity of vacuum, the vacuum-filled hole (outer conductor) must have a much smaller diameter than a PTFE-filled hole would have needed. Our pin diameter is constrained by the requirement that we can solder it to the traces on the Duroid board. The width of the traces on the Duroid board is constrained by the requirement that they have an impedance of 50 Ω, by the limited options in terms of standard Duroid thicknesses commercially available, and by the requirement that the traces on the Duroid be similar in width to the microstrip readout line on the detector chip (for practicality in wirebonding). These constraints together set the pin size to a 0.009" diameter (0.005" in the end section that solders to the copper traces on the Duroid). To achieve a 50 Ω impedance with a vacuum dielectric and a 0.009" inner conductor, this requires an outer conductor diameter of just 0.021". The wall of the package is 0.125" thick, so the fabrication requirement is that two 0.125" deep through holes of
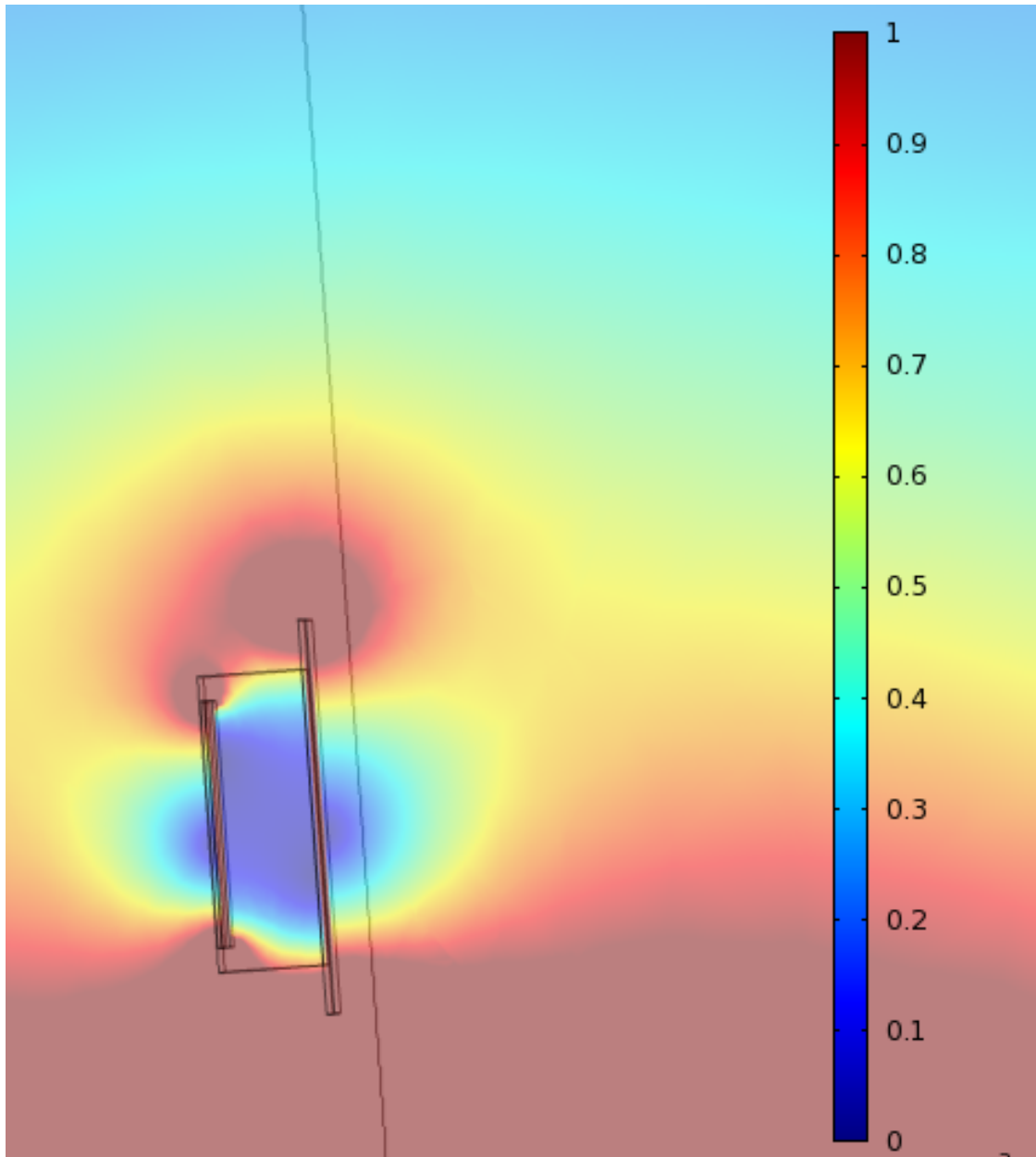
Figure 4.10: Simulation by Brandon Melcher of the effect of the cryoperm shields on magnetic fields in the vecinity of the chip, which is located on the inside of the box. The shields cut the field magnitude by roughly a factor of three near the chip.

diameter 0.021" be drilled through the OFHC package wall. A 21 mil ream is very tiny and very delicate indeed, and OFHC copper is notoriously gummy and difficult to work with, even when using more reasonable-sized tooling. We found the drilling of this hole to be possible, but after ruining the first attempted package at the last step with a broken-off drill bit, we found that only a mill properly tuned up to have supremely low chatter is up to the delicate task. Following machining, the package is thoroughly cleaned and degreased, and then gold-plated to improve thermal contact both from the chip to the package and from the package to the cold bath. Machining of the package was carried out by then-undergraduate Brandon Melcher.

In order to bridge the gap from the detector chip to the solder-pin connection on the SMA connectors, we used a custom Duroid circuit board. For practicality of wirebonding, we wanted a 50 Ω trace on the board to have a similar width to the 50 Ω line on the detector chip, while maintaining a board thickness similar to the Si thickness. This requires finding a material with an electrical permittivity similar to that of Si ($\epsilon_{Si} = 11.4$). Rogers Duroid 6010 is a composite ceramic material with a permittivity of $\epsilon = 10.4$. It is readily available commercially in the convenient thickness of 0.01" (0.25 mm), pre-clad with 1/2 oz copper on both sides. The front side of the board was patterned, etched, and diced by Joseph Suttle in WCAM using a mylar 20,000 dpi laser printed photolithography mask from Infinite Graphics of Minneapolis, MN. Three parallel aluminum wirebonds at each end of the microstrip connect the chip to the Duroid board.

The package is held in place on the cold stage by a gold plated OFHC copper L-bracket, machined by Brandon Melcher. The back (non-chip) side of the L-bracket is additionally used as a mounting surface for the cold stage thermometry, including the GRT thermometer and the Lakeshore thermometer. This thermometry mounting location has the advantage of having a relatively short thermal path to the detector chip.
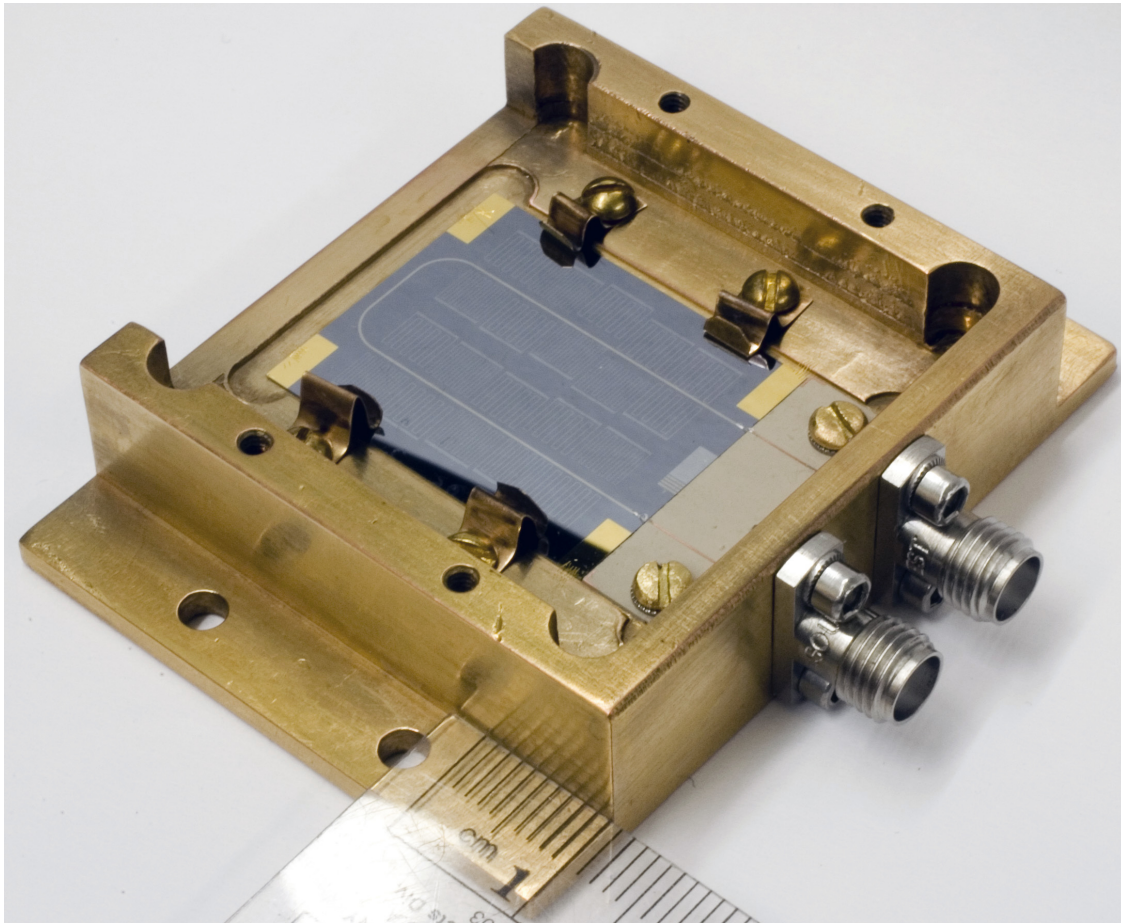
Figure 4.11: Photo of the chip holder package with a detector chip and Duroid board (tan-colored circuit board on the RHS) installed.

CHAPTER 5

─────

FABRICATION

5.1 Fabrication techniques

Microfabrication of any kind is invariably challenging. This is especially true for devices involving superconductors, which often need to be deposited in supremely clean and well-controlled environments in order to produce the intended film properties. While some of the materials used in this project are fairly standard (such as the niobium and gold layers), the materials used to produce the resonators are specialized materials developed specifically for good performance in high-Q resonators. However resonator internal quality factor is highly sensitive to the details of film deposition and processing. Careful and consistent control of every processing step is one of the largest challenges in fabricating KIDs and other microdevices.

Except where noted, all of the fabrication described in this chapter took place at the NASA Goddard Space Flight Center Detector Development Laboratory.

5.1.1 Metal Film Deposition

5.1.1.1 DC Magnetron Sputtering

DC magnetron sputtering is one of many techniques for growing thin metal films on silicon (or other) substrates. A rarefied noble gas (usually argon) plasma is struck in the deposition chamber. A disk of the metal to be deposited (the 'target') is attached to an electrode that is at a negative potential. Positive ions from the argon plasma are accelerated towards the target and strike it with such force that individual atoms are ejected from the target. These ejected atoms condense on any nearby surfaces. By placing the desired substrate near the target during this process, a film of the

target metal can be grown on the substrate. In magnetron sputtering, a magnetic field is used to confine the plasma which intensifies the bombardment of the target and increases the deposition rate. This also allows a plasma to be generated at lower pressures, which produces a cleaner film. In reactive sputtering, another gas in addition to the noble gas is introduced into the chamber. This gas can react with the ejected target atoms to modify the deposited material. This method is used with nitrogen gas and a pure titanium target to produce titanium nitride, for example.

For the devices described in this dissertation, DC magnetron sputtering was used to produce the Mo, TiN trilayers, and Nb films.

5.1.1.2 Electron Beam Evaporation

Electron beam (or E-beam) evaporation is another technique for growing thin films. In this process, an electron gun in a high vacuum is used to produce an electron beam. Electric and magnetic fields are used to aim the beam at a crucible containing the material to be deposited. The material is evaporated out of the crucible and condenses on every line-of-sight surface in the vacuum chamber.

For the decvices described in this dissertation, E-beam evaporation was used to produce the Ti/Au and Ge hard mask layers.

5.1.2 Photolithography

Photolithography in microdevice fabrication is a process used for patterning thin films. A photosensitive polymer coating, called photoresist, is applied to the surface of a wafer and exposed to bright UV light in some areas and shielded from light in other areas using a photolithographic mask. After chemical developing, the polymer is rinsed away in the areas that were exposed to light and left behind in the areas that were masked (or vice-versa if using a 'negative resist'). The pattern left behind in the photoresist is used to produce the same pattern in a thin film or in the substrate itself, usually using either an etch process or a liftoff process, as described in the sections that follow. Detailed recipes for all of the film depositions, patterning, liftoffs, and etch processes are provided

in appendix A.

5.1.2.1 Photoresists

Photoresists are photosensitive polymers used in photolithography. After exposure to bright light, the polymer can be washed away by a chemical developer, whereas the chemical developer has no effect if the polymer has been shielded from light. 'Negative resists' produce the opposite effect: areas of the resist which were shielded from light are rinsed away by the developer and areas that were exposed to light are left behind.

There is a vast variety of photoresistive chemicals commercially available and commonly used in microdevice fabrication. This section will only mention those resists used in the course of this project rather than attempting to give a complete overview. All of the resists discussed here are positive resists.

Adhesion promoters: HMDS, or hexamethyldisilazane, is used as an adhesion promoter since many photoresists do not adhere well to silicon on their own. GenARC antireflection coating is also used in a similar manner as an adhesion promoter. It is essential to bake the wafers either in an oven or on a hotplate just before using these adhesion promoters to be sure the wafer is extremely dry before application.

1811:   Dow Microposit 1811 photoresist is a common general purpose photoresist. It is the thinnest of the resists used in this project, which makes it especially good at capturing fine details and small features. For devices with the very smallest features, such as the mSQUID arrays used for evaluating resonator film properties (see section 5.2), the 1811 is further thinned using Dow Microposit P-thinner, which is a solvent intended specifically for thinning 1800-series photoresists.

1827:   Dow Microposit 1827 photoresist is chemically very similar to 1811, but is substantially thicker. While this makes it less useful for capturing fine features, it is useful for situations requiring
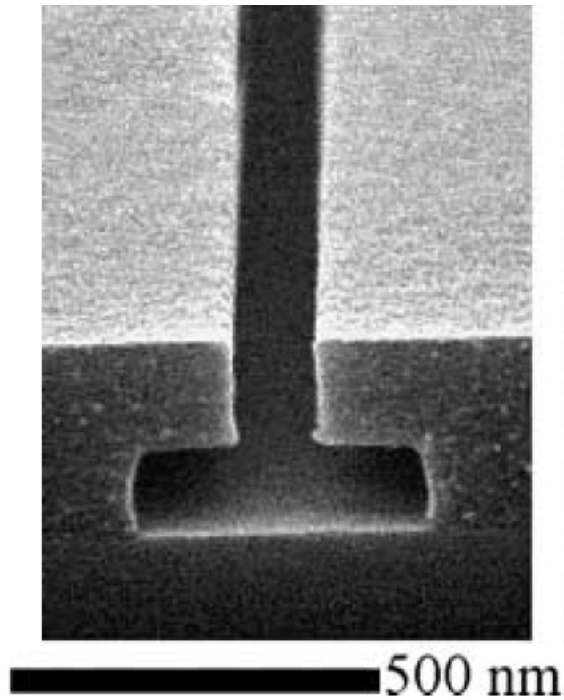
Figure 5.1: SEM micrograph of a bilayer resist undercut with PMGI. Figure adapted from [8].

a thicker or more robust coating, such as when the photoresist must survive especially aggressive processing or when a larger step height is needed for a multi-layer resist process.

PMGI: LOR-5A, which is a polymethylglutarimide-based, or PMGI, resist is particularly intended for bilayer liftoff techniques. A layer of PMGI is spun onto the wafer first, and topped with a soft-baked imaging resist (1811, in the case of this project). The bilayer resist is then exposed with a contact mask and developed. The goal in developing a bilayer liftoff mask is to form an 'undercut' where the top layer of resist overhangs beyond the bottom layer of resist so that the liftoff solvent can get underneath the metal-capped top layer of resist and contact the soluble resist to start the liftoff (see figure 5.1). With no undercut, there is a risk, especially with thicker metal films, that the metal layer will fully cap the resist and the solvent will be unable to reach underneath to lift the metal.

PMMA: PMMA, or poly(methylmethacrylate), is another resist for bilayer liftoff techniques, similar in usage to PMGI. In this project it was used as the under-layer for the Ge hardmask in the Nb liftoff process.

5.1.2.2 Photolithography masks

Photolithography masks are used to make patterns in photoresist for photolithographic processing. The mask is placed in contact with the photoresist-coated surface and blocks light in some areas while letting it pass through in other areas. A variety of materials and resolutions are available for photolithography masks. For low-precison tasks, a mask can be made as simply as laser printing or even drawing by hand on an acetate overhead projector transparency. For slightly more precision, mylar masks with up to $\mathcal{O}(100{,}000)$ dpi laser printing can be ordered from specialty printing companies. It was this type of mask that we used to pattern the 50 Ω traces on our Duroid transition boards. When mylar masks with laser printing are insufficient, chrome-coated soda lime glass or quartz can be ordered from commercial photomask companies with various resolutions which inversely correlate with price. With the exception of the mylar mask for the Duroid board, all of the masks used in this project were chrome-coated quartz with $\pm$ 0.2500 μm tolerance, purchased from commercial photomask company Photronics, Inc.

5.1.2.3 Exposure and development

For high-precision fabrication processes requiring careful alignment from one layer to the next, purpose-built mask aligners are used. These devices hold a quartz photolithography mask and a wafer with a very small air-gap between them. Alignment marks are etched directly into the silicon of the wafer as a first step before any other lithographic steps. For all subsequent lithographic layers, alignment marks on the photomask are aligned to the marks in the silicon (see figure 5.2). Cameras built into the machine view the alignment marks in the mask and in the Si wafer and display them on a split screen monitor. Buttons or a joystick are used to make fine adjustments to the position

of the mask relative to the wafer until satisfactory alignment is achieved. The mask aligner then presses the wafer directly against the mask so that the features come out as sharp as possible. Then the mask aligner shines a bright mercury lamp through the mask onto the photoresist for the specified exposure time.

After the wafer has been exposed, it is developed. For these devices, two primary methods of development were used: spray developer or so-called 'bucket developer'. The spray developer is a machine that holds a single wafer with a vacuum chuck and spins it while spraying MF317, a tetramethylamonium hydroxide-based (TMAH) developer, followed by DI water, each for a specified amount of time according to pre-programmed recipes. Bucket developer refers to developing by hand. MF312, another TMAH-based developer, is mixed in a 1:1 ratio by volume with DI water. Then wafers are placed, usually one at a time, in the developer for a specified amount of time or until the alignment marks visually clear. Some recipes call for sirring or agitating the solution during development (usually by stirring with the actual wafer and wafer holder) and some call for still developer. Whether using spray or bucket developer, the wafers are always immediately placed in a cascade DI water rinse following development to ensure that any remaining traces of developer are removed and the development reaction ceases.

After developing, the wafer is inspected to check for correct exposure and development. For this purpose, a critical linewidth feature is included on the diagnostic chips on each wafer. This feature consists of a series of 4 μm and 2 μm lines and spaces. When the exposure and development are correct, the lines and spaces should be equal in width (see figure 5.3). If the lines are too wide compared to the spaces, the photoresist was either underexposed or underdeveloped. A general visual inspection of the wafer is also undertaken at this point, with special attention paid to any essential features in the layer being worked on. If there are any flaws in the photoresist (from dust particles, incorrect exposure or development, 'comets' from spinning photoresist, etc), the resist can be stripped with a solvent rinse, re-spun, and re-exposed at this stage with no lasting damage to the wafer. Proceeding beyond this point with flaws in the resist will make those flaws a permanent feature of the wafer.

If the patterned resist is deemed acceptable after inspection, the wafer is ready for either etching
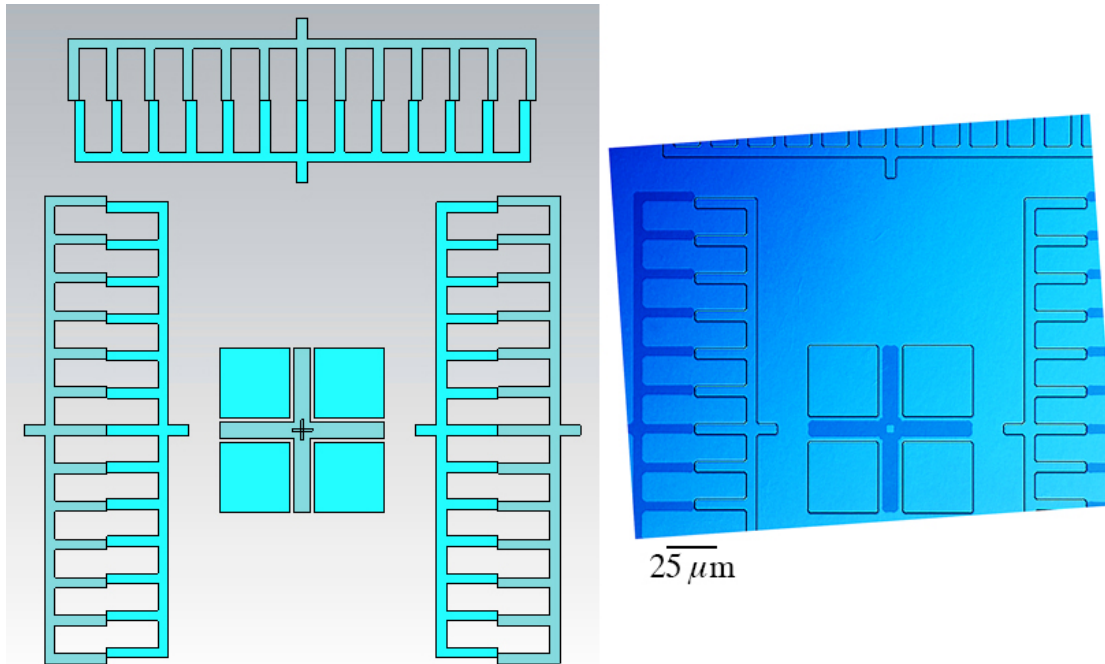
Figure 5.2: **Left:** Layout of an alignment mark. The ligher blue areas are etched areas in the Si wafer. The darker blue areas are the resonator material. Perfect alignment (shown) is when the cross at the center is perfectly centered in the four boxes and when the middle line on the combs at the right, left, and top are all perfectly in-line. **Right:** Micrograph of part of an alignment mark on an actual wafer. The dark blue areas are TiN trilayers and the light blue areas with black outlines are etched Si. The background is unetched Si.

(for an etch process) or film deposition (for a liftoff process).

5.1.3 Etching and liftoff techniques

5.1.3.1 Reactive ion etching

We used reactive ion etching for the Mo, Si, Nb, and Ge films in this project. Reactive ion etching (RIE) uses a chemically reactive plasma to etch materials on a wafer. A RF electromagnetic field is used to strike a plasma in a low pressure chamber. Ions from the plasma bombard the wafer surface and react with it. Common etchants for RIE are CF_4 and SF_6. We used RIE for several etching steps including some of the frontside Nb, etching the alignment marks into the Si wafer, some of the
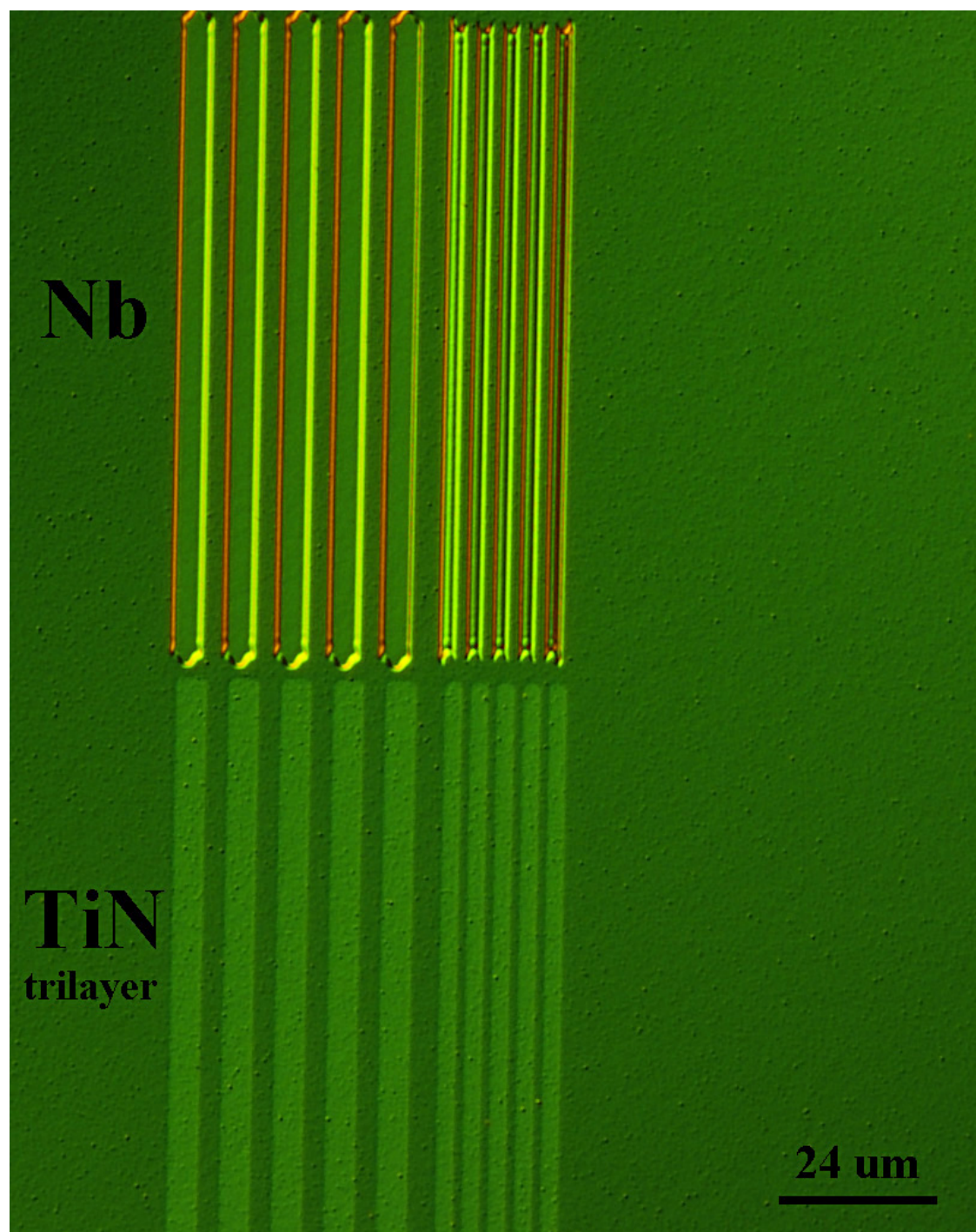
Figure 5.3: Micrograph of critical linewidth features for the TiN trilayer and frontside Nb layers. This example is from a wafer with etched Nb rather than liftoff Nb. We believe the pockmarks in the Si are caused by the Nb dry etch. The dark green background is the Si substrate.

Mo, and the final, successful etch recipe for the TiN trilayers.

To make the alignment marks into the silicon, we use an SF_6-based etch. We also used SF_6 for the Mo dry etch and to etch the Ge hardmask used for the Nb liftoff. A CF_4-based etch was used for the Nb dry etch. To etch the TiN trilayers, we used a slightly different piece of equipment; the Trion etcher uses an inductively coupled plasma, where the plasma is struck by a RF magnetic field, to drive the reactive ion etch. This recipe uses BCl_3 and Cl_2 to achieve a complete etch of the TiN trilayer without leaving a shorting residue, unlike the other etches we tried. In general, the goal in selecting process gases for RIE is to choose an etchant that will attack the material you intend to etch much faster than any other material already on the wafer.

5.1.3.2   Liquid etchants

We used liquid etchants for some of the molybdenum and some of the TiN layers.

For molybdenum, we tried both a wet and a dry etch. For the wet etch, we used E6, which is a mixture of nitric, phosphoric, and acetic acid and water. The E6 is heated to 45 C and agitated with a stir bar at 200 RPM to ensure even etching. It takes only about 5 seconds to etch through such a thin layer of Mo. The etched wafer is immediately submerged in a DI water cascade rinse to remove any remaining etchant and quickly stop the etch process.

For TiN, one of several etch processes we tried was a wet etch with hydrochloric acid, hydrogen peroxide, and DI water. This mixture is also commonly known as SC2 or 'standard clean 2.' This etch takes about three minutes at 65 C. As with other wet processing, the wafers are rinsed in a DI water cascade rinse immediately upon removal from the etchant. Unfortunately, as discussed in section 5.2, this etch for TiN left a conductive residue which shorted out the resonators, and therefore was not used on any of the successful wafers.

5.1.4   Liftoff

In liftoff processing, photoresist is spun on the wafer and patterned first. Then, a metal film is deposited over top of the patterned photoresist. Finally, the wafer is bathed in a solvent. The solvent dissolves the photoresist, lifting off the metal film that sits on top of the resist. Metal that is deposited over parts of the wafer that are not covered by photoresist should be fully adhered to the wafer and will remain so during the solvent soak. Sonication or agitation of the solvent with a pipette can be used to help fine features lift off more completely. The Ti/Au heatsinking pads on the prototype detector chips and the frontside Nb later in later versions of the fabrication procedure were both made with a liftoff process.

For the Ti/Au thermal contact pads, HMDS is applied followed by a layer of LOR-5A. The LOR-5A is topped with 1811 and the wafer is soft baked to prepare the resist for exposure. After exposing the resist in the mask aligner, and developing, we inspect the photoresist. Ideally, under magnification a dark line should appear at the edges of the resist. This is indicative of a good undercut which will make the actual liftoff step much easier. It can be helpful to humidify the wafers overnight before loading in the E-beam chamber to help prevent cracking of the resist during the deposition. The chamber is loaded with two separate crucibles: one with titanium and one with gold. Wafers are loaded face-down into the carousel at the top of the chamber. After pumping down for at least several hours or overnight, we first deposit a thin layer, about 60-200 Å, of Ti to aid in adhesion of the Au. Next, we deposit about 1200 Å of Au. The system is allowed to cool for several minutes before breaking vaccuum. To perform the actual liftoff, the wafers are soaked in acetone for several hours or overnight. Agitation with a pipette is used to help any stubborn areas, such as areas around small features, lift off more fully. Since the Ti/Au has no critical features in this design, we didn't need to be especially careful about making sure every last little feature fully lifted off. For some of the wafers, the Ti/Au liftoff was performed with just a layer of 1811, without PMGI underneath because the lab was out of PMGI. While the edges of the gold features on those wafers were slightly more ragged than on wafers where the full bilayer resist stack was used, since there were not critical features on the gold layer, the time saved by not waiting for the
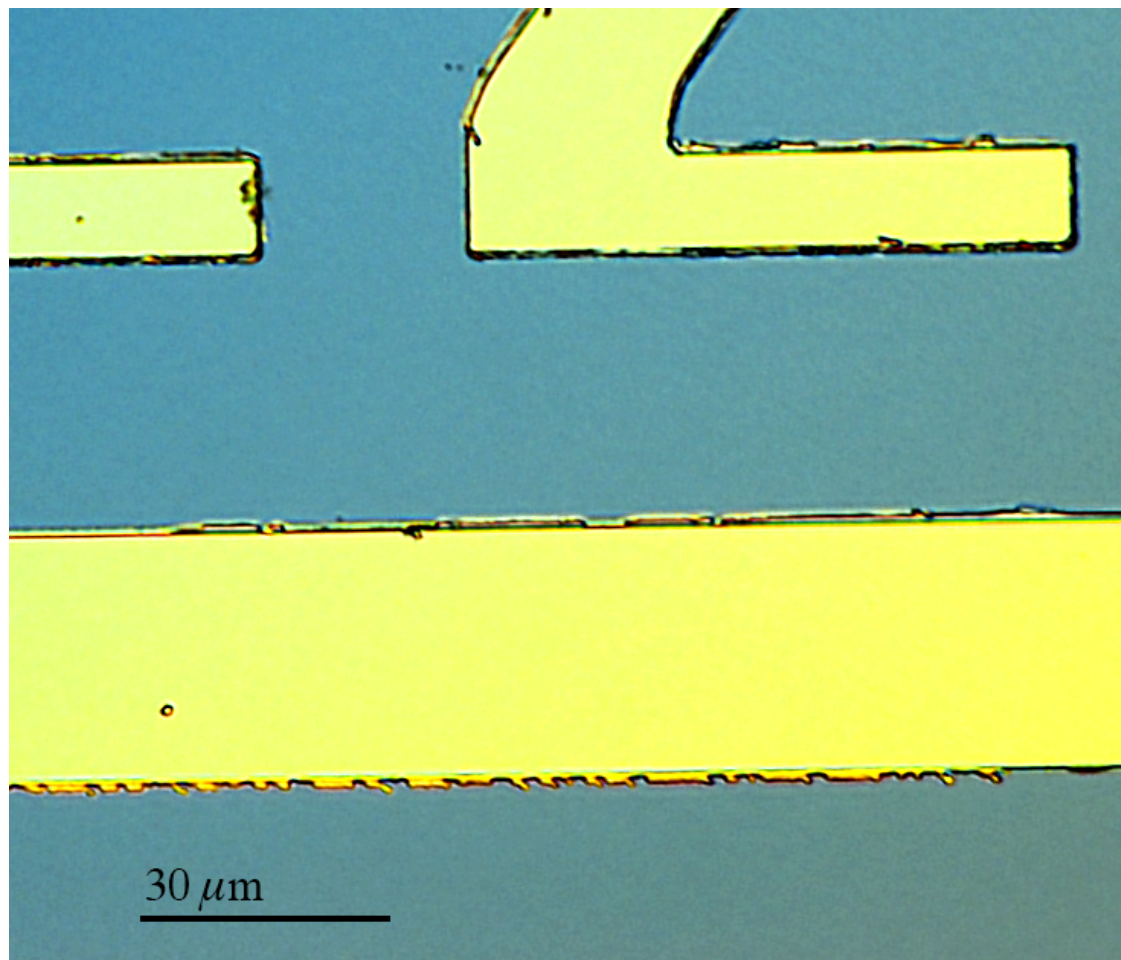
Figure 5.4: Micrograph of the ragged edges left on the Ti/Au layer for wafers where the liftoff was done with 1811 only instead of the bilayer resist stack.

PMGI shipment was more valuable than perfect heatsinking pad edges (see figure 5.4).

Wafers made early in this project used a dry etch process for the Nb. However, we found that the product wafers had pock marks which we believe were from the Nb etch process. This motivated the switch to a liftoff process for the Nb for the final set of product wafers. The niobium liftoff uses a germanium hard mask. First, the wafer is coated with PMMA resist and humidified overnight. Next, a layer of germanium about 1270 Å thick is deposited in the E-beam evaporation chamber. The germanium is coated with thinned 1811 photoresist and the 1811 is exposed and developed in the usual way. Next, an SF_6-based RIE dry etch is used to etch the Ge anywhere not protected by the 1811. This etch does not go through the PMMA that sits underneath the Ge, so the underlying

Si wafer is protected and won't be pockmarked as it was in the non-liftoff Nb process. After the Ge etch, the PMMA is removed using an O_2 ash in the RIE. Finally, we coat the wafer with sputtered Nb and lift off by soaking in acetone, which dissolves the PMMA underneath the Ge.

5.2 TiN films study

5.2.1 Single-layer substoichiometric TiN

Many TiN KIDs use single-layer TiN. To tune the critical temperature of TiN is is possible to limit the nitrogen flow in the chamber during deposition, which reduces the amount of nitrogen in the final titanium nitride material, producing substoichiometric TiN_x. With this method, the T_c can be varied between the T_c for pure Ti, 0.4 K, to the T_c of stoichiometric TiN, 4.5 K [53]. However, T_c over most of this range is *very* sensitive to nitrogen flow rate, which makes it challenging to develop recipes at specific T_cs, and makes film parameters highly sensitive to small changes in chamber condition. For this reason, we chose not to attempt to use single-layer substoichiometric TiN, even though in principle it was an option for these devices.

5.2.2 Trilayer TiN

Because of the fabrication challenges associated with single-layer TiN outlined in the previous section, we chose to use TiN trilayers instead. With trilayers and other multilayers, thin layers of pure Ti and stoichiometric TiN are stacked together. If the layers are thin enough, they will proximitize and share their superconducting properties across all layers (see chapter 4 for more detail). We used work by Mike Vissers [43] as a starting point for our trilayer recipes.

The critical temperature and normal state sheet resistance of TiN trilayers are very sensitive to chamber and target condition, especially when some or all of the layers are very thin ($\sim$10 nm or less). TiN and TiN trilayer recipes had been previously developed by Ari Brown and Vilem Mikula at GSFC using their AJA load-locked sputtering chamber. However, following repair of a small leak

	T_c	RRR	R_s
3/8/3 nm	1.22	1.3	68.0
3/8/3* nm	1.26	1.3	58.7
3/10/3 nm	1.18	1.4	53.7
3/10/3* nm	1.16	1.2	44.7
3/12/3 nm	1.16	1.3	34.4

Table 5.1: Critical temperature (T_c), residual resistance ratio (RRR), and sheet resistance (R_s) for five TiN trilayer recipes. The starred recipes included a Si surface nitridization step before the first TiN layer. All three layers are deposited in succession without breaking vacuum.

in the chamber, the chamber condition changed and film properties for those recipes needed to be re-established. It was necessary to adjust the previously-developed recipes and measure the new T_c and R_s until we found a new recipe with parameters suitable for this KID design. Films were deposited by Ari Brown and Vilem Mikula. The trilayers consisted of a (nominally) 3 nm layer of stoichiometric TiN, a layer of pure Ti with thickness varied between 8 and 12 nm depending on the recipe, and another 3 nm layer of stoichiometric TiN. I checked the room temperature sheet resistance of the trilayer film and then patterned and cleaved the wafers. Some of the samples were mounted for DC Tc checks by Aaron Datesman so that I could measure the Tc in an adiabatic demagnetization refrigerator at GSFC, which Jay Chavernack generously allowed me to use. The remaining samples I brought back to Wisconsin for testing in our Madison cryostat. Results of tests of 5 TiN trilayer recipes are summarized in table 5.1.

I made one wafer of KID prototype arrays of geometry B with recipe 3/10/3*, which was the best match to the goal film properties of $R_s = 40\Omega/\square$ and 0.8 K$< T_c <$ 1.2 K. Unfortunately, a conductive residue was shorting out the resonators, making the wafer unusable. We believe that the wet etch for the TiN leaves behind a very thin layer of conductive titanium silicide. We tried a reactive ion etch using CF_4 to clear the residue on one sample chip from the product wafer, and tried a short dip in dilute HF on another sample chip. Unfortunately, the RIE did not clear the residue. The HF dip was able to successfully clear the residue, but the TiN was damaged faster than the residue cleared, so it wasn't possible to remove the conductive residue without damaging the TiN resonators. Following our inability to clear the residue without damaging the resonators, Ari Brown and Vilem Mikula made a new set of test parts with the same TiN recipes, but a new

etch process that combined a wet and dry etch. Unfortunately, while this new etch process did clear the residue and yielded samples with good DC properties, the etch produced an undercut so severe that the RF properties were destroyed for smaller features (of order 10 μm). Finally, Ari and Vilem made yet another set of test devices with a new BCl_3/Cl_2 dry etch process which they found to fully clear the conductive residue without producing an excessive undercut.

DC testing of the BCl_3/Cl_2 etched TiN trilayers yielded results as in table 5.1. Ari and Vilem also produced RF testing structures using a single-layer CPW mSQUID mask which is commonly used by the KID group at NASA Goddard for studying RF film properties and was designed by Kongpop U-Yen. The mSQUID chips have 16 resonators in the low GHz range with a variety of coupling Qs from 5300 to 100 million. Goddard also loaned a SMA-connectorized package designed to hold the mSQUID chips. Fitting the mSQUID package in the Madison cryostat required only minor modifications to the L-bracket and RF SMA lines on the ADR stage. Measurements of the Qs of the mSQUID resonators serves as a method for evaluating the film quality without having to fabricate a whole multi-layer prototype array. We selected two of the recipes for RF testing of the corresponding mSQUID chips: 3/10/3 and 3/10/3*. Unfortunately, I was not able to test these two samples at the same bath temperature, so a really fair comparison can't be made between the two recipes based on these tests. The 3/10/3* recipe at 167 mK had a maximum combined Q of 100,000 compared to a theoretical maximum Q of about 850,000 for ideal coupling at that bath temperature and with that T_c and R_s. The 3/10/3 recipe at 304 mK had a maximum combined Q of 10,000 compared to a theoretical maximum Q of about 25,000 for ideal coupling at that bath temperature and with that T_c and R_s.

CHAPTER 6

——

TESTING APPARATUS

6.1 Cryogenics

The field of Low Temperature Physics is unique as one of the few areas of physics were Man has bested Nature; the lowest temperature known to naturally occur in the universe is that of the cosmic microwave background radiation, at 2.7 K. Yet macroscopic samples of condensed matter have been cooled to a few μK, and nuclear spin temperatures of a fraction of a nanokelvin have been reached in a laboratory setting.

6.1.1 Magnetic Cooling

Adiabatic demagnetization of paramagnetic salts is the oldest method of cooling significantly below 1 K. This method was proposed independently by Debye in 1926 and Giauque in 1927 and the first working system was achieved in 1933 [97].

The general principle is as follows [97]: Certain salts are paramagnetic; that is, their electronic spins tend to line up parallel to an applied magnetic field. The stronger the field, the more complete the spin alignment. To be more precise, the salt has some interaction energy, ϵ, of the paramagnetic ions with themselves and with the crystal which is small compared to kT at relatively high temperatures ($\gtrsim$ 1 K). Thus in the absence of a magnetic field, thermal randomness dominates, and a random distribution of dipoles results. However, if a magnetic field is applied such that the magnetic interaction energy, ϵ_m, is sufficient to overcome kT, ordering of the dipoles and a reduction in the entropy will result. If $\epsilon_m \gg kT$, then the dipoles will be strongly ordered and the spin entropy will be near zero.

This property - that the entropy of the salt can be significantly reduced by application of a

strong magnetic field - can be exploited to cool a sample. An apparatus using this cooling technique is called an adiabatic demagnetization refrigerator (ADR). The paramagnetic salt is housed in the center bore of a strong magnet, usually a superconducting electromagnet. While the salt is in thermal contact with an "intermediate" cold bath (such as a liquid helium bath), the magnet is gradually ramped up, exposing the salt to a strong magnetic field. This strong field causes the previously-disordered spins of the salt to align, while contact with the liquid helium bath prevents the system from heating up. A heat switch is then used to disconnect the helium bath from the salt and the cold stage (the section of the system to be cooled by the ADR). The magnet is slowly (adiabatically) ramped down to low- or no- field. In doing so, the spins of the salt relax and return to a disordered, high-entropy configuration. If the relaxation occurs slowly enough to be adiabatic, then entropy of the isolated [salt + cold stage] system is conserved. Therefore as the spins relax and the entropy of the spin system of the salt increases, the entropy of the cold stage and the lattice of the salt must decrease, which results in a significantly reduced cold stage temperature.

For a detailed discussion of fabrication and installation of our ADR see Grant Wilson's PhD thesis [98]. The ADR uses ferric ammonium alum (FAA) salt crystals grown in our lab in the 1990s and sealed inside a gold-plated stainless steel tube housing. The salt is grown on a matrix of gold wires which make thermal contact with the cold stage. A tensioned Kevlar suspension system holds the salt housing at the center of the bore of a 3 T magnet[1] while maintaining thermal isolation of the pill from the supporting structure. A similar Kevlar suspension scheme is used to provide mechanical support and thermal isolation to the cold stage. A purpose-built mechanical heat switch (also described in detail in the Wilson Thesis, see figure 6.1) makes and breaks thermal contact of the ADR and cold plate assembly to the helium bath.

6.1.2 The Blue Dewar

Affectionately known as the Blue Dewar, our laboratory cryostat is a modified IR Labs[2] HD-10 Dewar with 9 liter LHe tank and 4 liter LN tank. Factory modifications from the standard design

---

[1]American Magnetics, Oak Ridge, TN
[2]Infrared Laboratories Inc., Tucson, AZ
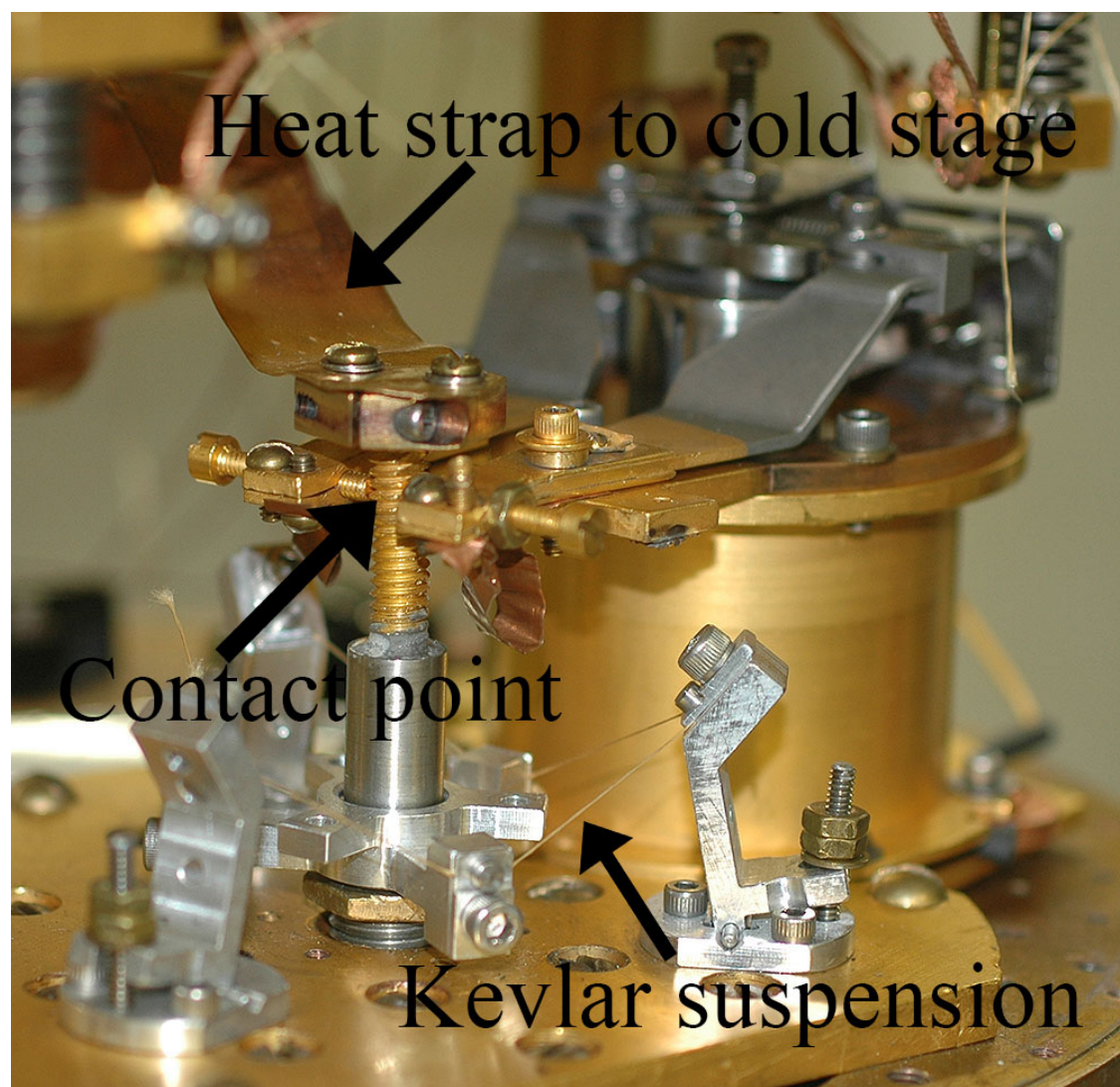
Figure 6.1: The Wilson heat switch

include six additional indium-sealed feedthroughs and a vent tube to the helium tank (in addition to the standard fill tube). Additionally, a number of further, after-market modifications have been made. Most critically, a home-built ADR was installed in the Dewar's youth in the mid-1990s. More recently, an additional indium-sealed feedthrough for RF and microwave coaxial lines for KID readout was installed in 2012 and one of the factory-modified additional feedthroughs was re-purposed as a microwave coaxial feedthrough in 2015. The RF and microwave feedthroughs are described in section 6.3 and the ADR is described in section 6.1.1. RFI is limited by using twisted pairs and low-pass filtering on DC lines.

Because it was originally part of the MSAM experiment's balloon-bourne cryostat, the Blue Dewar uses liquid cryogens rather than a dry refrigerator for pre-cooling before cycling the ADR. The ADR can be cycled starting from either 4.2 K or from ∼2 K if a vacuum is drawn on the LHe tank. Cycling from 2 K typically uses more liquid helium per ADR cycle and requires more intensive monitoring due to the risk of ice plugs over-pressurizing the liquid cryogen reservoirs. However cycling from 2 K significantly improves hold time and temperature stability, and slightly improves base temperature. A detailed description of the cooling and fridge cycling procedure, intended primarily as a reference for future operators of that specific instrument, can be found in appendix C.

6.1.3 Thermometry

Temperature monitoring of the cold stage is achieved using a pair of thermometers with complementary ranges. A Lakeshore Cernox ruthenium oxide RX-102A-BR thermometer monitored with a Lakeshore 218 temperature monitor is accurate over a range from 40 K to 4 K. For accuracy below 5 K, we use a germanium resistive thermometer (GRT) read out with a Cryocon62 AC resistance bridge. Additional uncalibrated thermometers located on the liquid helium and liquid nitrogen stages provide approximate temperatures used primarily for monitoring the liquid cryogen pre-cooling phase of operation.

The temperatures of the corrugated blackbody source and the collimator tube were also monitored with Lakeshore RX-102A-BR thermometers.
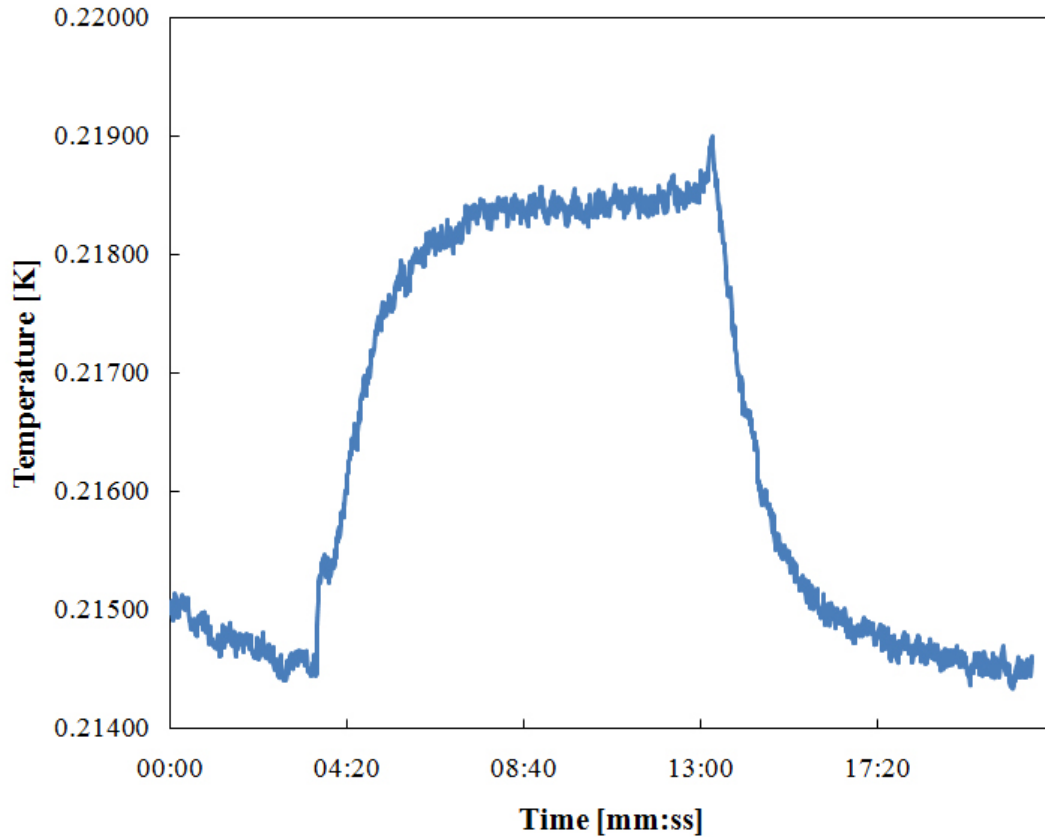
Figure 6.2: Thermal response of the cold stage to application of heat. 0.2μW of Joule heating is applied just before 4:20 and turned off at about 13:00. The thermal time constant is 42 s and the conductance from the cold stage to the salt pill is 51 μW/K. The quiescent heating of the cold stage over time has been subtracted out of this data as a simple linear correction.

6.1.4 Thermal Time Constant

Using a 10 Ω resistor on the cold stage to apply 0.2 μW at 215 mK, the thermal time constant was $\tau_{\frac{1}{2}}$=42 s and the conductance between the cold stage and the salt pill was 51 $\mu W/K$ (see fig 6.2).

For comparison, when the ADR was originally built and tested in the 1990s, the thermal time constant and conductivity from the cold stage to the salt pill were measured. With 0.1 μW of input power at 96 mK, the time constant was 51 s with a conductivity of 77.7 $\mu W/K$ [98].

6.2   Optical

There are several options when deciding how to deliver in-band photons to a detector.

Many experiments choose to use optical windows: large vacuum-tight ports in the side of the cryostat which are made of a material transparent in the relevant band and which have a view through all of the temperature shields and onto the detectors at the center of the cryostat. Optical windows are advantageous because all of the microwave electronics can live at room temperature and can be adjusted or serviced without warming or opening the cryostat. However they are prone to a number of failure modes including vacuum leaks, light leaks, condensation problems, and heat sinking or thermal loading problems. They also require drilling a giant hole in the side of your cryostat, which is its own logistical can of worms.

Another option is to install a hermetic waveguide feedthrough. In this case, a much smaller hole is drilled in the wall of the cryostat (and in each thermal shield on the way to the detector stage), and a hermetic waveguide feedthrough (available commercially) can be installed. The waveguide runs inside the dewar all the way to a point with a clear optical path to the detector (heat sinking at each temperature stage as necessary) and terminates in a horn antenna which shines on the detectors (possibly with a lens or two between the horn and the detector). Again, waveguide has the advantage that the microwave source is outside the Dewar at room temperature, where it can be adjusted or serviced even while the Dewar is closed and cold, though waveguide offers somewhat less flexibility than an optical window in the sense that you are strictly limited to the modes that your waveguide can propagate. In practice, unless you're trying to make a very broad-band detector, this isn't so much of a problem. Additionally, waveguide feedthroughs are prone to vacuum leaks, they are cumbersome in the sense that they take up a lot of space in the cryostat and have relatively large minimum bend radii compared to coax, and they are big chunks of metal which means they carry a large thermal load with them through each temperature stage.

Ultimately, we decided not to use either a window or a waveguide feedthrough. Instead, measurements were taken using two optical setups: First, a coaxial microwave feedthrough was fabricated to carry W-band (75-110 GHz) radiation from a room temperature sweeper outside the

cryostat to a coax-waveguide transition and finally to a horn antenna on the liquid helium stage. Second, a cold blackbody was fabricated, with DC heater power running from a room temperature power supply outside the cryostat to the blackbody located on the liquid helium stage.

6.2.1   Finline cold blackbody source

The finline blackbody source was designed and assembled by a previous graduate student, Emily Barrentine. A copper fin structure is lithographed onto a Kapton pc board (fabricated by Brigitflex), and a 100 Ω chip resistor is soldered across the fins near the base (see fig 6.3) and serves as a termination and source of the blackbody radiation. The assembly is inserted into the waveguide section that is just before the horn antenna in the optical chain, positioned parallel to the E-plane. The finline blackbody source has the advantage of exhibiting a relatively short thermal time constant, however because it uses the horn antenna for directionality, it suffers from all of the Gaussian beam optics complications of any other arrangement involving the horn. Partly for this reason, this blackbody option was never used for testing the samples discussed in this work.

6.2.2   Corrugated cold blackbody source

The corrugated cold blackbody source has the advantage of being beam-filling, which significantly simplified calculations of pixel response. The thermal time constant, while much longer than that of the finline blackbody source, is still practical at 60s. Design considerations for the corrugated blackbody were as follows: must fit in the limited space available on the 'diving board' (shown in figure 6.10) on the LHe stage; must have a heat capacity and thermal link to the LHe cold bath that allows for a reasonable thermal time constant without an excessive heat load on the helium bath; must have a controllable temperature between the LHe bath temperature and at least 6 K; must have a fairly constant temperature across the blackbody; must be reasonably black in the microwave frequency range.

Oxygen-free high conductivity (OFHC) copper was selected for the base structure of the
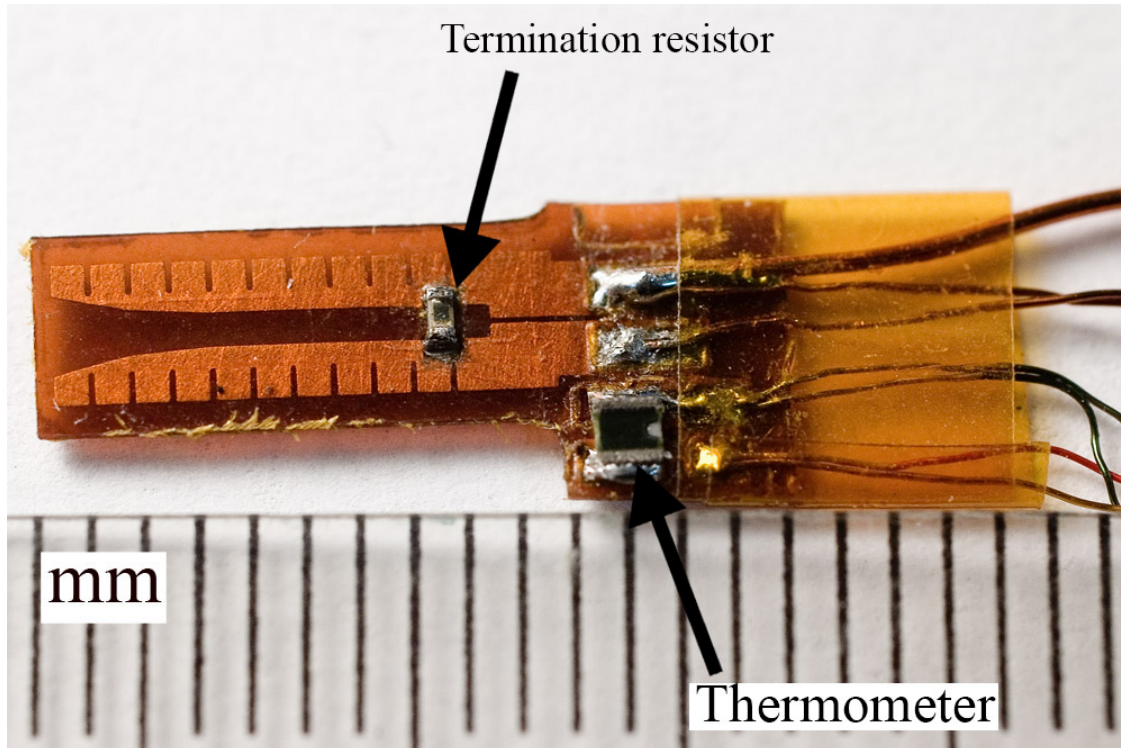
Figure 6.3: Finline blackbody source

blackbody. The high heat capacity isn't ideal, but using OFHC copper helps to ensure good heat conduction across the blackbody, minimizing the potential for hot spots and cold spots. Using a metal crimper, OFHC sheet stock was formed into a corrugated pattern, which helps increase blackness and reduce reflections of stray light by forcing incident light to bounce off of the blackened surface at least twice before escaping back into the open space in front of the chip. The copper structure is 1.8 inches tall and about 2.5 inches wide. The total mass of copper is 28 g. To blacken the chip-facing side of the corrugated copper structure, Eccosorb CR-117 iron-loaded epoxy was used. CR-117 was selected because of its good balance among viscosity (we want it to be 'paintable' for ease of application to the copper backing structure), heat capacity (the greater the amount of iron loading, the greater the heat capacity), and W-band blackness.

The CR-117 was prepared according to the manufacturer instructions and degassed in a vacuum chamber for several minutes. It was applied in several thin layers (fully curing between each layer), totaling approximately 2 mm thick over the 15 in^2 (96.8 cm^2) surface area of the chip-facing side of

Figure 6.4: Corrugated cold blackbody source

the copper support structure. The total mass of CR-117 (after curing) is 30 g.

To make the blackbody temperature-controllable, nine 100 Ω resistors are spaced evenly across the back (non-chip-facing) side of the blackbody and connected in series. They are affixed to the copper with small dots of degassed Stycast 2850 epoxy. A thin twisted pair of superconducting wires connects to existing DC feedthroughs on the LHe stage to allow for current input and control from outside the cryostat. A Lakeshore Cernox ruthenium oxide RX-102A-BR chip thermometer is affixed to the center of the blackbody using GE varnish and cigarette paper and the leads are routed to existing DC connections on the LHe stage.

OFHC copper has a specific heat of 2.28×10^{-3} J/gK at 6 K, down to 2.76×10^{-4} J/gK at 2 K [99]. Therefore, the 28 grams of copper in the blackbody have a heat capacity of 6.38×10^{-2} J/K at 6 K or 7.73×10^{-3} J/K at 2 K. CR-117 has specific heat of 4.8×10^{-3} J/gK at 6 K and 5.0×10^{-4} J/gK [100]. The 30 grams of CR-117 in the blackbody has a heat capacity of 0.015 J/K at 2 K and 0.144 J/K at 6 K. The heat capacity of the resistors, wires, GE varnish, Stycast, and

thermometry is negligible, therefore the total heat capacity of the blackbody is 0.21 J/K at 6 K and 0.023 J/K at 2 K.

A G10 foot is placed between the bottom of the blackbody and the LHe stage to regulate the thermal link between the two. To determine the best thickness and area for the G10 foot, a balance must be found between minimizing the blackbody's thermal time constant and minimizing helium boil-off due to heat load from the blackbody. We had scraps of G10 readily available with 1/16" (1.6 mm) thickness, so the primary parameter available for tuning the thermal link was the area of the G10 foot. To select an appropriate area, the calculations are as follows:

$$\tau = \frac{CL}{\kappa A} \tag{6.1}$$

where τ is the thermal time constant, C is the heat capacity of the blackbody, L is the length of the thermal link (the thickness of the G10 foot, in this case), κ is the thermal conductance of the link material (G10), and A is the area of the thermal link. G10 has a thermal conductance of κ=0.1 W/mK [97]. That leaves τ and A as the free parameters. Consider the 6 K case, since that will be the worst case; to achieve a time constant of $\tau \leq 60s$, the area must be $A \geq 56mm^2$.

On the other hand, the helium boil-off rate must also be considered. The latent heat of vaporization of helium is 21 kJ/kg and the density of liquid helium is 0.125 g/cm^3 [99], so it takes 2.96 kJ/L to boil off liquid helium. Supposing we allow for up to 0.05 W from the the blackbody, that's a contribution from the blackbody to the liquid helium boil-off rate of not more than 1 mL/min. Compared to the empirical quiescent boil-off rate from all other sources, roughly 10 mL/min, a worst-case contribution of 1 mL/min from the would be entirely reasonable.

The power flow through the thermal link is:

$$P = \frac{\kappa A \Delta T}{L} \tag{6.2}$$

where P is the power flow through the thermal link, ΔT is the temperature difference across the thermal link, and κ, A, and L are, as above, the thermal conductivity, area, and length (G10 thickness), respectively. Requiring P $\leq$ 0.05 W, and again using the worst-case 6 K values, leads

to the requirement that $A \leq 200mm^2$. So the area of the G10 foot must be between 56 mm^2 and 200 mm^2. The actual foot is 5mm $\times$ 30 mm $\times$ 1.6 mm, with two size-4 clearance holes to allow for fastening; an area of approximately 150 mm^2, which is well within this requirement.

To secure the blackbody to the diving board with minimal effect on the thermal link, teflon screws and teflon nuts were used. Spring steel Belleville washers were used between the screw head and the diving board surface to ensure a tight joint, even after thermal contraction.

To ensure that the detectors see only the blackbody and not stray light or light leaks from other parts of the cryostat, several measures have been taken. The lid and walls of the LHe stage have been painted with Bock black to help absorb stray light. Additionally, there is a Bock black-painted baffle to help mitigate any small light leaks that may come through the slit in the LHe stage lid where the RF coaxial cables pass though. Most importantly, when using the corrugated blackbody, the chip holder package is fitted with an Eccosorb-coated collimator tube and low-pass filter. First, a flat copper lid with a hole of radius 13/32" centered on the middle two pixels (see figure 6.5) is affixed to the front of the package. Next, a 117 GHz metal mesh low-pass filter made by P.A.R. Ade is placed over the hole in the lid. Finally, a second copper lid placed on top and the whole assembly screwed together. The second lid has a hole in the center to match the first lid. Protruding from the hole away from the chip and towards the blackbody is a copper tube 2.5 inches in length and 0.8 inch in inner radius. The interior of the tube is coated with 1.5-2 mm of CR-117 Eccosorb to further aid in absorption of stray light and collimation of the beam (see figure 6.6). To make certain that the collimator tube is well heat-sunk to the ADR stage, the collimator/filter assembly is attached to the chip package using Belleville washers and tightly-fastened brass screws. Additionally, there is a copper heat strap which more directly connects the second lid to the L-bracket that supports the chip package. The heat strap is fastened at both ends with tight brass screws and Belleville washers. To be certain that these measures were adequate, a thermometer was affixed to the collimator tube to allow for direct monitoring of the tube temperature during operation. The tube was found to be consistently within a few mK of the ADR stage.
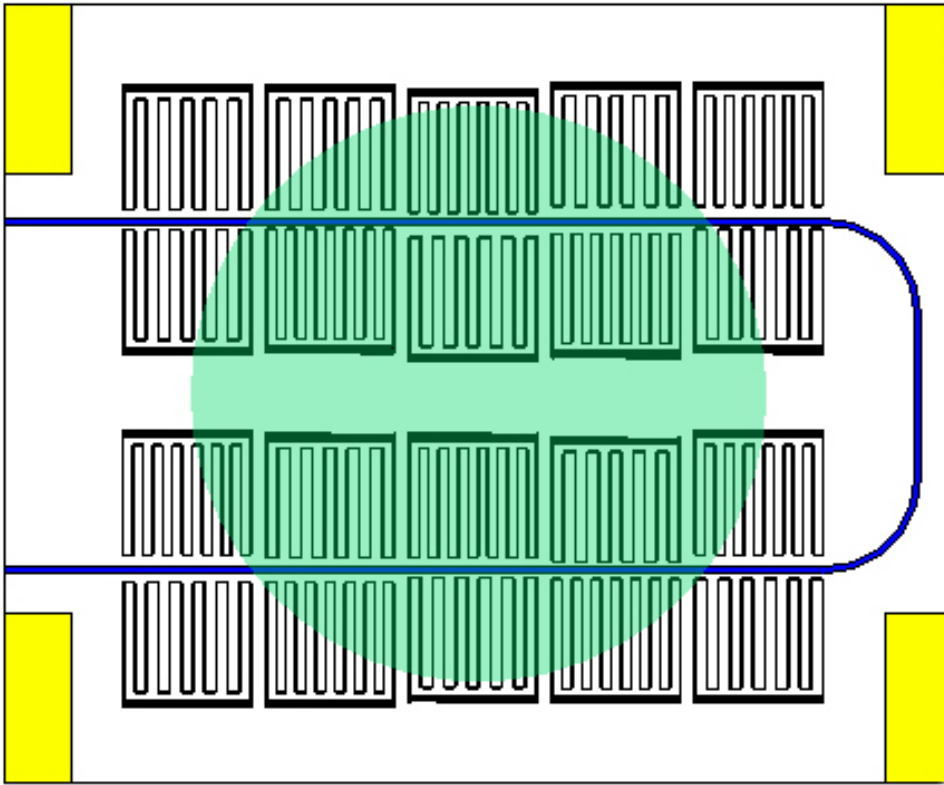
Figure 6.5: Drawing of the detector chip layout. The highlighted portion indicates the location of the illumination holes in the collimator/filter assembly lids.

6.2.3 Swept microwave source and coupling

6.2.3.1 Microwave source

A microwave synthesizer is used to provide swept or CW microwave radiation. The available synthesizer only goes up to 20 GHz, so a multiplier chain is used to bring the radiation up into the 100 GHz range. First,the output of the synthesizer is passed an active quadrupler[3]. Next, a passive doubler[4] is used. The active quadrupler has output power equal to the input power. The passive doubler has a typical input power of 16 dBm and maximum input power of 18 dBm. At 16 dBm input, the W-band (75-110 GHz) output is 1 dBm. The first harmonic content of the output is

---

[3]Milliwave OS5PO FA-10608
[4]Millitech MUD-10-1
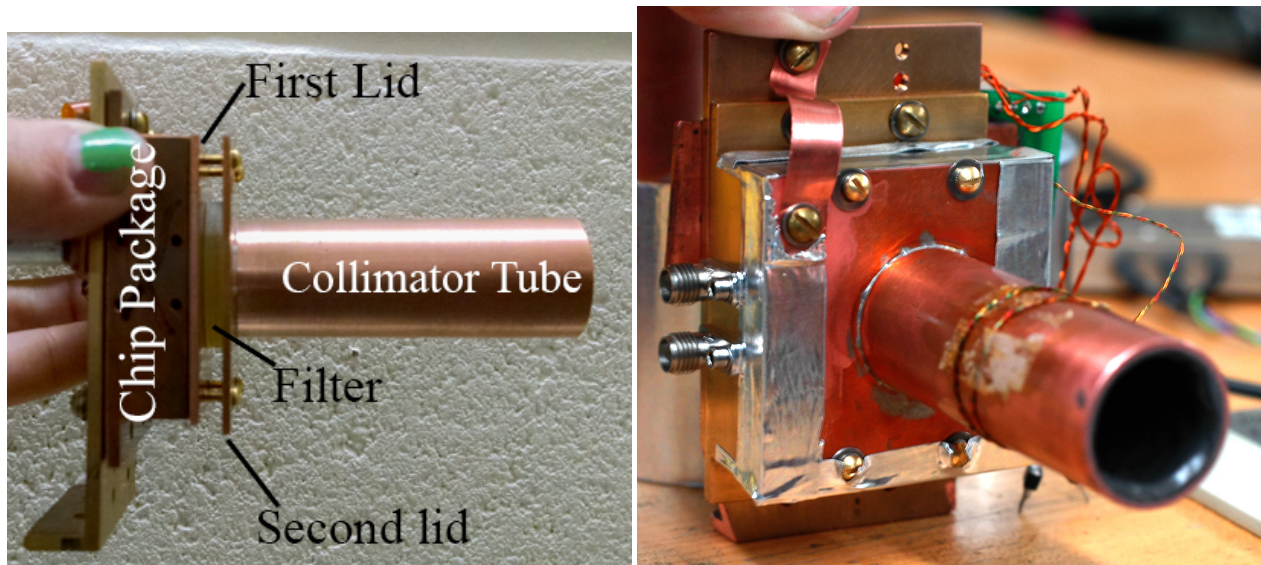
Figure 6.6: **Left:** Side view of collimator/filter assembly before addition of tape, thermometry, and heat strap. **Right:** Fully-assembled chip package assembly with collimator, thermometry (coiled around tube), filter (not visible), first lid (not visible), aluminum tape to provide an extra seal against light leaks, and heat strap (upper left) to ensure good thermal contact between the collimator tube and the cold bath.

about -25 dBc.

At the chip, the microwave power should be similar to the expected CMB power were the detectors looking at the sky; about 1.5 pW or -85 dBm for ground-based observing. At the output of the doubler, the power is about 1 dBm, so significant attenuation must be achieved between the doubler output and the chip. Some attenuation comes from the coaxial cable starting at the hermetic feedthrough and passing through the cryostat leading up to the horn antenna and some will come from the horn antenna itself, but there must be significant attenuation outside the dewar to reach the desired ∼ -85 dBm. The steelcast waveguide attenuator (see section 6.2.3.3) of broadband attenuation; 40 dB for the first mode and even greater attenuation for higher frequencies. An adjustable 0-50 dB vane attenuator is used to provide a small amount of adjustable attenuation, but not more than a few dB because vane attenuation does not attenuate odd harmonics. Recall, the doubler outputs the first harmonic at -25 dB, but since we're attenuating by ∼85 dB between the doubler and the chip, it's essential that most of the attenuation after the doubler is broadband and not limited to certain modes, or else higher modes will arrive at the chip at a higher power

than the first mode and confound sensitivity measurements.

The coaxial cable/hermetic feedthrough provides about 32 dBm of attenuation to the first mode and greater attenuation for higher frequencies (see section 6.2.3.2), the horn antenna provides about 10 dB of attenuation, the steelcast waveguide attenuator provides 40 dB of attenuation, and the vane attenuator is used to provide the last few dB to get down to -85 dBm.

6.2.3.2   100 GHz coaxial feedthroughs

To deliver W-band radiation from a room-temperature synthesizer into the cryostat and to the chip, we require a hermetic, low-profile (to fit in the narrow space between the 300 K and 77 K shields) feedthrough suitable for the 75-110 GHz frequency range. As far as we are aware, no such feedthrough was commercially available when we installed the coax. While a waveguide feedthrough is the usual solution for this frequency range, waveguide is simply too bulky and has too large a minimum bend radius to fit in the small available space. As a result, a custom, novel coaxial feedthrough was designed and fabricated.

The original 100 GHz coaxial feedthrough was installed in the same brass cap as the RF lines and followed the same route through the cryostat to the LHe stage (the 100 GHz line was installed first, and the RF lines were added some months later). It was made of coax with a 1.19mm OD beryllium copper outer conductor, silver-plated beryllium copper inner conductor, and PTFE dielectric. Both ends were connectorized with Anristu male W1 connectors, which were chosen for their suitability for this frequency range and their compatibility with the coax-waveguide transitions already owned by the lab. On the room temperature end of the cable, the back of the connector is butted up against the surface of a brass cap which will serve as the hermetic part of the feedthrough. The connector sits on the exterior side of the cap and the coaxial cable passes through a small hole in the cap (diameter roughly double that of the coaxial cable) and into the cryostat. This hole is sealed with degassed Stycast 2850 epoxy, which is applied so that it comes up around the base of the connector (using caution not to get epoxy on the mating surfaces of the connector) and fills the hole through which the coax passes. The brass cap is positioned over a ~ 1" hole in the

vacuum shell of the cryostat and seats on a flat milled into the side of the shell centered on the hole. The inward-facing side of the cap features a circular groove to allow for sealing with an indium o-ring. The cap is held in place with twelve steel 4-40 socket cap machine crews. Several months after the 100 GHz line was originally installed, two additional holes were drilled in the brass cap to accommodate two more 1.19 mm OD coaxial cables to be used as RF input and output lines. These were similarly sealed with stycast epoxy. See section 6.3 for more details on the RF lines. Inside the Dewar, the coaxial cable winds in a constricting spiral pattern between the lids of each temperature shield, with heat sinking measures taken at each stage, until they reach the interior "cavity" of the LHe stage. Here, the second connector mates with a coax-waveguide transition installed on the LHe stage.

This design worked well for about three years, but eventually the PTFE delaminated from the conductors allowing an air leak through the interior of the coaxial cable. While this is a risk with any coaxial cable hermetic feedthrough that isn't inherently sealed off on at least one end by a termination or connector, we believe that the leak was hastened or exacerbated by the location of the original line; its path, winding through the lids of each temperature stage, necessitated significant flexing of the cable every time the dewar was opened or closed. When the original feedthrough started to leak, we set out to improve the design for the replacement feedthrough.

The basic idea of the second 100 GHz coaxial feedthrough was essentially the same as the original design; a 1.19 mm OD coaxial cable was epoxied into an indium o-ring-sealed brass cap and routed through the different temperature stage shields to reach a coax-waveguide transition on the LHe stage. However, several key changes were made for the new design. Since the output from the microwave waveguide doubler is necessarily at a significantly higher power than what we want at the chip, we decided to use the coaxial cable itself as a significant part of the attenuation. This has a few advantages. First, the coax offers broadband attenuation, with stronger attenuation at higher frequencies, which is desirable to ensure that any higher harmonic output from the doubler is adequately attenuated before reaching the chip. Since we're specifically trying to maximize attenuation in order to get the signal down to -85 dBm, we selected lossier materials for the new cable: cupronickel inner and outer conductors with the same PTFE dielectric as before. When the
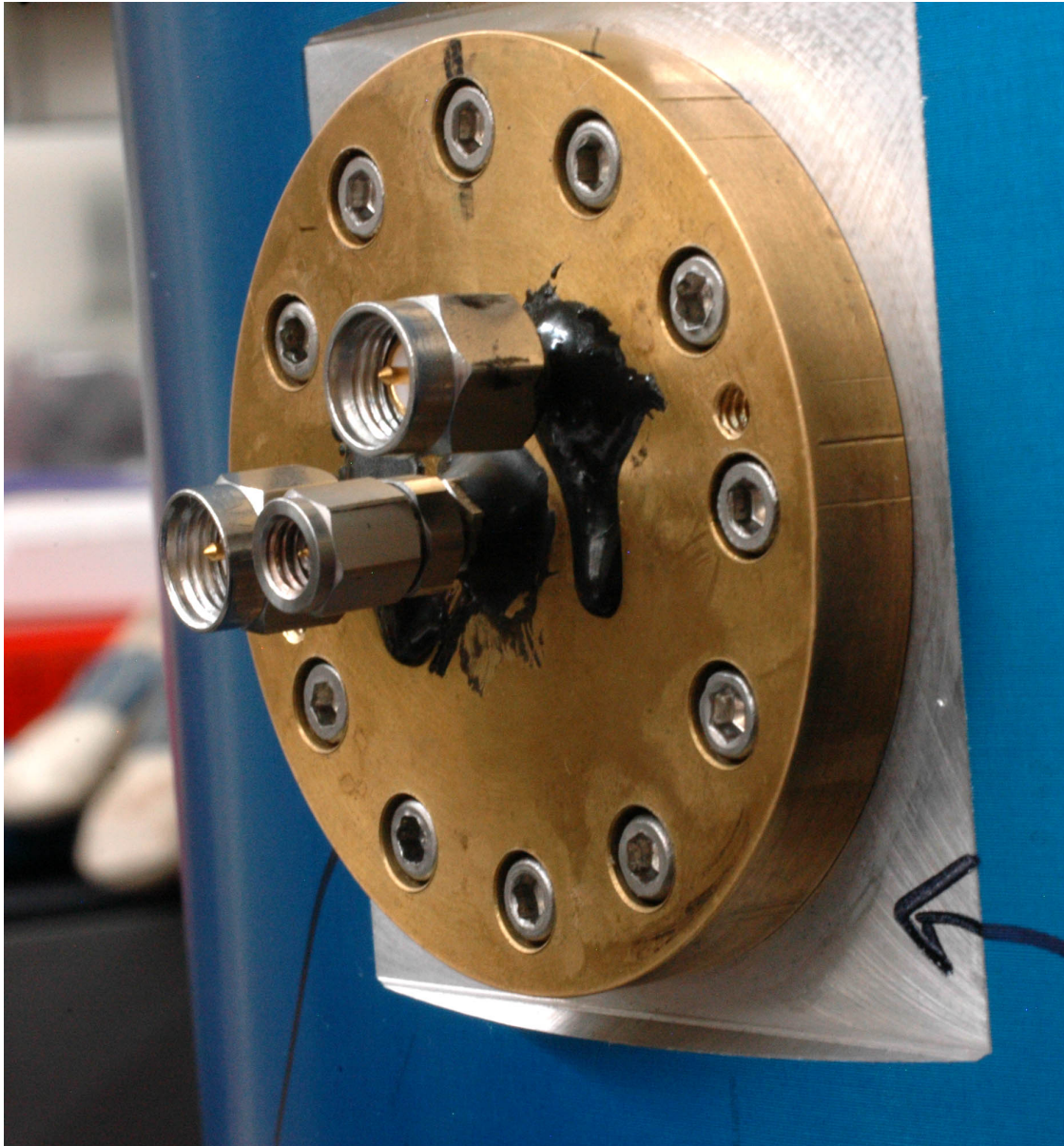
Figure 6.7: The mm-wave and RF coaxial connectors on the dewar shell for the original 100 GHz hermetic coaxial feedthrough are shown here. The center connector is for the 100 GHz line and the two outside connectors are for the RF lines (see section 6.3). After the new 100 GHz feedthrough was fabricated, this one was sealed over with stycast epoxy. The RF connectors are still in use.

original 100 GHz cable was designed, it was intended for testing of a TES array which required significantly more incident power for optimal operation, so the original 100 GHz line had been optimized for minimal length and minimal loss. The increased attenuation from the new coax is also increased *cold* attenuation, with heat sinks at each temperature stage, which reduces the risk of any thermal radiation from room temperature making it down the cable to the chip. The new design has a longer total length than the original cable, allowing for a greater thermal length between each heat sinking point, and therefore less heat load on the 4 K stage. Finally, the new cable is installed in a new location, with the brass cap on the side of the cryostat, near the bottom (when the cryostat is in loading position). Instead of routing the cable between the lids, which must be removed and replaced every time the Dewar is opened, the new cable is routed up the side of the cryostat, in an area where it won't need to be uninstalled or disturbed for possibly as long as several years at a time. If frequent flexing of the original cable contributed to the PTFE delamination and subsequent leaking, the new location will significantly slow that failure mode. This new cabling route also allowed for a cable of nearly twice the length, again allowing for more overall attenuation and more cold attenuation, with nearly 1 foot of the new cable routed along (and heat sunk to) the outside of the LHe tank.

According to the manufacturer specifications[5], the cupronickel cable has thermal conductivity at 4 K of $\kappa = 1.74 \times 10^{-5}$ Wcm/K, and attenuation at 4 K of approximately $A = 4.1\sqrt{f}$ with A in dB/m and f in GHz. Compare to the manufacturer specifications for the original beryllium copper cable: $\kappa = 1.77 \times 10^{-4}$ Wcm/K, and $A = 0.5\sqrt{f}$. The 300 K attenuation per meter of the cupronickel cable is about $A = 5.4\sqrt{f}$, or about 30% greater than the 4 K attenuation.

The new coaxial feedthrough is 68 cm in length. If we make the approximation that the average attenuation over the length of the cable will be about halfway between the 4 K and 300 K attenuation, then we find that the total attenuation for the whole cable at 100 GHz will be roughly 32 dB.

---

[5]http://www.coax.co.jp/en/cryogenic

6.2.3.3   Broadband waveguide attenuator

To adequately attenuate the microwave signal before introducing it into the cryostat, a ~ 40 dB broadband attenuator was required. While our adjustable vane attenuator goes up to 50 dB of attenuation, it only attenuates odd modes (i.e. the dominant TE_10 waveguide mode in the W-band, but not the harmonics that we expect to be generated by the mm-wave multipliers), which is insufficient for this application. Since there was no other microwave attenuator available in our lab, we made one using a recipe provided by Dr. Edward Wollack of NASA Goddard Space Flight Center. The broadband attenuator uses WR10 waveguide filled with steel-loaded Stycast epoxy (so-called 'steelcast'). Stycast was chosen because it has a similar coefficient of thermal expansion to copper; though we plan to use this attenuator at room temperature in the short-term, it could be used at cryogenic temperatures without suffering mechanical failure due to thermal expansion coefficient mismatch. Stainless steel powder is used to introduce magnetic loss which varies only slightly with temperature [9]. Our attenuator uses 36% by mass of epoxy resin, 2.7% of epoxy catalyst, and 61% of stainless steel powder. This is equivalent to 30% stainless steel by volume. The waveguide section is 0.25" long, which was aimed at attenuation of about 40 dB in the center of the W-band. However the measured attenuation is somewhat higher (see figure 6.8).

6.2.3.4   Horn and lens coupling

Finally, the last element in the optical chain for the swept microwave source is the horn antenna and rexolite lens. A coax-waveguide transition connects the mm-wave coax to the waveguide horn antenna on the liquid helium stage. The lens is held out over the ADR stage (but not in contact with it) by a OFHC copper 'diving board' which is thermally sunk to the helium stage (see figure 6.10). The optics were designed by Emily Barrentine based on quasi-optical beam theory [101]. We use a pyramidal horn antenna with a gain of 15 dB, and has a beam waist radius of 2.0 mm located 1.65 mm behind the aperture plane of the horn [101, 102]. Figure 6.11 shows the simulated and measured beam pattern for the horn.
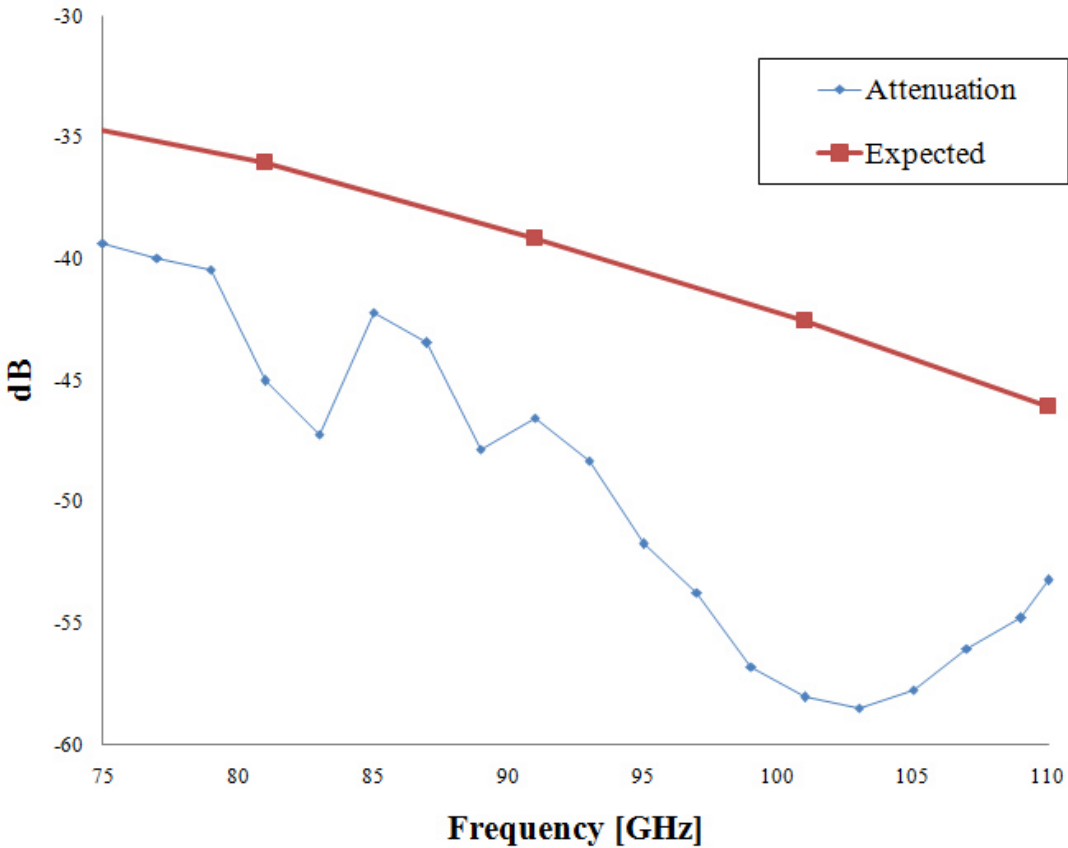
Figure 6.8: $| S_{21} |$ of the steelcast broadband waveguide attenuator across the W band. The red points indicate the predicted attenuation based on [9] and the blue line indicates the measured attenuation.

6.3   RF

6.3.1   Hermetic RF and microwave feedthrough

Very tight space between the thermal shields in the Blue Dewar necessitated a novel approach to hermetic RF feedthrough design. We required an air-tight RF coaxial feedthrough of minimal length in the direction of the dewar radius on the interior side, with an adequate amount of effective thermal length between heat sinking points at each temperature stage (ambient temperature, liquid nitrogen, and liquid helium), and with a geometry that permits the Dewar to be opened and closed frequently without excessive damage to the RF lines. Our solution was to install a new feedthrough
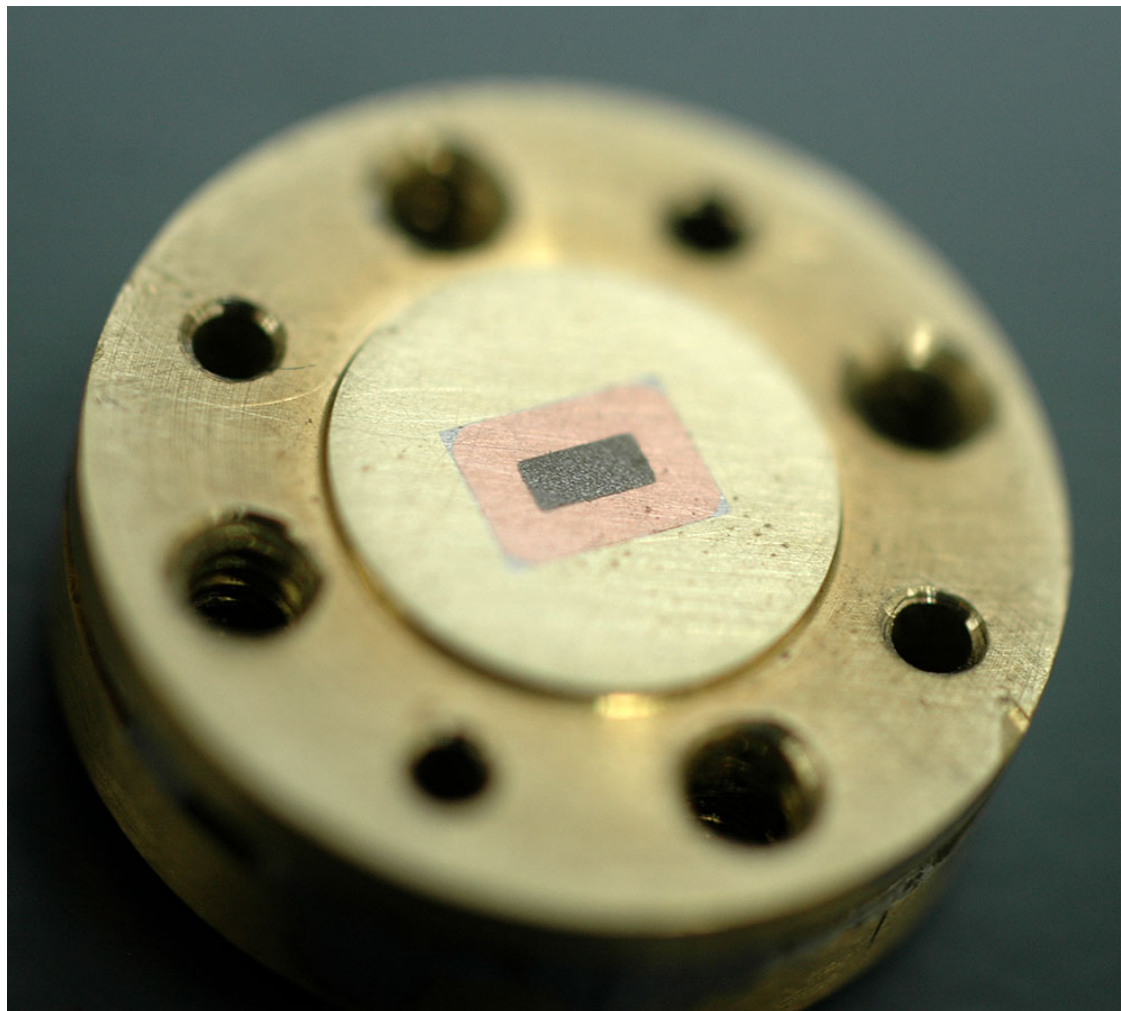
Figure 6.9: The steelcast WR-10 broadband waveguide attenuator.

port (mentioned in section 6.1). Similarly to the fabrication of the microwave line, a standard male SMA connector is installed onto one end of the coax according to the connector manufacturer instructions. Then the coax, 1.19 OD 50 Ω beryllium copper coax from Coax Co Ltd, with one connectorized end, is inserted into one of the holes in the brass cap, so that the connectorized end is on the exterior side of the cap and the back of the connector is butted up against the brass surface. Stycast 2850 epoxy is prepared according to the manufacturer instructions and degassed for a few minutes in a vacuum chamber. The brass cap and coax are clamped in place so that the plane of the brass is parallel to the floor and the un-connectorized end of the coax points down. Prepared epoxy is applied to the hole at the base of the connector, allowing epoxy to make contact and seal
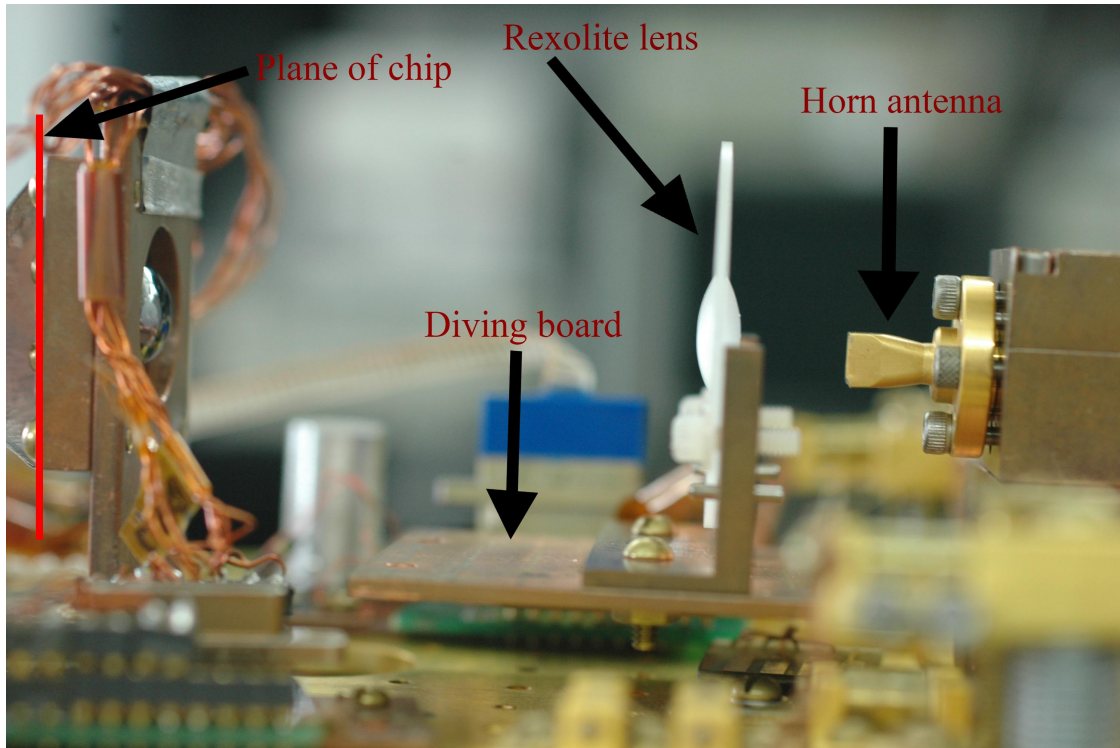
Figure 6.10: Shown here are the horn antenna and rexolite lens optics setup. The horn, lens, and diving board are all on the liquid helium temperature stage. The chip is on the ADR temperature stage.

around the back side of the connector (but with care not to get epoxy on the mating surfaces of the connector) and also allowing the epoxy to fill the hole and drip down through it onto the first centimeter or so of the coax on the other side. the epoxy is allowed to set overnight and then the cap can be installed in its place on the side of the Dewar, with an indium o-ring to create the seal. The Dewar is then pumped out and the new feedthrough can be leak checked. If a leak is found in the feedthrough, a new batch of epoxy can be prepared and applied over top of the existing epoxy layer on the outside of the feedthrough while the vessel is still under vacuum. The vacuum will help pull the epoxy into any leaking spots and seal them. The new layer of epoxy is allowed to cure overnight and the leak checking process is repeated. The second connector can be installed on the other end of the coax either before or after the coax gluing and leak checking process.

We found this type of feedthrough to be very effective initially, but unfortunately after repeated thermal cycling and repeated installation and uninstallation (which in our setup requires significant
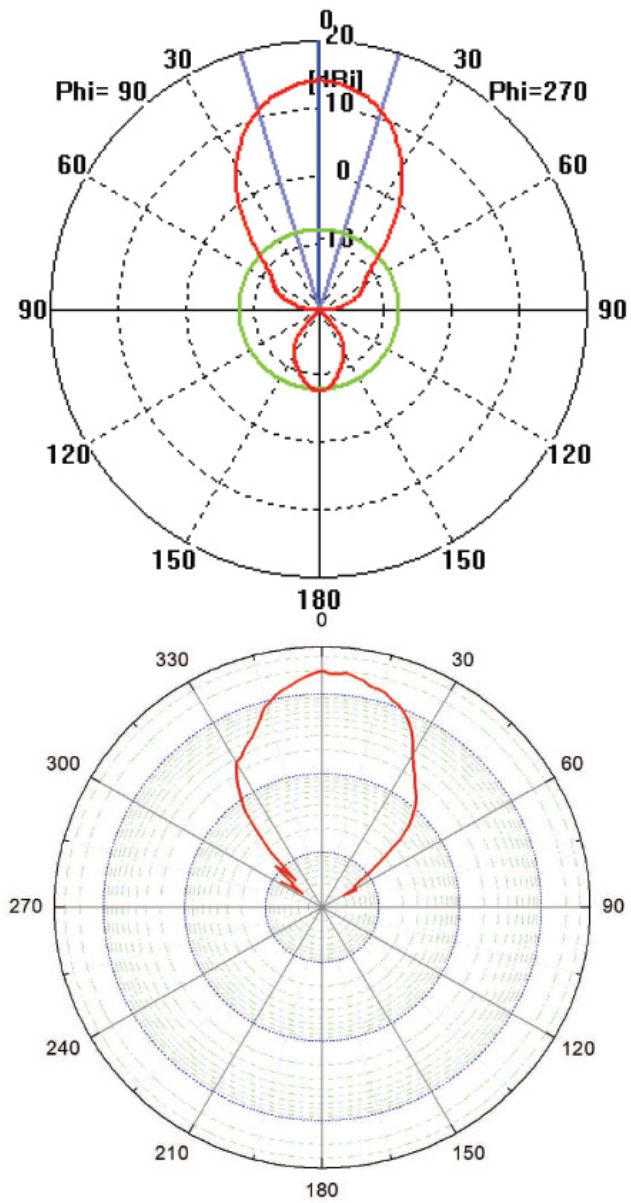
Figure 6.11: Simulated (top) and measured (bottom) beam pattern for the horn antenna. Simulations, measurements, and figures by Sara Stanchfield.

flexion of the coax) it did eventually begin to leak. While any cracks that may develop in the epoxy seal can be easily fixed using the leak checking and re-epoxying procedure described in the previous paragraph, we found that this is not the only hermeticity failure mode. We believe thermal cycling and frequent flexing of the cables eventually causes the PTFE dielectric to delaminate from the conductor on the inside of the coax, allowing for a small leak through the interior of the coax. In the case of the RF lines, we were able to seal off the leaks by tightly screwing male-male adapters into the SMA connectors at the exterior ends of the RF lines. While this solution continues to work more than a year later without further intervention, we do not consider it a reliable solution, per se. The leak in the microwave line was not repairable in this manner. For this and other reasons discussed in section 6.2, a second version of the microwave line was built. The original was clipped off at the brass cap and the remaining nub of coax was sealed over with degassed Stycast 2850FT epoxy, allowing for continued use of the RF lines, while eliminating the leak from the original 100 GHz line.

6.3.2   Cold RF components
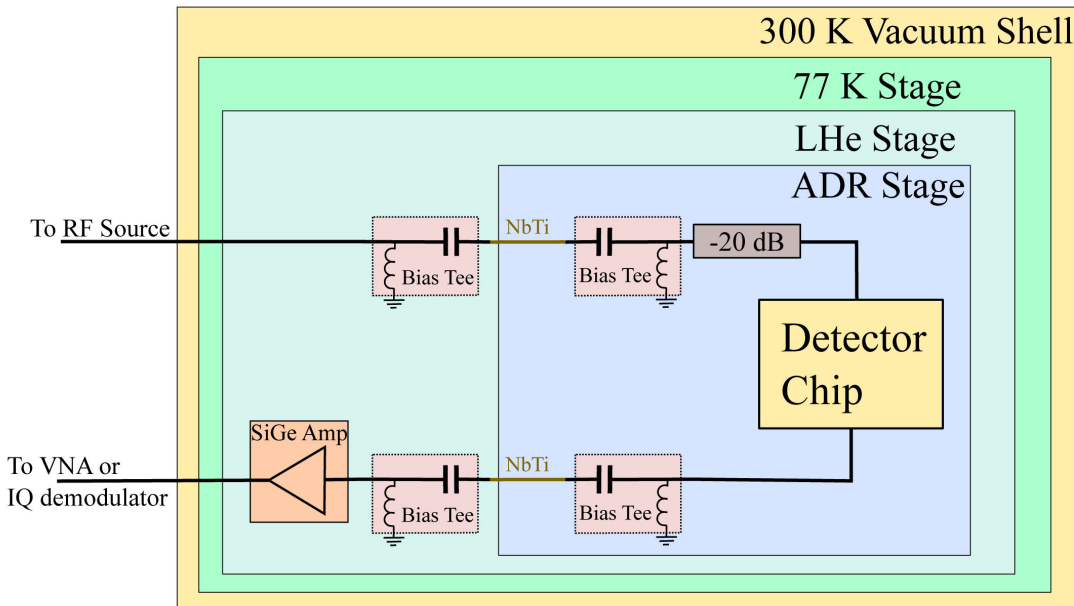
Figure 6.12: Schematic of cold RF components. Individual components are discussed in greater detail in the subsections that follow.

6.3.2.1   NbTi cables

Special consideration is required for getting the RF signal onto and off of the cold stage while avoiding both excessive thermal loading of the cold stage and excessive loss of the RF signal. The signal is carried between the liquid helium stage and the ADR stage by two custom 20 cm NbTi coaxial cables from Coax Co Ltd[6] (one on the input side and one on the output side).

Superconductors are especially well-suited to situations in which high electric conductance and low thermal conductance are required. In a superconductor, many of the electrons form Cooper pairs, which all sit in a zero-entropy ground state and are separated from all excited states by a gap energy. The Cooper pairs cannot leave the ground state and cannot carry any entropy without first being separated into quasiparticles and overcoming the gap energy. As a result, only unpaired electrons

---

[6]part number SC-086/50-NbTi-NbTi

are available for heat transport, significantly reducing the superconductor's thermal conductivity. At temperatures very much lower than the superconducting transition temperature, there are so few unpaired electrons that the conductivity can rival that of traditional insulators. At the same time, because the Cooper-paired electrons in the ground state are separated by an energy gap from all of the excited states, they cannot be excited or scattered by an arbitrarily small amount of energy because there are no states available to scatter into until enough extra energy has been put into the pair so that both electrons can overcome the gap. That means Cooper-paired electrons simply cannot interact with the impurities and lattice defects that would result in electrical resistance in a normal metal. Rather, the paired electrons move ballistically though the metal, with no resistance and no loss in the bulk metal (though there can be AC surface resistance effects, this usually has negligible effect except in the case of thin films).

NbTi has a superconducting transition temperature of 9.2 K. Therefore, below 4 K, there are few remaining unpaired electrons, and the conductivity of the NbTi is quite low. According to the manufacturer specifications, the NbTi cable assembly (including the Teflon dielectric) has a conductivity of 7.5×10^{-6} W cm/K at 4 K. As a point of reference, that is within a factor of a few of the conductivity of insulators such as Teflon [103] and tensioned Kevlar [104] at the same temperature; high purity copper at 4 K has a conductivity of about 7000 W cm/mK [99]. If we assume the worst-case scenario, where the conductivity of the cable remains at the 4 K value all the way through from the hot end to the cold end (even though both Teflon [103] and NbTi [105] decrease in conductivity monotonically and by roughly an order of magnitude between 4 K and 100 mK), for a 20 cm cable with a 4 K change in temperature, the heat flow for each cable is about 1.5 μW, which is well within the heat load budget for the ADR (the original flight with this ADR in the 1990s had an approximate quiescent heat load of 100 μW [98]).

6.3.2.2   Bias tees

In order for any of the above heat load calculations for the NbTi cables to matter, we must be sure that the cables are well heat-sunk on both ends. We need the inner and outer conductors to make

reasonably good thermal contact with the cold bath without disturbing the RF signal. For the outer conductor, this is trivial; simply ground the outer conductor to the LHe stage and the ADR stage. For the inner conductor, bias tees were used to achieve thermal contact to the cold bath. In a basic bias tee, the center conductor connects from the AC input to the AC output through a capacitor (essentially a minimalist high-pass filter). After the capacitor, there is an inductor that connects the center conductor to a DC input pin (essentially a minimalist low-pass filter). By grounding (and thermally sinking) the DC input pin to the cold plate (and cold bath), we can make a thermal connection from the center conductor to the cold bath, while the inductor prevents any influence on the AC signal. We are effectively applying a 0 V (grounded) DC bias, and in doing so causing the happy side effect of putting the center conductor in thermal contact with the cold bath. Bias tees were placed on the LHe stage side and the ADR stage side of both NbTi coaxial cables. The inductor side of the bias tee always faces away from the NbTi cable, to ensure optimal heat sinking.

Because of space limitations on the LHe and ADR stages, very compact bias tees were required. As far as we are aware, no manufacturer makes modestly-priced, compact, cryogenic bias tees with good performance in the 100-1000 MHz range. Therefore, we purchased 'room temperature' bias tees and verified their cryogenic performance ourselves. MiniCircuits ZX85-12G-S+ bias tees had good performance within their manufacturer-specified temperature range, but had a significant resonance in the middle of our frequency band at cryogenic temperatures. Marki Microwave BT-0018-0 bias tees fared much better (see Fig. 6.13) at very low temperatures, and so were selected for use in the coaxial cable heat sinking scheme.

6.3.2.3 Cold Attenuator

A 20 dB attenuator in a coaxial package with SMA connectors sits on the ADR stage between the bias tee and the chip package to help eliminate any reflections, or any 4K (or hotter) radiation that might be shining down the coax despite the bias tee.
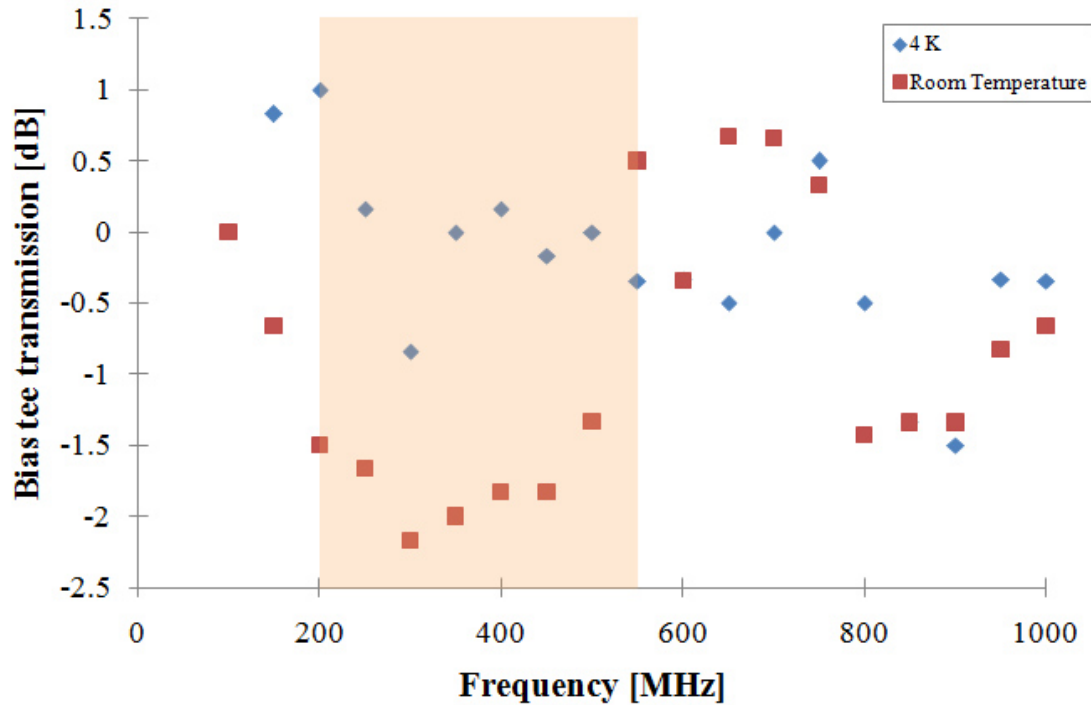
Figure 6.13: Marki microwave bias tee ($|S_{21}|$) at room temperature and 4 K. Highlighted area roughly indicates the band where we expect the detector resonances to be. Measurement error is about ± 1 dB, which is why some points show slight amplification instead of loss.

6.3.2.4 SiGe Amplifier

A silicon-germanium cryogenic amplifier fabricated by and purchased from the laboratory of Dr. Sander Weinreb at the California Institute of Technology (model CITLF1) sits on the LHe stage after the second bias tee on the output side of the chip. It provides cold, low-noise amplification of the detector signal. The noise temperature at 20 K is 7 ± 1 K at 1 GHz. See figure 6.14 for the room temperature gain over a range of frequencies of interest.

6.3.3 Network Analyzer

Most of the measurements presented in this work were made using a vector network analyzer (VNA) generously lent by the Van der Weide laboratory in the UW division of engineering. For most measurements, port 1 of the VNA was used as the RF source (connected to the input SMA
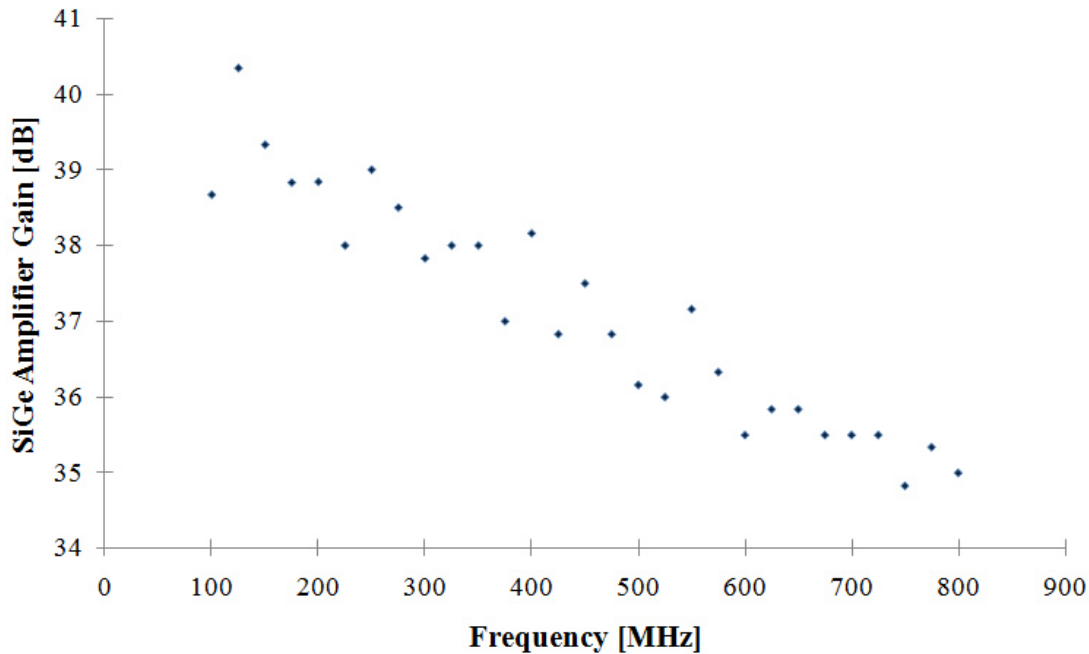
Figure 6.14: SiGe amplifier performance at room temperature.

on the RF hermetic feedthrough described in section 6.3.1) and port 2 as a detector (connected to the output SMA on the RF hermetic feedthrough). Collection of complex response data was implemented with Labview data acquisition software adapted by then-undergraduate Catherine Steffel and operated via a GPIB interface between the VNA and a PC.

Additionally, some of the earlier measurements were taken using a scalar network analyzer (SNA) in conjunction with an external swept RF source. Labview software, again operated via GPIB connection to the SNA and adapted by Catherine Steffel, was used for data recording.

Subsequently, MATLAB scripts were used to peak-fit and analyze the response data offline.

6.3.4   IQ demodulator

Because the network analyzer is not capable of very high data capture rates, an alternative measurement scheme is required to measure noise in the resonances. For this purpose we purchased a custom Polyphase Microwave I Q demodulator based closely on model AD0105B, with the frequency

range adjusted from 100-500 MHz to 200-700 MHz. A digital oscilloscope or a MCCdaq USB analog-to-digital converter (ADC) connected to a laptop were used to record the IQ demodulator data, depending on the demands of the particular measurement. A schematic of the IQ demodulator setup can be found in appendix D.

6.4   Other Room Temperature Electronics

Measuring sheet resistances and critical temperatures from the diagnostic chip DC 4-wire structures necessitates a method of highly accurate resistance measurement. For this we typically employ two pieces of equipment. A Keithley high-precision multimeter in "4-wire mode" can be used as an extremely straightforward monitor of resistance at liquid helium bath temperatures and higher. However the Keithley's simplicity is also its downfall at lower temperatures. Because it does not offer user control of the excitation current, at lower temperatures the resultant heating of the cold stage is too great. Additionally, the Keithley does not allow for user control of the load resistance, so the it does not give accurate measurements when the lead resistance is much greater than the sample resistance.

As a verification of the Keithley at high temperatures and low lead resistances, and as a sole means of measurement in cases where the Keithley is not useful (either due to thermal loading or insufficient load resistance), a lock-in amplifier is used to make 4-wire resistance measurements. Low excitation frequencies (10-100 Hz, typically) are chosen to minimize AC effects on the resistance measurement.

CHAPTER 7

MEASUREMENTS

This chapter will describe the various measurement efforts conducted in the course of this dissertation project.

7.1 Molybdenum resonators

Because of its convenient natural T_c and because of the challenges associated with controlling the T_c of TiN_x, the first set of resonators were made with molybdenum. While the material ultimately proved too lossy for use in this type of detector, it was an instructive material for blazing the trail that led to our final test setup.

7.1.1 Mo v1

Very little work has been done previously to investigate Mo as a candidate material for high-Q superconducting resonators. It was investigated by Leduc and others at Caltech/JPL in the very early days of KIDs, but that work was never published, and as far as I am aware there has been no other prior work on the subject. While Mo is known to have a desirable T_c and was suspected to have a desirable density of states and characteristic quasiparticle recombination time constant, its practical ability to resonate was unknown. Therefore, it was necessary to start with a test of the material alone before attempting to use it in an actual detector.

Collaborators at GSFC made available an mSQUID mask (discussed also in chapter 5). The mSQUID mask, originally designed as a prototype of a microwave microresonator multiplexing readout for SQUIDs, is now used primarily to pattern candidate superconducting microresonator materials for evaluation of their RF properties. The pattern is a single-layer CPW design with a

central transmission line flanked on both sides by 16 CPW planar LC resonators. Each of the 16 resonators is tuned to a different resonant frequency and each is coupled to the central transmission line with a different coupling strength. As resonant frequency increases, so increases the coupling Q, over a range from Q_c=5.3k to Q_c=100M.

The mSQUID mask was used to pattern a Mo film deposited in a CVC sputtering system with the help of Peter Nagler using a recipe which I will henceforth refer to as 'Mo v1', described in appendix A. The film was etched using the E6 wet etch process also described in appendix A.

Finally, chips from this wafer were mounted in an SMA-connectorized package and installed in a cryostat known as Bacchus in the laboratory of Dr. Harvey Moseley, at GSFC. With the help of Dr. Emily Barrentine, I cooled the chip to a base temperature of 320 mK and measured the RF response using a VNA as both source and detector. We observed a single resonance (likely actually several resonances lumped together) with a Q of $\mathcal{O}(100)$. Since the base temperature was somewhat high relative to the critical temperature, this low value for Q is not terribly discouraging. At the relatively high base temperature of 320 mK, with our anticipated Mo film properties, the best-case Q would only be about 2500.

We proceeded with fabrication of a full 20-pixel prototype array using geometry B. These wafers were brought back to Madison for testing in the Blue Dewar. DC measurements of the diagnostic chips were made using the lock-in amplifier and RF measurements of the detector chips under dark conditions were made using the SNA. We measured the critical temperature to be 1.1 K, which is consistent with an expected T_c of 0.9 K for bulk Mo. We expect the T_c to be slightly higher than for bulk Mo; in very thin films the film thickness restricts the coherence length which shifts T_c upwards. Unfortunately, there were no visible resonances on any of the detector chips tested with Mo v1.

7.1.2 Mo v2

Following testing of resonators made with the first Mo recipe, I returned to Goddard and made a new set of wafers with a slightly altered recipe. The new recipe was deposited at a higher power
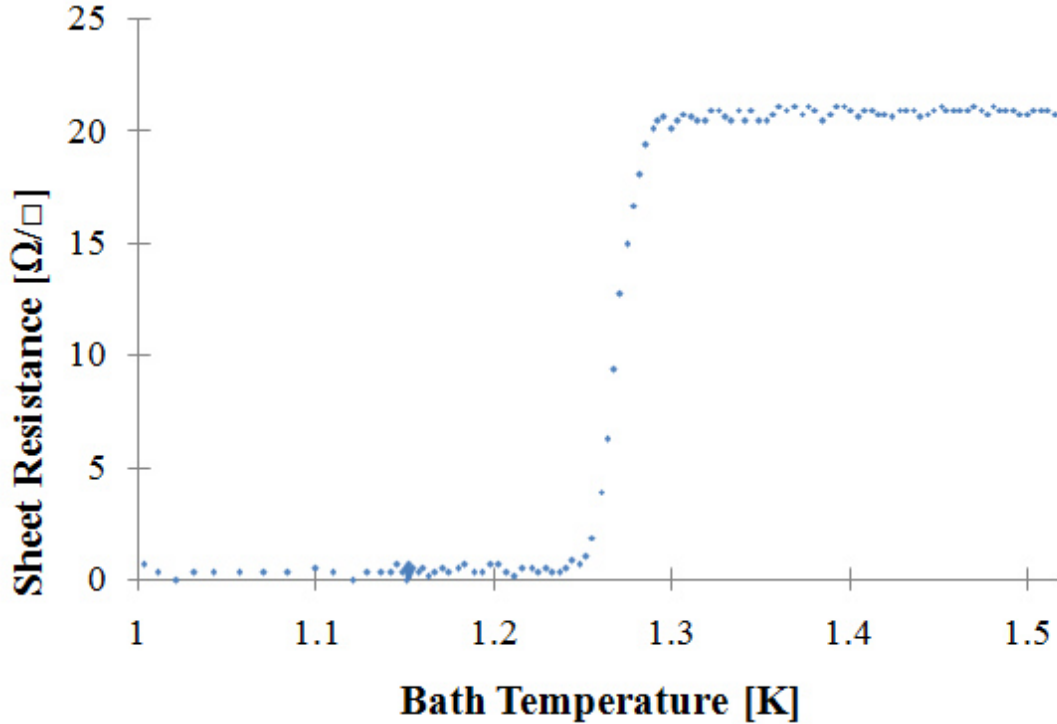
Figure 7.1: Measurement of the superconducting transition of Mo v2 on dummy wafer 2 chip 2. T_c is about 1.27 K and R_s is about 20 $\Omega/\square$.

and used plasma shapers to help assure a more even film. The higher deposition power increases the deposition rate, decreasing the deposition time and resulting in a cleaner film. The sheet resistance of the resulting films was about 20 $\Omega/\square$, and was consistent between the dummy wafers, product wafers, and with older samples of the same recipe which we previously tested for T_c and R_s in Madison. The films were quite tensile, with an average stress on the dummy wafers of about 945 MPa across six measurements at different angles, but this is consistent with historical results from this recipe.

Back in Madison, measurements of the diagnostic chips showed sheet resistances around 20 $\Omega/\square$ and a critical temperature of about 1.27 K (see figure 7.1). RF tests of detector chip exhibited the first well-separated resonances for this detector design. Unfortunately, the internal Qs saturated at about $Q_i \simeq 5000$ below 300 mK (see figure 7.2). This is indicative of some source of temperature-independent dissipation which dominates at low temperature. We investigate two possible causes of this dissipation in sections 7.1.3 and 7.1.4.
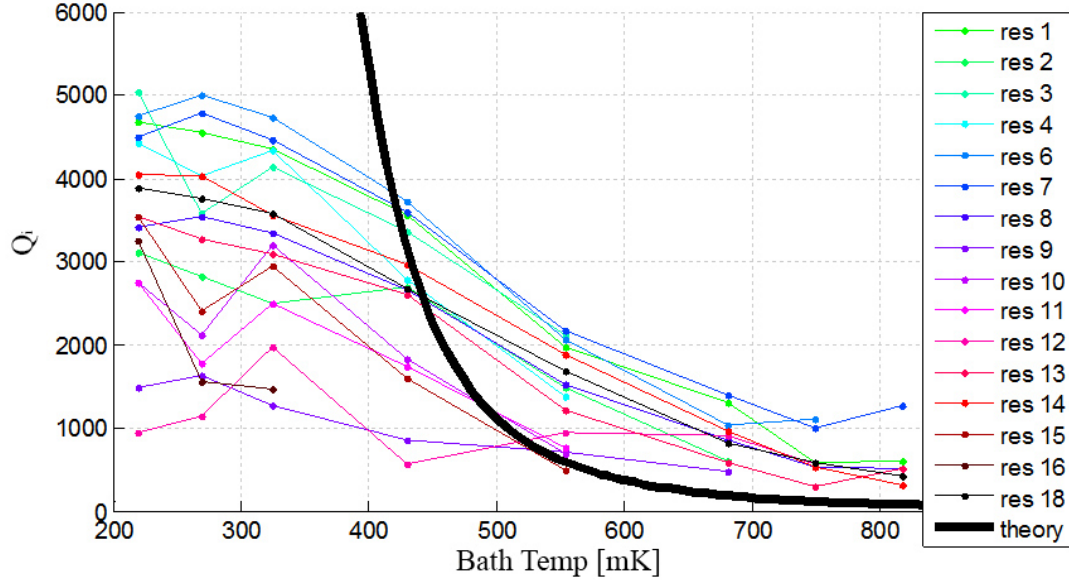
Figure 7.2: Measured internal quality factors of molybdenum resonators of geometry A over a range of temperatures. The thick black line shows theoretical best-case Q_is for a well-behaved Mattis-Bardeen material with $T_c = 1.27$ K, $\alpha=0.5$, and $R_s=20$ $\Omega/\Box$.

7.1.3   Magnetic field trapping

One possible source of Q degradation is magnetic field trapping. If there is a finite magnetic field component normal to the plane of the inductor at the moment when it passes through the superconducting transition, magnetic flux can be trapped by the superconducting material, which can decrease the gap parameter, decreasing Q [5]. In an effort to identify the cause of the degraded internal quality factors, Qs were measured with the cryostat in three different orientations relative to Earth's magnetic field: 180 mG component of B_{Earth} normal to the chip, 47 mG normal to the chip, and 0 mG normal to the chip. The chip was heated above the transition temperature of the Nb groundplane and re-oriented between measurements to ensure all trapped flux during the measurements was associated with the intended cryostat orientation. Error in cryostat orientation is approximately 5°, or about 16 mG.

Results are summarized in table 7.1, where a representative sample of measured Q_is for the first seven detectable resonances are shown at similar temperatures for the three orientations with respect to Earth's magnetic field. As expected, the highest Q_is were observed in the 0 mG normal

field orientation, with an average Q_i of 4300 for the seven resonators shown in detail in the table, or 3500 for all 18 resonators detectable at that temperature. The average Q_i in the maximum normal field component orientation was cut by more than half compared to 0 normal field. The intermediate orientation, at 47 mG, was degraded by about 10% compared to the 0 mG case. Figure 7.3 shows the first (lowest frequency) resonance in each of the three magnetic field scenarios.

Resonance number	180 mG normal B field, 201 mK	0 mG normal B field, 219 mK	47 mG normal B field, 204 mK
1	2100	4700	4900
2	2000	3100	3200
3	2700	5000	3900
4	2200	4400	4100
6	2100	4700	3700
7	2000	4500	3500
9	1500	3400	3700
average Q_i	*2100*	*4300*	*3800*
percent of max	*48%*	*100%*	*89%*

Table 7.1: Measured Qs for the first 7 detectable resonances. A 180 mG decrease in the normal component of B_{Earth} doubles the average measured Q_i.

We conclude that magnetic flux trapping can have a significant effect on observed internal resonator quality factors in KID devices, however cryostat orientation is not sufficient to relieve the tension between our measured and expected Qs. Magnetic field orientation is nonetheless an important consideration in KID testing and design. Following these measurements, the magnetic field in the lab was carefully mapped out and the cryostat was positioned so that the chip would have a normal component from Earth's magnetic field near zero for all subsequent measurements.

7.1.4   Molybdenum double-gap behavior

A number of superconducting materials are known to exhibit "double-gap" behavior [106–110]; magnesium diboride is especially well-represented in the literature. In a double-gap superconductor, some of the conduction electrons live in a low-gap state and some live in a high-gap state. Because
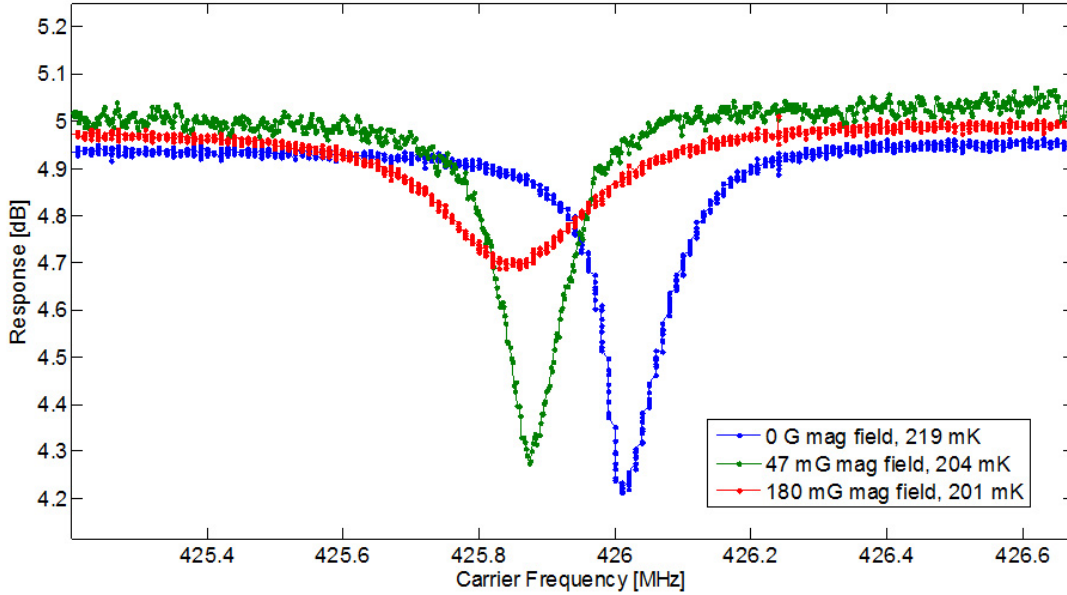
Figure 7.3: First resonance for the Mo v2 detector chip with three different normal magnetic field components. Plot shows the voltage transmission coefficient, $|S_{21}|$, of the readout line as a function of frequency.

electrons occupying these states are intermingled in physical space, they proximitize and a simple DC critical temperature measurement reveals a single T_c. However, one expects the internal quality factor in a double gap material to be degraded relative to the Q_i expected based on the DC critical temperature; electrons in the low-gap state see a much higher bath temperature to T_c ratio, which results in a larger than expected population of thermally excited quasiparticles. To detect a double gap in a superconducting material, one can measure the dependence on temperature of a superconducting resonator's resonant frequency. If the data is a good fit for one BCS gap at high temperatures and a good fit for a different BCS gap at low temperatures, this is evidence for a double gap or multi-gap material. This behavior is easiest to see and understand by looking at the dependence on $1/T$ of $\log(1 - (f(T)/f(0))^2)$, where $f(T)$ is the resonance center frequency at a given temperature, which should be linear with a slope $m = -\Delta/k$ in the low-temperature limit [96]. Figure 7.4 shows the 0 mG B_{Earth} data from the test diagnostic chip displayed in this manner. The dashed line shows the relatively poor best fit for a simple single-gap model. The best fit has $\Delta = 0.75 \times \Delta_{BCS}$. The solid line shows a substantially better fit to the data by allowing 25% of

the $1/L_k$ to come from a low-gap state with $\Delta = 0.33 \times \Delta_{BCS}$ (i.e. a superconducting energy gap which is only 33% of the gap energy expected from a simple BCS prediction) and the remainder of $1/L_k$ coming from a typical gap state with $\Delta = \Delta_{BCS}$. Figure 7.5 shows an alternative view of the same data set, now with inverse internal quality factor and inverse bath temperature for two resonators with the lowest and highest internal Qs. The solid line shows the expected Q_is for a simple two-gap best-fit model. However, figure 7.2 shows that at low temperature, Q_i saturates as a result of an unknown temperature-independent dissipation. The dashed lines show the two-gap prediction for Q_i with two different constant values added in to account for the unknown additional dissipation. When the additional constant dissipation term is included, the two-gap model is a good fit for the data. An alternative explanation for this data is the Klapwijk model for gap broadening in disordered superconductors [111]. Distinguishing the two-gap model from the gap-broadening model in our samples will require additional data, especially more precise measurements of center frequency response and Q$_i$ response to bath temperature at more bath temperatures over a wider range.

The low-gap population of electrons may be sufficient to relieve the tension between the expected and observed internal quality factors, however additional data will be required to definitively confirm or rule out this explanation.

7.2 Titanium nitride resonators

Titanium nitride is a promising material for superconducting detectors because the critical temperature is tunable either by carefully controlling the nitrogen flow during deposition or by using proximitized multilayers with titanium nitride and pure titanium. It also has properties that are desirable for kinetic inductance detectors in particular, including a long characteristic quasiparticle time constant and a low electron density of states at the Fermi level. A significant amount of the time spent on this project was devoted to developing a suitable TiN material and to testing candidate TiN materials.
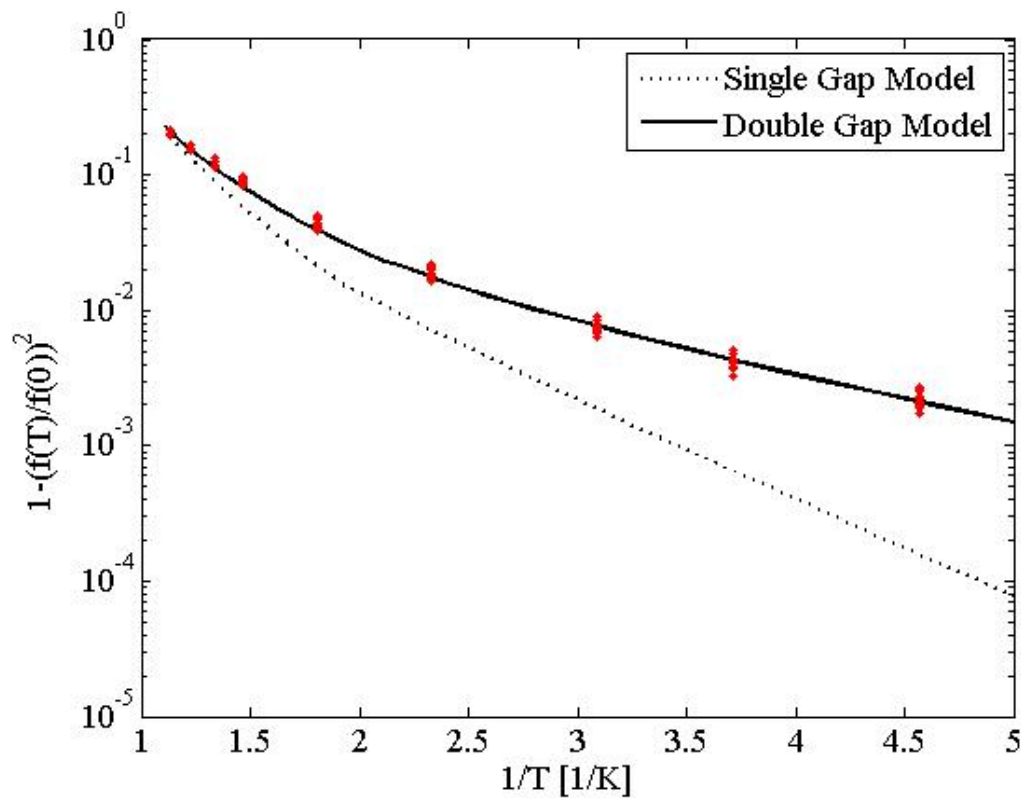
Figure 7.4: Shown here is resonant frequency vs temperature, f(T), for the Mo v2 resonators (red dots), plotted as described in section 7.1.4. The dashed line is a simple single-gap expectation from Mattis-Bardeen. The solid line is a fit allowing for two superconducting gap energies. In the units shown, we expect the data to be linear in the low-temperature limit (high 1/T limit), with a slope $m = -\Delta/k$.

7.2.1 Early TiN materials

There were a number of 'early' TiN recipes tested before we made any TiN resonators. This section will briefly summarize measurements of these materials and the reasons they were not used to make detectors.
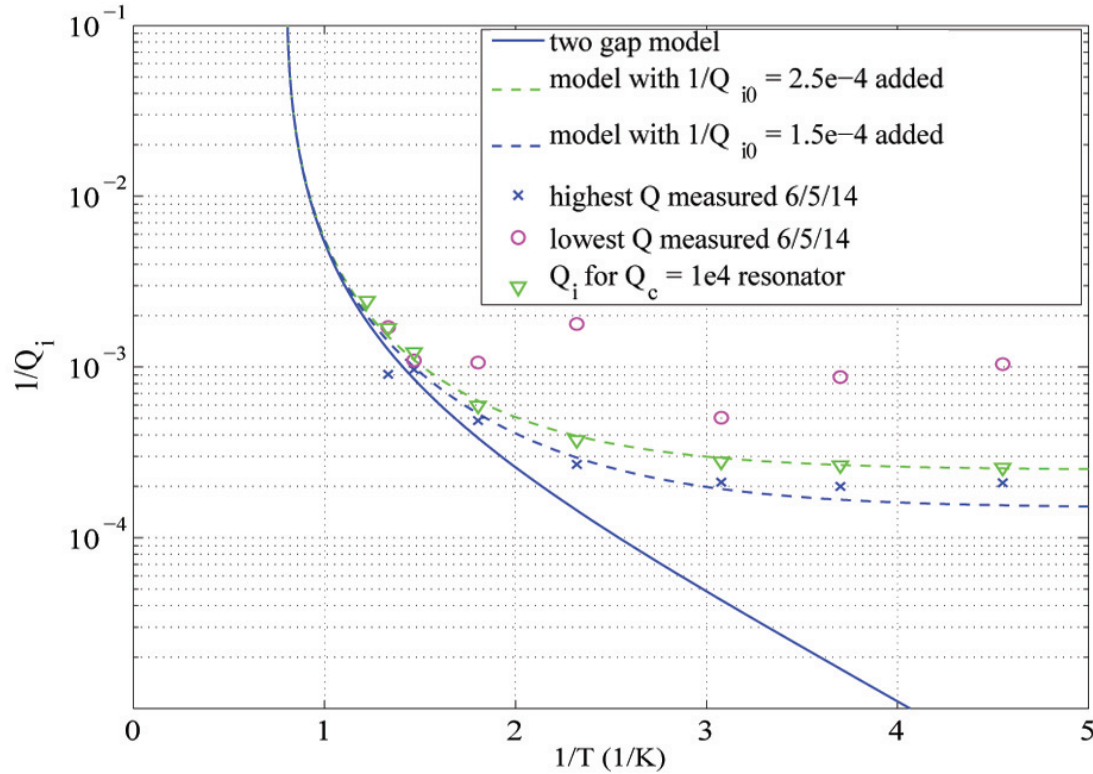
Figure 7.5: Two-gap fit to the data, with and without an additional temperature-independent dissipation term. The purple circles are the data from the resonator with the lowest internal Q. The blue x marks are the data from the resonator with the highest internal Q. The green triangles are the data from the resonator with the best-matched coupling Q, $Q_c = 1 \times 10^4$. The solid blue line is the expectation for a simple two-gap model. The dashed blue and green lines are expectations for two gap models with, respectively, 1.5×10^{-4} and 2.5×10^{-4} added to $1/Q_i$ to account for the observed temperature-independent dissipation. Figure generated by Dr. Thomas Stevenson of NASA Goddard Space Flight Center from data generated by me.

7.2.1.1   Monolithic TiN

The primary advantage of single-layer titanium nitride is the very fact that it is single-layered; this removes relative layer thicknesses from the parameter space and makes it correspondingly simpler to optimize the material. The critical temperature of TiN can be tuned by adjusting the nitrogen flow during deposition to produce substoichiometric TiN, however the critical temperature is extremely sensitive to nitrogen flow so that there is a very narrow range of nitrogen flows that produce materials with T_c lower than that of stoichiometric TiN but higher than that of pure Ti. I

tested samples of five nominally substoichiometric TiN samples produced by Dr. Ari Brown over the course of several months. Of the five samples, one had a T$_c$ essentially equal to that of pure Ti, two had T$_c$s very close to that of stoichiometric TiN and two had no superconducting transition above 200 mK, which was the minimum temperature of our ADR during those tests. Since we weren't able in practice to produce an intermediate critical temperature with the monolithic TiN, we moved on to trilayers.

7.2.2   Trilayer TiN

Trilayer TiN has the advantage that the critical temperature can be tuned without the precise nitrogen flow control needed to tune substoichiometric TiN. Using the paper by Vissers [43] on multilayer TiN as a starting point, Dr. Ari Brown developed TiN trilayer recipes with various critical temperatures and sheet resistances. While the films resulting from these recipes originally underwent DC testing for T_c and R_s at Goddard, following a change in chamber condition they needed to be re-characterized. I carried out this re-characterization in our Madison cryostat. While a process for producing films with a desirable T_c and R_s was identified relatively quickly, developing suitable etch process required several iterations of process development and testing. Results of these tests are discussed in section 5.2.2.

7.2.3   TiN trilayer detector chips

Once a suitable TiN trilayer deposition and etch combination was identified, we fabricated a set of wafers with geometry B and tested them in our laboratory cryostat. DC testing showed a critical temperature of 1.16 K and sheet resistance of 41.5 $\Omega/\square$, consistent with previous tests of samples using the same deposition and etch recipes.

Next, the resonators on the detector chip were tested under dark conditions with the package lid on, so that the detectors are looking at a wall with the same temperature as the bath temperature, seeing essentially no in-band optical power. Of 20 resonators on the chip, 19 were visible in
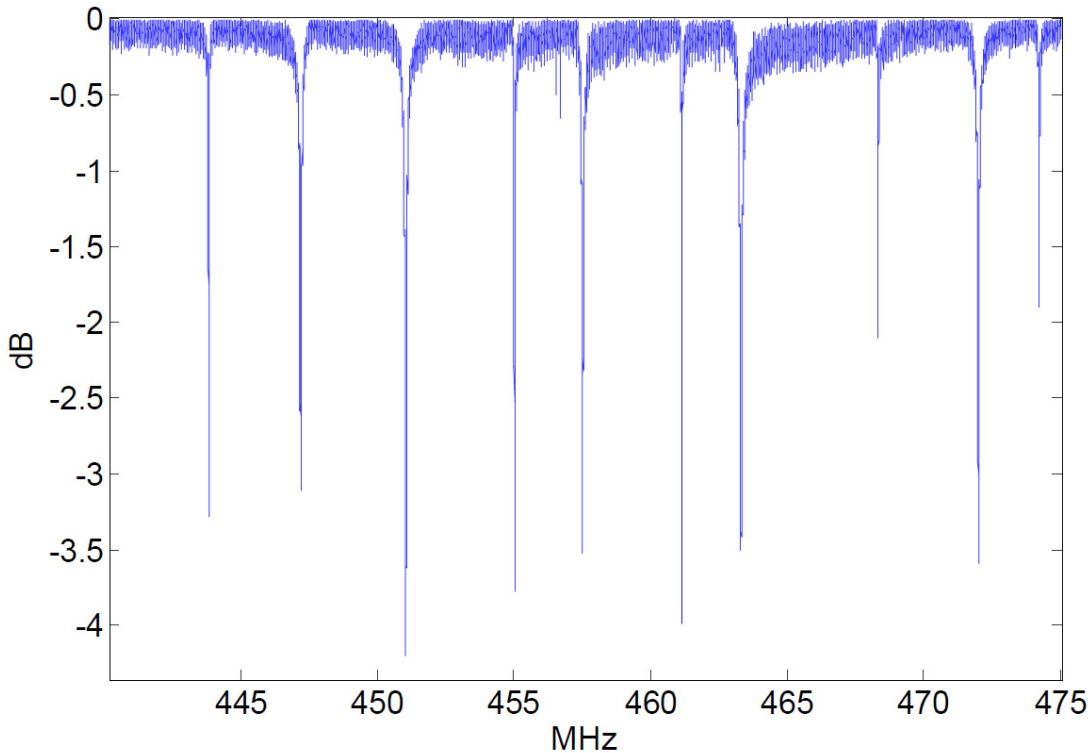
Figure 7.6: Resonances 10-19 from product wafer 12, chip C.

measurements. It is unclear why the missing resonator, with the eighth-lowest frequency, was not visible; there were no obvious lithographic flaws upon inspection under a microscope. Possible explanations for the missing resonator include: the resonator works but the resonance was lost in the noise (that resonator was designed to have a coupling Q of 100,000, which would make it among the hardest resonators to see), there is a lithographic flaw not visible on a microscope, or there is a localized variation in TiN film quality or localized wafer contamination affecting only that resonator. Figure 7.6 shows 10 of the 19 visible resonances.

Measurements of the response of the resonator center frequencies to changes in bath temperature are shown in figure 7.7. These data show that the gap energy for this TiN film is significantly below what we expect for a material with a T_c of 1.16 K and that TiN does not match well with either a single-gap or a double-gap model. That TiN is not a well-behaved Mattis-Bardeen material has been known for several years [111, 112]. Since both the single-gap and double-gap models are a poor fit to the data, this suggests that TiN may be a broadened gap material, perhaps obeying the
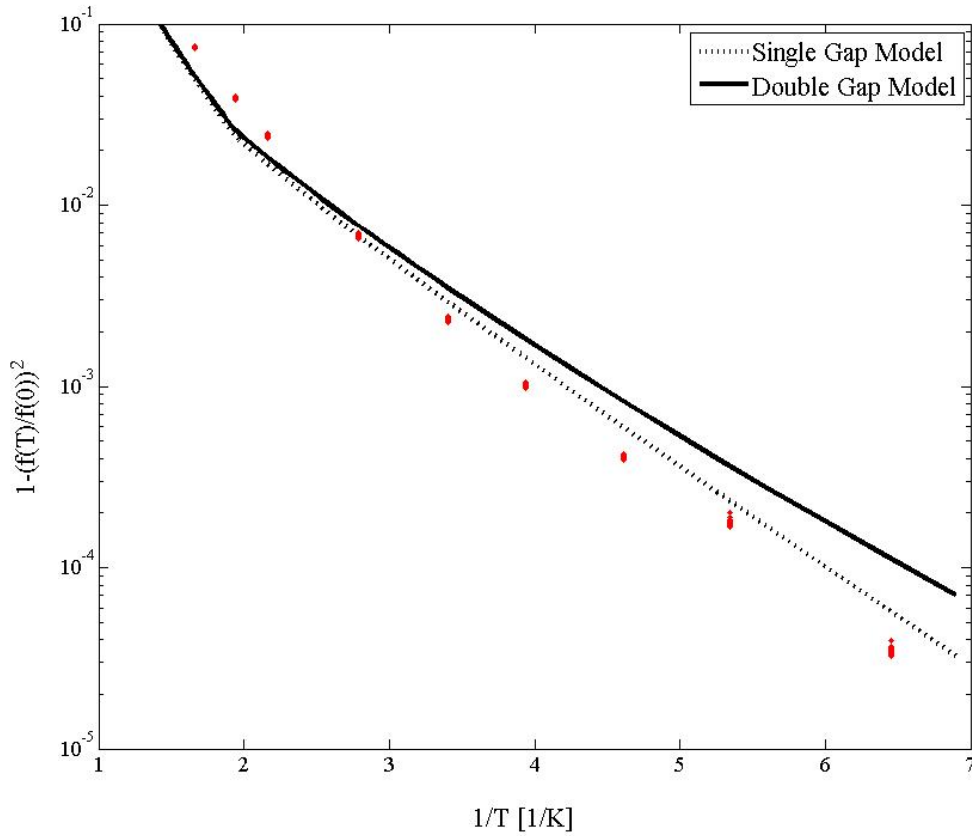
Figure 7.7: Dependence of the resonant frequency, f(T) on changes in bath temperature for TiN trilayer resonators on product wafer 12 chip C. Data are red dots. Single and double gap models are the dotted and solid lines respectively. Neither the single-gap nor the double-gap models are good fits for the data.

Klapwijk broadened gap model discussed in the Mo section [111]. Significantly more data would be required to more fully understand the superconducting gap behavior of TiN. The best fit gap(s) are about 90 μeV, which is only about half of the expected Mattis-Bardeen gap.

The internal quality factors for the TiN trilayer detectors perform much better than their Mo counterparts, though the Q_is do still start to saturate at low temperature. The highest internal Qs observed for the trilayer TiN chip was nearly 200,000. There was, however, a substantial spread. The highest internal Q was 194,000 and there were 10 TiN resonators with Qs over 100,000, but the lowest Q_i was just 26,000. The reason for this extreme variation is not well-understood. A plot of Q_i relative to the resonator's physical position on the chip shows a checkerboard pattern
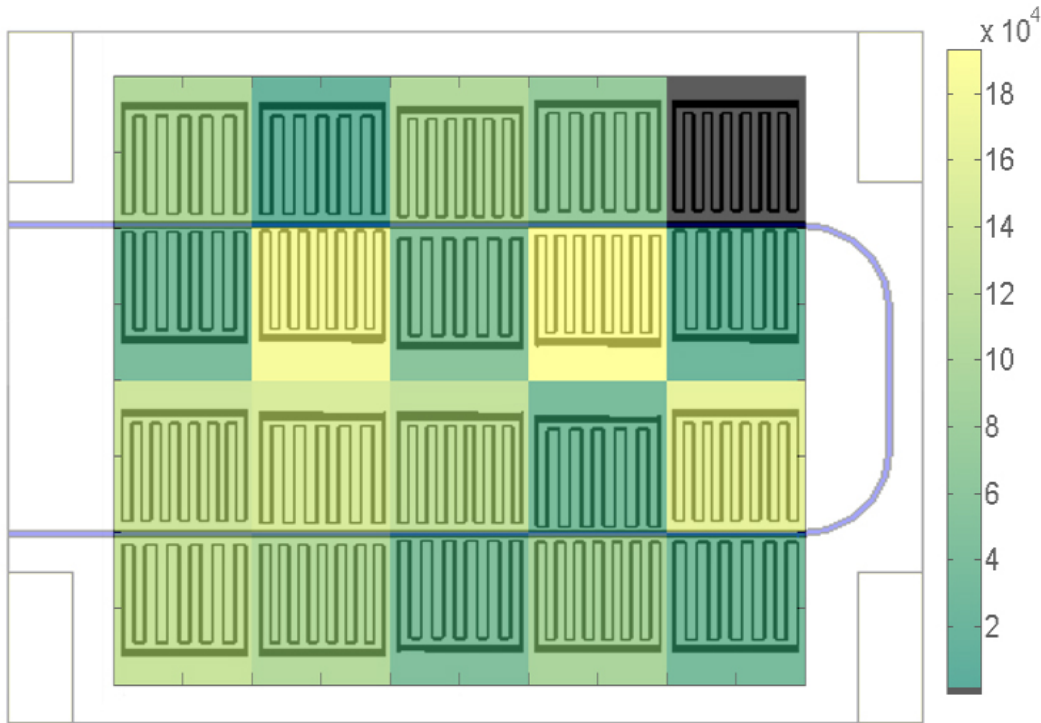
Figure 7.8: Values of Q_i at 155 mK overlaid on a drawing of the chip layout. The black pixel indicates the resonator that was not visible in any of the measurements. Notice the checkerboard pattern. The higher-Q pixels correspond to the higher frequency resonators.

(see figure 7.8). This pattern rules out some sort of contaminant gradient or film quality gradient across the wafer as the cause of the lower Qs in certain resonators. Yet the relationship between Q_i and resonator frequency in this data set is not monotonic (see figure 7.9). Rather, the data forms two clusters: one cluster made up of all the visible resonators with 12 inductor meanders (higher resonant frequencies) and one made up of all the visible resonators with 14 inductor meanders (lower resonant frequencies). This suggests that some aspect of the geometry of the 14 meander resonators is adversely affecting the resonator quality factor.

Following the fully-dark (lid-on) tests of the prototype array, the resonators were measured again with the package lid off. This configuration allows the detectors to see the walls of the liquid helium stage, which are at about 1.9 K. Since the helium stage temperature is near the CMB temperature, the detectors in this configuration see quite a few in-band photons (whereas with the lid on, there was essentially no in-band illumination). For tests done at the same bath temperature,
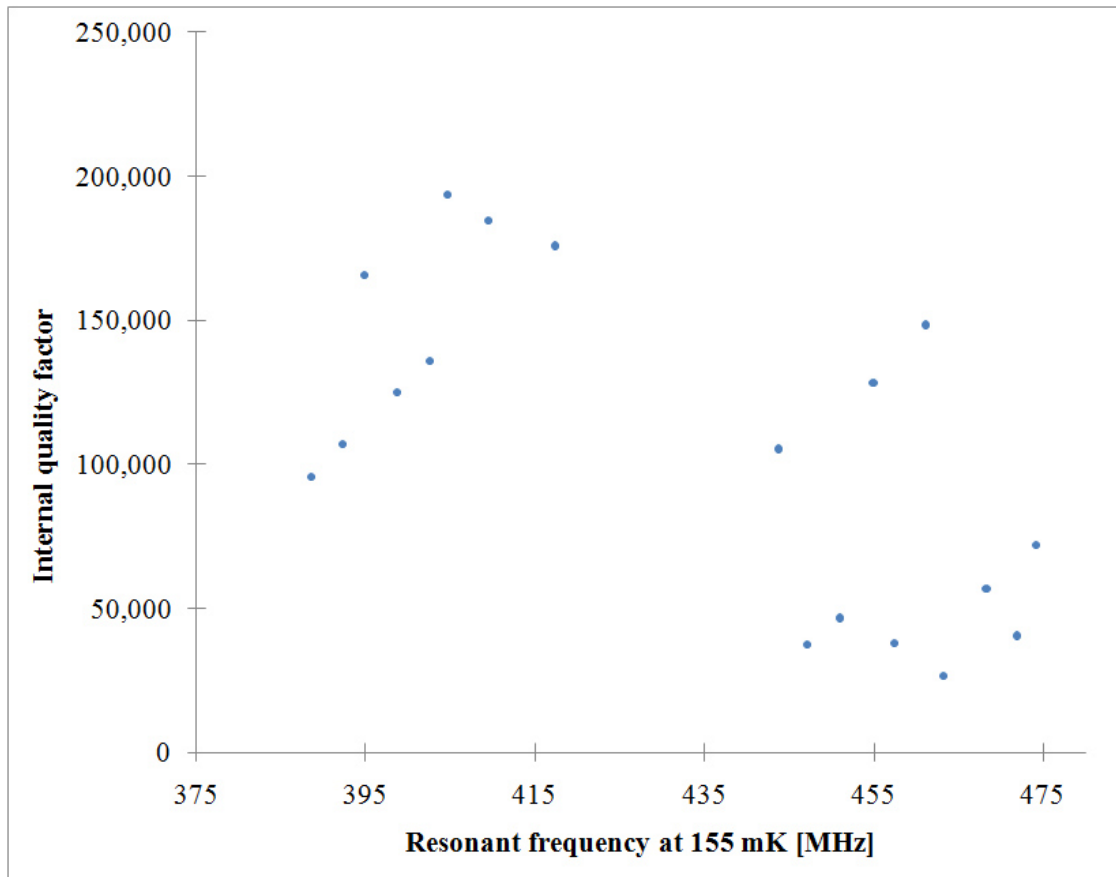
Figure 7.9: Internal quality factors at 155 mK plotted against the resonators' center frequencies. The pixels are clustered into two or three groups, but the dependence on frequency is not monotonic.

we nonetheless expect to see the resonators shift to a lower frequency compared to the lid-on dark tests as a result of optical response to this 'background' illumination. As shown in figure 7.10, we see the expected response.

In the same cooldown, the chip was illuminated with about -60 dBm of W-band power using the horn antenna. This is significantly brighter than a real observing scenario, but we wanted to start off by seeing if there was any optical response at all and map out the relative responses of each pixel. Figure 7.11 shows a zoomed-in view of the response from a single pixel. Figure 7.12 shows a map of the relative response for each pixel in the array. The beam from the horn antenna is nominally centered on the array, focused with a rexolite lens to a beam waist of about 1 cm diameter in the plane of the chip, and should have roughly Gaussian falloff towards the edges of the array. Figure
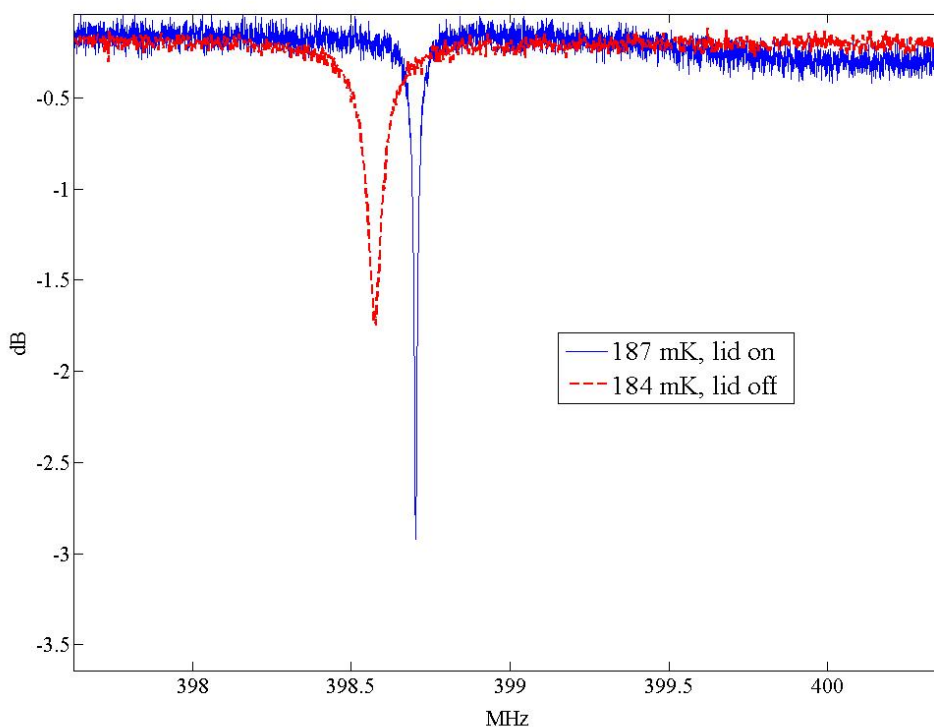
Figure 7.10: TiN resonator 4 response to 1.9 K background illumination from the walls of the liquid helium stage (red dashed line) compared to the un-illuminated, lid-on measurement of the same resonance at the same readout power (blue solid line). The measurements are at slightly different bath temperatures, but the bath temperature difference reduces the apparent effect (i.e. the illuminated measurement was taken at a slightly colder bath temperature. The optical response shifts the resonance down in frequency while the colder bath temperature shifts the resonance back up slightly in frequency). The effect of the 3 mK bath temperature shift is much smaller than the effect of the illumination. Note also the decrease in Q at higher optical powers. The measurements were taken with the same readout power.
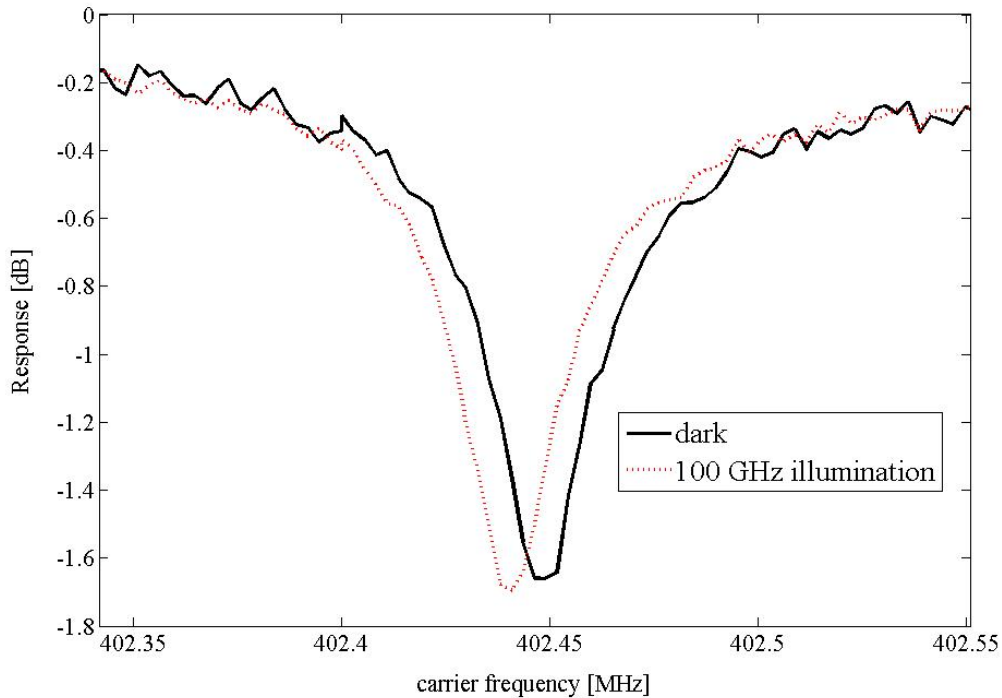
Figure 7.11: Response of resonator 5 to -60 dBm W-band illumination from the horn antenna. The dotted line is the response with w-band illumination from the horn antenna. The solid line shows the resonance 'dark' with only the 1.9 K background illumination from the walls of the liquid helium stage. The resonance shifts toward lower frequencies, as expected for an increase in L_k under illumination.

7.12, however, shows a hotspot of response in the lower left corner rather than near the array center. There are a few possible explanations for this behavior. The most probable explanation is simply that the alignment of the ADR stage (where the chip sits) relative to the helium stage (where the horn sits) shifted during the cooldown. While the ADR stage is carefully aligned before closing the cryostat, thermal contraction of the springs which hold the Kevlar suspension lines tight combined with relaxation of the Kevlar as it cools may allow some movement in the cold stage. The plate to which the chip holder is attached is regularly a few mm out of alignment when the cryostat is reopened after a cooldown. It's also possible that the lower left corner pixels really are significantly more responsive, however this seems less likely since that area has a variety of different pixel designs, including 12-meander pixels, 14-meander pixels, and a variety of coupling Qs.

Finally, we attempted to measure an optical response in a more realistic approximation of a

Figure 7.12: Fractional frequency response ($\Delta f / f_o$) of the resonators to ∼-60 dBm of w-band power. Black pixel is the blind niobium test resonator. Grey pixels were resonators that were either not visible at all or that were too poorly resolved to get a good center frequency measurement.

real observing scenario using the corrugated cold blackbody (section 6.2.2). Measurements were taken with the detectors looking at the beam-filling blackbody at 1.9 K, and 5.1 K. We expect the response here to be much smaller than the response to either the horn antenna illumination or to the background 1.9 K illumination (because the in-band power difference between 150 mK and 1.9 K is much larger than the in-band power difference between 1.9 K and 5.1 K). Unfortunately, we saw no response at all with these tests (see figure 7.13). However this is not particularly surprising. Recall the discussion above of the center frequency response to temperature changes. Those measurements showed that the superconducting gap energy for this TiN film is only about half of what we expect for a 1.16 K critical temperature. On the one hand, this means any optical illumination is breaking about twice as many Cooper pairs as expected. On the other hand, this also means that the ratio of the thermal energy of the bath temperature to the gap energy is much larger than expected, so we
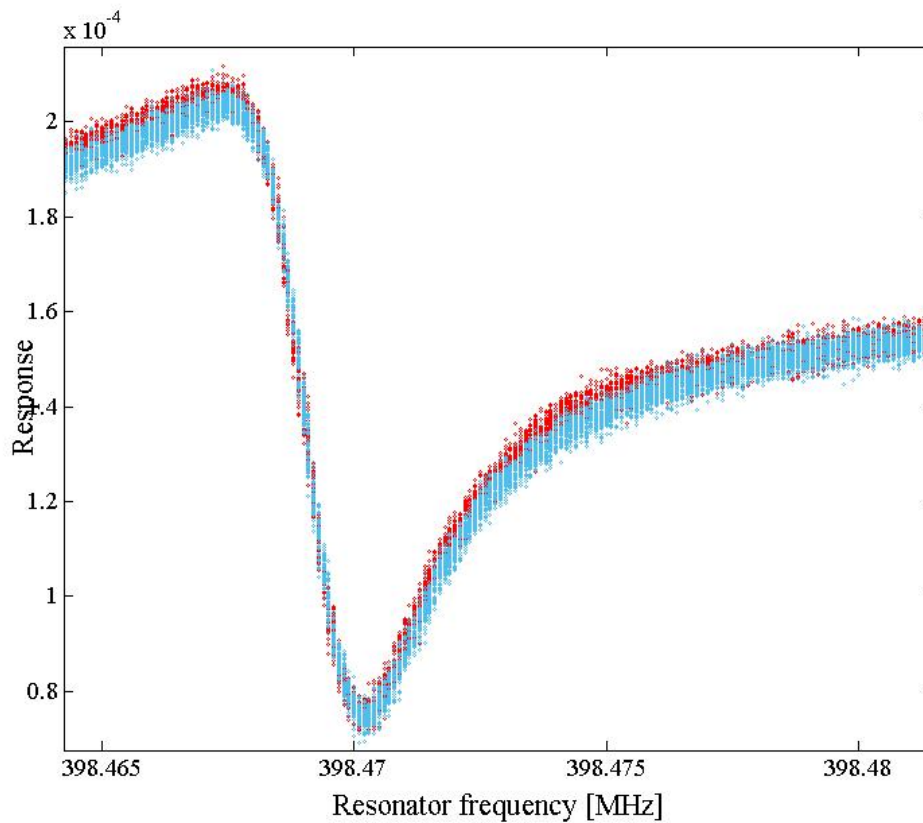
Figure 7.13: Response of resonator 4 (center of array) to 1.9 K blackbody (red dots) and 5.1 K blackbody (blue dots). The measurements were taken at bath temperatures of 161.8 mK and 161.7 mK respectively. The slight frequency shift is consistent with the shift expected from a 0.1 mK change in bath temperature.

expect significant thermal noise and significant thermal loading. Because the detectors are already seeing so much dissipation from thermal excitations, the optical response is reduced. There may be other effects reducing the optical response as well. For example, the optical coupling may be lower than expected. More data would be required to determine the exact factors contributing to the performance of the detectors.

CHAPTER 8

───

CONCLUSIONS

8.1 Summary

Described in this dissertation is a design for a quasi-lumped element direct-absorbing kinetic inductance detector array. Extensive semi-analytical calculations and EM simulations drove the initial design (geometry A), and these along with empirical results from testing of geometry A drove the final detector design (geometry B).

Significant emphasis was also placed on materials development. DC and RF properties of two types of molybdenum films and ten types of TiN films were studied in the course of this dissertation in an effort to identify the best possible material for the detector resonators.

Finally, while higher powered optical tests did reveal some optical responsivity in the titanium nitride trilayer devices with geometry B, more realistic lower powered tests with a cold blackbody showed no distinguishable optical response. This is likely due primarily to the lower than expected gap energy of the titanium nitride trilayer films used.

8.2 Recommended Future Work

Materials development is clearly critical to successful KID development at mm wavelengths, and additional work in this area will be essential for producing science-grade mm-wave KIDs. Several groups are currently investigating the non-Mattis-Bardeen behavior of TiN, though publications have been sparse. The Mazin group at UCSB has also recently developed a new material with potential applications for mm-wave KIDS. Their platinum silicide has a critical temperature near 1 K and good kinetic inductance properties, though its characteristic quasiparticle recombination time is shorter

than that of TiN, which makes it perform better for photon counting KIDs (the Mazin group's intended application) but incurs a noise penalty for more traditional 'photon flux' applications [113]. Further investigation of alternative materials suitable for w-band and lower-frequency KIDs would be valuable to the field.

While it is unlikely that pure molybdenum will ever be a useful material for kinetic inductance detectors (though molybdenum bilayers and nitrides are already in use for such devices where higher critical temperatures are desirable) it would nonetheless be interesting and possibly fruitful to conduct a more thorough study of the apparent double gap behavior of molybdenum, which did not appear in the literature prior to our measurement.

On a more local scale, computerized PID control of the cryostat temperature will be essential to making better optical response measurements with this experimental setup in the future, as will better electromagnetic shielding for the cryostat. Both of these improvements have already been undertaken by upcoming students in the group and will be fully implemented in the near future. There is also significant room for improvement in the readout, which would enable better studies of the noise properties of KID detectors. Ideally, an FPGA-based readout (for example, based on ROACH boards originally developed for radio astronomy) would be used, but these are prohibitively expensive. Alternatively, some improvement could be gained with the existing equipment by optimizing the VNA readout code to run faster and by integrating the ADC/DAC more tightly with the rest of the hardware/software interface.

APPENDIX A

RUN SHEETS

Except where noted, all of the recipes that follow were developed by Dr. Ari Brown of NASA Goddard Space Flight Center or are very slight modifications of his recipes.

A.1 Etched Niobium

1. Deposition

   a) DC megnetron sputter with Ar at 3.75 mTorr, 500 W

2. Patterning

   a) spin HMDS and 1827

   b) soft bake

   c) Expose

   d) Develop (bucket or spray developer)

3. RIE Etching

   a) condition chamber with dummy wafer running all process gases

   b) Etch

      i. O2 ash

     ii. etch: 100 W, 75 % CF4 10 % O2.

     iii. O2 ash

4. Cleanup

    a) Solvent strip photoresist

    b) Ash HMDS

    c) Optional EKC strip

A.2   Nb Liftoff

1. Spin PMMA, vacuum bake at 180 C

2. Deposit Ge hard mask in e-beam chamber

    a) ramp to 50 mA

    b) Deposit $\sim$1270 Å

    c) Slowly ramp down current.

3. Pattern Ge and PMMA

    a) O2 ash

    b) spin HMDS and thinned 1811

    c) Soft bake

    d) expose

    e) Develop: spray developer

4. RIE etch Ge

    a) Ash HMDS

    b) Condition metals RIE with dummy wafer, run all process gases

    c) Etch: 70W, 30% SF6, 6% O2

    d) Ash PMMA

5. Deposit Nb in AJA

6. Liftoff in acetone

A.3   Titanium/Gold

1. Pattern

   a) Spin HMDS, PMGI, 1811

   b) soft bake

   c) Expose

   d) Bucket develop

   e) O2 ash HMDS

2. Deposit Ti/Au in Denton e-beam chamber

   a) Ramp up to 60 mA

   b) Deposit ~ 200Å Ti and ~ 1500Å Au

3. Liftoff in acetone

A.4   TiN/Ti/TiN trilayer, chlorine etch

1. Spin HMDS and 1811

2. Expose

3. Spray develop

4. Etch

   a) O2 ash

   b) Trion chlorine etcher:

      i. 10 mT, with BCl3, Cl2, Ar, and O2 with 350 W ICP power, 50 W RIE power.

   c) O2 ash

A.5   Molybdenum Etch

1. Deposit Mo v1 recipe

   a) DC magnetron sputter: with 1.4 mTorr Ar @ 250 W, with 10 min getter of Ti @ 200 W and 1 mTorr

2. Deposit Mo v2 recipe (this recipe was provided by Dr. Kevin Denis of NASA Goddard and deposited with his assistance)

   a) DC magnetron sputter: 700 W with 1.3 mTorr Ar

3. Spin Photoresist: Genarc and thinned 1811 OR HMDS and 1811

   a) Soft bake

4. Expose

5. Develop (spray or bucket)

6. O2 ash HMDS

7. Etch: 45 C E6 or RIE dry etch with SF6

A.6   Si Etch

1. Pattern

   a) Spin HMDS and 1811

   b) Soft bake

   c) Expose

   d) Spray developer

2. RIE etch

a) O2 ash

b) SI etch: 50 W, 30% SF6, 8% O2

c) O2 ash

A.7   Titanium Nitride, HCl/H202 etch

1. Pattern

   a) Spin HMDS and 1811

   b) Expose

   c) Spray developer

   d) Ash HMDS

2. Etch in SC2 H20:Hcl:H2O2 12:1:1 at 65 C

3. Ash HMDS

APPENDIX B

————

BLUE DEWAR PINOUT

B.1   Blue Breakout Box

Bendix	MDM-C	Device
[s,t]	[21,8]	Chip
[m,n]	[20,7]	Chip
[i,U]	[23,10]	MDM wire 10 now broken; do not use
[h,T]	[22,9]	Chip
[S,R]	[17,4]	Chip
[f,P]	[16,3]	Chip
[p,q]	[19,6]	SiGe Amp
[r,g]	[18,5]	Heat switch monitor

B.2 Yellow Breakout Box

Device	MDM-B	Bendix	D-sub	Usable? [1]
	1	L		
	2	K		
Lakeshore b shield	3	Y	2	Y
Lakeshore a	4	H	17	Y
GRT 8 I+ [2]	5	F	18	Y
(Old CADR ground)	6	Z	3	Y
	7	a		
4K	8	N	21	Y
	9	-		
CADR shield	10	U	8	Y
GRT 5 V-	11	D	24	Y
	12	B	25	Y
	13	-		
	14	M		
	15	J		
Lakeshore b pin	16	X	1	Y
Lakeshore a	17	G	5	Y
GRT 9 I-	18	E	6	Y
CADR pin	19	c	15	Y
	20	b		
4K	21	P	9	Y
	22	-		
new GRT 4 V+	23	T	7	Y
	24	C	12	Y
	25	A	13	Y
77K		S	10	Y
77K		R	22	Y
		V		
		W		

---

[1] i.e. does the electrical continuity go all the way through from the MDM through the bendix & D-sub (regardless of whether it's currently in use)

[2] numbers following GRT (8 in this case) refer to the relevant pin on the 9-pin D-sub on the yellow box

APPENDIX C

BLUE DEWAR OPERATING PROCEDURES

C.1   Closing up

1. Check electrical continuity. These are approximate expected resistances at room temp.

   a) Thermometry (measured from yellow breakout box)

      i. 4K: 1660 Ω

      ii. 77K: 1480 Ω

      iii. GRT: 150-200 Ω 2-wire measurement (5 Ω 4-wire measurement)

      iv. Lakeshore: two pairs at 1180 Ω, two pairs short (150-ish Ω)

      v. CADR: 1304 Ω

   b) Heat switch power: 110 Ω measured at He exhaust bendix (pin D + ground)

   c) Heat switch monitor: 75 Ω measured at [r,g] on blue breakout box

   d) DC devices: leads alone are about 150 Ω round-trip. Check for expected room temp resistance across device and for unexpected shorts to ground.

   e) as of 8/25/2015, working twisted pairs on blue box are: pq, rg, hT, SR, fP, mn, sT

   f) rg is usually the HS monitor and pq is usually the SiGe amp

2. Install 4K shield

   a) Put on shield and screw down (there's an extra-long hex driver for this purpose). You only need to do a handful of screws, but make sure the ones you leave in are snug. Remove any you can't get to catch threads using the grabber-claw tool, and make sure to get the washers as well (lest they rattle around during the cooldown and make thermal shorts or break wirebonds)

b) Alignment is determined by where the little slot is for the 100 GHz line. There is only one correct orientation. Do not smash the 100 GHz line.

c) Plug in the 4K thermometer, amp, MDM cables, DC devices, etc. Check again for electrical continuity.

d) Tape MDM cables to the outside of the 4K shield using mylar tape. Wipe down the shield with iso first or the mylar tape won't stick well.

e) Tape around seam and around top of 4K shield with 2" aluminum tape. Mash the tape down to make a good, light-tight seal using the handle of a screw driver or similar implement. Beware, bumpy spots in tape can cause thermal touches, and gaps/tears make light leaks.

f) Cut a V slit in the Al tape that's going around the top of the 4K shield. This will be the gap for the RF coax.

3. Install 77K shield

a) Slide the shield on. Align the arrows at the bottom; there is only one correct orientation.

b) Push the shield down so the holes line up with the threaded holes on the 77K plate. Make sure it's resting firmly on all three little copper "feet" that stick out from the 77K plate or you'll struggle to get the lids on later.

c) Screw down. Use all the screws to reduce light leaks.

d) Tape around the top with Al tape. Cut a V slit for the RF coax.

4. Install the 300K vacuum shell

a) Check o-ring for proper seating and cleanliness

b) Put the shield on. The tape should line up with the vacuum valve; there is only one correct orientation. Be careful of the RF lines as you lower the shield; try not to bend them too much or jerk them around.

c) Screw down. Use all the screws.

5. Install the lids

    a) Screw the RF coax into the coax-waveguide adapters. They should be very snug, but don't crank on it.

    b) Dab thermal grease in the slot in the 4K shield where the RF cables pass through and also on the RF cables where they pass throught he slot. This helps with thermal sinking and possibly helps reduce light leaks.

    c) Final check of cold stage electrical connections. This is your last chance to easily fix things.

    d) Install 4K lid. The circled hole lines up with the broken off screw; there is only one correct orientation. Be careful not to smash the baffle into the RF lines or anything else delicate on the cold stage. Use a thin implement (like the back end of a pair of tweezers) to work the lid down through the tape cylinder. Screw the lid down, making sure the RF lines are staying in their slot and not getting squished by the lid. You only need to do a few screws. Then fold down the tape and smush it down with a screwdriver handle.

    e) Check for touches with a slip of paper. You can use a screwdriver as a lever to slightly push the 77K shield around relative to the 4K shield to help eliminate any touches.

    f) Install 77K lid. Essentially the same procedure; work it down through the tape cylinder, screw down with a few screws, be careful of the RF lines, fold down the tape, and check for touches.

    g) Install 300K lid. Use all of the screws (except the ones that are stripped, which have Xes). To avoid stripping more screws, do NOT crank on them. They don't need to be super tight to hold the vacuum; just snug.

C.2   Cooling to 77K

1. Pump out

a) Check the electrical connections again before you waste time pumping.

b) Pump-out takes at least 6 hours, more if the Dewar has been open a long time.

c) Very shortly after starting the pump, the vacuum will be strong enough to hold the 300 K lid on without aid of the screws. As a safety measure (because there is no other emergency pressure relief), it is wise to loosen (but not remove) the lid screws, so that the Dewar can vent freely in the event of an unplanned over-pressure event.

2. Liquid nitrogen initial fill

a) Maximum pressure to begin filling LN2 is 2×10^{-4} torr. Otherwise you'll get too much icing, the o-rings will freeze too early, the vacuum will get too bad too soon, and the fill will take forever.

b) Fill the LHe tank first (less ice, faster fill). When 4K=2200Ω, it's cold. When you can see little droplets splashing up from the vent side, it's full.

c) Takes about 1 hr typically for the initial fill, but up to 2 hrs, especially if it's humid or if you were pushing your luck on the pressure when you started. Expect the pressure to rise significantly during the fill. It'll drop back down when the o-rings thaw out.

d) Fill the LN2 tank next. Cold when 77K=2000Ω. Full when spraying out of fill tube.

e) Takes 10-15 minutes for the initial fill.

3. Liquid nitrogen subsequent fills

a) Will need to be refilled about 5 hours after you finished the initial fill. Once it's at 77K, the big tank will hold overnight (12-16 hrs) but the small tank will run out.

C.3 Cooling to 4K

1. You can begin filling LHe when the CADR is over 1500Ω if you're in a hurry, but wait until CADR=1620Ω or higher to save a lot of helium.

2. Check your electrical connections again.

3. Disconnect the vacuum pump and lines from the Dewar. Be very careful with the valves so that you are 100% sure not to accidentally vent the dewar or contaminate the pump. Turn the turbo off and leave it alone to spin down while you start filling.

4. Put a cold-safe container (such as a styrofoam bucket) under the dewar and dump out any remaining LN2. Rock the Dewar back and forth a couple times to get the last few drops.

5. Refill the LN2 tank with LN2.

6. Fill the LHe tank with LHe.

   a) Pressurize the storage tank with the soccer ball

   b) When the 4K=20kΩ, it's cold and starting to fill. Monitor with He level sensor to determine when the tank is full. The sensor usually only goes up to 98%; don't wait for it to get to 100.

   c) Initial fill takes 30-40 min.

   d) Release all of the He storage dewar pressure before pulling out the transfer line, else you'll blow off half your tank as you pull the line out.

   e) Filling is MUCH easier with a full or nearly-full storage dewar. Plan accordingly.

   f) At some point during the He fill, the turbo will finish spinning down. When it does, reattach the pump line to the dewar. Open the pump line leading to the turbo (but NOT yet the dewar valve) and pump out the line. When the line pressure reaches 5×10^{-6} or so, you can open the dewar valve safely. Always think very carefully about your vacuum setup before touching any valves. Be sure to never vent gas into a cold dewar (ice!) and never vent gas into a running turbo (pump contamination, or even mechanical damage).

7. Cooling to 4K

   a) LHe will need to be refilled 4-5 hrs from when you started filling

b) Time from beginning of LHe fill to 4.4K is about 5-6 hrs.

c) Keep an eye also on the nitrogen level in the LN tank. LHe will boil off much faster if the LN runs out.

d) Once the GRT is reading below 4.5 K or so, a full LHe tank will hold overnight. Make sure you start with a full LN tank, though the LN will almost certainly run out overnight.

e) If you're going to cycle the ADR starting from un-pumped LHe, you can start the magnet ramp up around 4.4K.

C.4   Cooling to 2K

1. Set up

   a) Refill liquid helium and liquid nitrogen. You can refill the liquid nitrogen during the pumping procedure, but not the helium, so make sure you're starting with a full tank.

   b) Attach pressure gauges to both fill side and vent sides of He tank. One of the pressure guages is attached to the backfilling jig (the one with the needle valve and hose barb); I usually put that one on the fill side and pump from the vent side so that the side with the larger aperture is the one being pumped through. But really you can go either way. Leave the needle valve on the backfilling jig OPEN until you are ready to start pumping so that pressure doesn't build up when you've closed off all the lines.

   c) Attach the long flexible plastic pump line to the side you're going to pump from (probably the vent side) and attach the other end to either the cart pump or the line going to the pump room. You'll want a relatively fine valve somewhere in the line between the dewar and the pump.

2. Start pumping

   a) Start pumping at a slow rate (1 T/sec or so) by slowly opening the fine valve on the pump line.

b) The guage on the far side will lag slightly behind the gauge on the pump side, but they should both move together. If the difference between their pressure readings is increasing, this is a symptom of an ice plug. You should monitor it closely and be ready to intervene if things get worse. The two guages currently differ by 15 Torr even when the actual pressure is the same.

c) If you start seeing oscillations in the pressure, try either opening the valve a little or closing it a little.

d) Continue slowly opening the valve until it's all the way open, over 30-60 minutes. Temperature should drop below 2 K.

e) If you're going to cycle the ADR, you can start ramping up the magnet around 2.4K

3. When you're done pumping for the day

a) Backfill the helium tank with warm helium gas

   i. Connect a line (slightly above atmospheric pressure) from a helium cylinder to the hose barb on the backfilling jig.

   ii. Valve off the pump and switch it off

   iii. Slowly open the needle valve on the backfilling jig and allow He gas to flow. Monitor the pressure gauges, and when the pressure inside is slightly above atmospheric pressure, disconnect the pump line from the dewar. Make sure you can feel the helium gas flowing out of the dewar on the (formerly) pump side; that means there's no ice plug, or at least not a completely closed plug.

   iv. Turn off the helium gas and disconnect the gas line

b) If you're going to continue the next day

   i. If you're going to refill He and pump again the next day, you must intervene to clear the ice constriction out of the vent side or you'll have poor pumping results the next day. After you have backfilled but before you refill the LHe, run He gas through the He tank from the vent side (running it in the fill side and out the vent side like you

normally do for backfilling won't clear the ice) for a few minutes. Sometimes if you stand there and listen you can hear the sound of the He flow change suddenly when the ice clears. If you still have the pressure gauges hooked up, you can also see the ice (if there was any) clear on the pressure readings.

ii. Refill with LHe and LN2

c) If you're not going to continue the next day

i. Turn the cryostat over and dump any remaining cryogens

ii. Leave the cryostat upside down (fill tubes pointing down)for at least a few hours, or all night. This position helps prevent ice plugs from forming while the helium tank is still extremely cold.

iii. For extra insurance against ice plugs, connect tubes to the fill and vent ports. The longer path length helps keep air from reaching the cold part of the He tank and freezing up. There is a Tygon tube stuck to a KF-40 hose barb and a neoprene tube lying around for this purpose.

C.5   Cycling the ADR

1. Get close to LHe base temp. Wait until you're at about 4.4K or colder for un-pumped LHe, or about 2.4K or colder for pumped LHe.

2. Ramp up: Use the Labview program ramp_HP_7.vi to ramp up the magnet from 0 A to 7 A in 60 minutes. Expect the GRT temperature reading and the helium boiloff rate to increase quite a bit while the magnet current is high.

3. Soak stage: Let the magnet sit at 7 A until the GRT temperature reading drops back down to the relevant base temperature (4.2 K for unpumped LHe or <1.9 K for pumped LHe). Waiting longer and letting things get as cold as possible makes a difference to the base temperature you'll ultimately achieve. If getting as cold as possible is important, wait for it to get as cold

as possible. If a cold base temperature is less critical, save some time by moving to the next step at a slightly higher temperature.

4. Open the heat switch

5. Ramp down the magnet current from 7 A to 0 A in 30-40 min.

6. Wait for the temperature to level off. On a good day, you'll reach 200 mK if you started from un-pumped LHe, or 140 mK if you started from pumped LHe.

7. When you're done, close the heat switch again before things warm up too much on their own. It will be harder to get it to actuate if things are too warm.

C.6   Additional notes

1. Useful Labview programs

   a) For the VNA: Vector Network Analyzer 8753D.vi

      i. Getting it to work: The main trick here is the file naming. Put in the file name box the path to the folder you want, plus whatever you want the first file to be named (don't use endings like .txt or .csv, just use normal characters). If you're doing more than one segment, segments after the first will automatically have numbers appended on to the end of the file name. The formatting of the appended numbers is kind of weird. It's a quirk of how labview allows you to do automatic naming, not a sign that you did something wrong. I generally just give the folder a descriptive name, and then make the first file called something extremely simple like 'a'. Also, beware that the frequencies are in GHz, so make sure you've got your decimals in the right place. The frequency range you put in will be divided up evenly into however many segments you tell it to do. Don't forget to set the number of points per sweep to 1601 and set the IF bandwidth to whatever you want. Leave everything else alone. The averaging and smoothing features don't work; don't try to use them.

b) For the SNA: Driver2.vi

    i. Getting it to work: The files live in the 'Network Analyzer' folder on Gates. Also in that folder is a text file with instructions.

c) For the lock-in amp and thermometry: cryogenics measurement new.vi

    i. Getting it to work: Open the program. Go to window>show block diagram. Near the upper left part, double click on the first cryocon box. In the window that pops up, click the VISA IN dropdown menu and pick cryocon. save. close that window. on the full block diagram, do file>'save all' and close the block diagram. In the main view, in the lakeshore section, select the lakeshore from the VISA In menu. Select Cernox fromt he sensor type dropdown menu and select user curve 1. On the lock-in section put in whatever settings you want. When you start running the program, the lockin settings on the computer will be applied to the lockin (not the other way around), so make sure the computer says what you want the lockin to be doing. Put the path to where you want the data saved in the box at the top.

d) For ramping the magnet: ramp_HP_7.vi

    i. Getting it to work: Nothing special here. Don't forget to change where it saves the file (it defaults to some old folder no longer used). Also don't forget to change it to a current ramp instead of a voltage ramp (default).

e) Instrument discovery tool: Meausrement and Automation (National Instruments)

    i. Getting it to work: If one of the instruments isn't being "seen" by labview, try running the instrument discovery tool, called 'Meausrement and Automation' (shortcut on Gates's desktop). On the left side, click the little dropdown arrow for 'devices and interfaces' and give it a moment to think... GPIB should appear as an option after a few seconds. Click on GPIB. Then at the bottom in the right pane, there should be a list of all the boxes that are hooked up to GPIB. If not everything is there that's supposed to be, click 'scan for instruments' at the top. If it's still not showing up,

check that the GPIB cable is plugged in well. Sometimes they unplug themselves under their own weight.

2. Where do all the wires come out?

    a) Bendix on the He vent

        i. 4 wires for the He level sensor: red=B, black=A, green=C, white=N

        ii. 1 wire for the heat switch power: D. Return is dewar ground.

        iii. Heater (U) doesn't currently work because the safety switch on the 4K place is broken (permanently open circuit). Don't run it without replacing the safety; it's supposed to be closed when cold and open at room temp to prevent accidentally overheating the dewar and killing the salt pill or blowing up the pressure vessel.

        iv. ADR magnet power: [L,M] and [K,T], doubled to achieve adequate current rating. These are connected each to a bundle of three brass wires (again, to achieve adequate current rating).

        v. Ground: (F) Pin F is not automatically connected to dewar ground in the current configuration. Instead, there's a bare solder nub in the cord bundle which gts alligator clipped to the dewar ground strap. This (unsurprisingly) is apt to cause electrical pickup, so make sure to unplug the whole Bendix (including the grounding clip) after you have ramped the magnet all the way down. Remember, DO NOT unplug it while the magnet is running unless massive back EMF is your favorite. After the magnet has been ramped down, you can install the filter dongle, which has a proper ground connection and a connection for the blackbody heater (only).

        vi. If in the future we install the 4-wire heat switch made by Brandon, it is planned to go on pins P, R, and E, plus the current one, D. These wires are all together in one brass wire bundle.

        vii. Spares: (H, G) These wires aren't currently connected to anything, but they go through the He tank feedthrough.

viii. No connection: (J, S) These are not connected to anything. They don't connect to any brass wires or to anything that goes through the He tank feedthrough.

3. Breakout boxes

a) Yellow: All of the thermometry comes out here. Everything works, though the heat switch monitor on this side is only useful if you don't have the RF coax lines going to the cold stage (it checks of dewar ground and cold stage ground are the same, which is a good monitor for thermal contact only if the NbTi lines are not there). The actual wire comes out on the copper board that holds the GRT and CADR.

b) Blue: More broken than not here. As soon as there is funding available, a new cryoloom MDM cable should be installed here. Historically there were actually two 25-pin cryoloom cables going to the blue box. Currently on the 4K shield the copper blocks where the MDMs plug in are labeled B and C... MDM-B goes to the yellow box. MDM-C goes to the blue box. The block for A used to be installed on the side towards the vacuum valve. The cable (now taped to the 77K cold plate) has so many broken wires it wasn't useful and we uninstalled the block it went to because there wasn't room on the cold stage for that many DC devices anyway. But many of the wires otherwise go through, so many of the unused connections on the blue box could be resurrected if MDM-A were reinstalled with a new cryoloom cable.

4. Miscellaneous other notes:

a) He tank feedthrough: There's a spare one in the red tool cart. Also some spare older ones that don't fit as many wires.

b) The brass caps have two different bolt circles (oops). The one in the lid and the one off by itself on the side of the dewar are 4-40 with a bolt circle (diameter) of 1.600". The ones that are original to the dewar, in a ring together around the base are also 4-40, but with a bolt circle of 1.630". There are a couple spare brass caps of each size in the red tool cart.

c) The salt pill permanently ceases to be paramagnetic at 40 C.

APPENDIX D

IQ DEMODULATOR SETUP
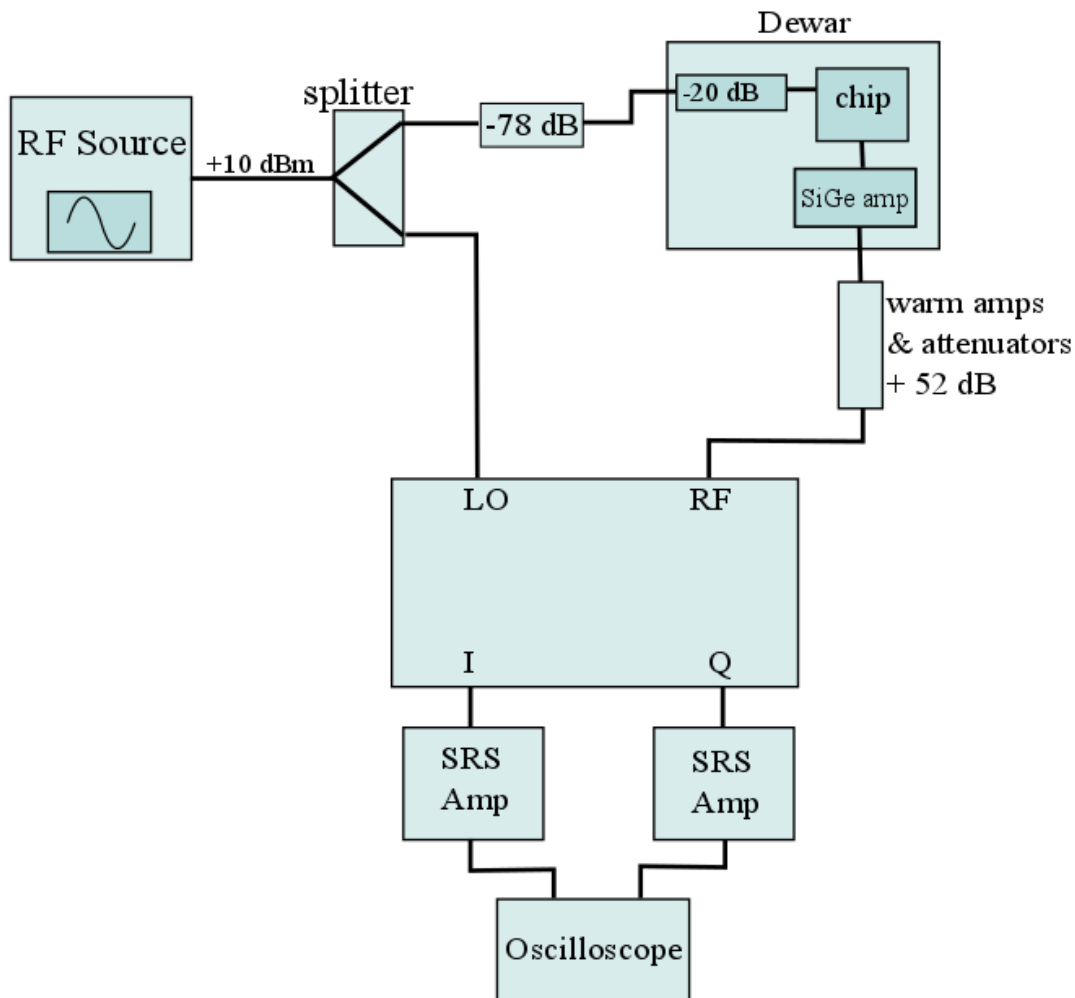
Figure D.1: Schematic of the IQ demodulator setup. See below for a more detailed description of each part.

The RF source we used was port 1 of our VNA. The -78 dB attenuator at the top of the schematic consists of 37 dB of attenuation from several SMA coaxial attenuators connected in series plus up to 41 dB of attenuation from a variable 'switch' attenuator which was used to adjust the amount of

power arriving at the chip. The warm amplifiers and attenuators on the right side of the schematic were three Mini-Circuits ZFL-1000LN+ 0.1-1000 MHz amplifiers connected in series, with about 10 dB of coaxial SMA attenuators split into groups of 3 or 4 dB between each amplifier and after the last amplifier. The SRS amplifiers at the bottom of the schematic were two nominally-identical Stanford Research Systems SR560 low-noise preamplifiers. The IQ demodulator was a custom part from Polyphase Microwave Inc based closely on their standard part AD0105B, but with a slight shift upwards in frequency to 400-700 MHz (instead of 100-500 MHz for the standard part). For some measurements, the oscilloscope shown in the schematic was replaced with an USB-1608-FS-Plus ADC from the Measurement Computing Corporation, read out with a laptop running an oscilloscope emulation software package. For a more detailed schematic of the RF components inside the Dewar, see figure 6.12. The maximum safe input power to the RF port on the IQ demodulator is +20 dBm. The maximum safe input power to the LO port is +10 dBm (+5 dBm typical).

DISCARD THIS PAGE

COLOPHON

This dissertation was prepared with literal blood, sweat, and tears, and also a TeX template adapted by William C. Benton from the venerable withesis.cls. The years spent researching and writing it have really all been a thinly-veiled setup for the bad pun in the dedication.

BIBLIOGRAPHY

[1] Kevork N Abazajian, K Arnold, J Austermann, BA Benson, C Bischoff, J Bock, JR Bond, J Borrill, E Calabrese, JE Carlstrom, et al. Neutrino physics from the cosmic microwave background and large scale structure. *Astroparticle Physics*, 63:66–80, 2015.

[2] John C Mather, ES Cheng, RE Eplee Jr, RB Isaacman, SS Meyer, RA Shafer, R Weiss, EL Wright, CL Bennett, NW Boggess, et al. A preliminary measurement of the cosmic microwave background spectrum by the cosmic background explorer (cobe) satellite. *The Astrophysical Journal*, 354:L37–L40, 1990.

[3] D Larson, J Dunkley, G Hinshaw, E Komatsu, MR Nolta, CL Bennett, B Gold, M Halpern, RS Hill, N Jarosik, et al. Seven-year wilkinson microwave anisotropy probe (wmap wmap is the result of a partnership between princeton university and nasa's goddard space flight center. scientific guidance is provided by the wmap science team.) observations: Power spectra and wmap-derived parameters. *The Astrophysical Journal Supplement Series*, 192(2):16, 2011.

[4] B. A. Mazin. *Microwave kinetic inductance detectors*. PhD thesis, California Institute of Technology, California, USA, November 2005.

[5] Peter K Day, Henry G LeDuc, Benjamin A Mazin, Anastasios Vayonakis, and Jonas Zmuidzinas. A broadband superconducting detector suitable for use in large arrays. *Nature*, 425(6960):817–821, 2003.

[6] S. Scully, D. Burke, C. O'Sullivan, D. Gayer, M. Gradziel, J. A. Murphy, M. De Petris, D. Buzi, M. Zannoni, A Mennella, M. Gervasi, A. Tartari, B. Maffei, J. Aumont, S. Banfi, P. Battaglia, E. S. Battistelli, A. Baù, B. Bélier, D. Bennet, L. Bergé, J.-Ph. Bernard, M. Bersanelli, M.-A. Bigot-Sazy, N. Bleurvacq, G. Bordier, J. Brossard, E. F. Bunn, D. Cammileri, F. Cavaliere,

P. Chanial, C. Chapron, A. Coppolecchia, F. Couchot, G. D'Alessandro, P. De Bernardis, T. Decourcelle, F. Del Torto, L. Dumoulin, C. Franceschet, A. Gault, A. Ghribi, M. Giard, Y. Giraud-Héraud, L. Grandsire, J. C. Hamilton, V. Haynes, S. Henrot-Versillé, N. Holtzer, J. Kaplan, A. Korotkov, J. Lande, A. Lowitz, S. Marnieros, J. Martino, S. Masi, Mark McCulloch, Simon Melhuish, L. Montier, D. Néel, M. W. Ng, F. Pajot, A. Passerini, C. Perbost, O. Perdereau, F. Piacentini, M. Piat, L. Piccirillo, G. Pisano, D. Prêle, R. Puddu, D. Rambaud, O. Rigaut, M. Salatino, A. Schillaci, M. Stolpovskiy, P. Timbie, M. Tristram, G. Tucker, D. Viganò, F. Voisin, and B. Watson. Optical design and modelling of the qubic instrument, a next-generation quasi-optical bolometric interferometer for cosmology. *Proc. SPIE*, 9914:99142S–99142S–15, 2016.

[7] A. Ghribi, J. Aumont, E. S. Battistelli, A. Bau, B. Bélier, L. Bergé, J.-Ph. Bernard, M. Bersanelli, M.-A. Bigot-Sazy, G. Bordier, E. T. Bunn, F. Cavaliere, P. Chanial, A. Coppolecchia, T. Decourcelle, P. De Bernardis, M. De Petris, A.-A. Drilien, L. Dumoulin, M. C. Falvella, A. Gault, M. Gervasi, M. Giard, M. Gradziel, L. Grandsire, D. Gayer, J.-Ch. Hamilton, V. Haynes, Y. Giraud-Héraud, N. Holtzer, J. Kaplan, A. Korotkov, J. Lande, A. Lowitz, B. Maffei, S. Marnieros, J. Martino, S. Masi, A. Mennella, L. Montier, A. Murphy, M. W. Ng, E. Olivieri, F. Pajot, A. Passerini, F. Piacentini, M. Piat, L. Piccirillo, G. Pisano, D. Prêle, D. Rambaud, O. Rigaut, C. Rosset, M. Salatino, A. Schillaci, S. Scully, C. O'Sullivan, A. Tartari, P. Timbie, G. Tucker, L. Vibert, F. Voisin, B. Watson, and M. Zannoni. Latest progress on the qubic instrument. *Journal of Low Temperature Physics*, 176(5-6):698–704, 2014.

[8] Yifang Chen, Kaiwu Peng, and Zheng Cui. A lift-off process for high resolution patterns using pmma/lor resist stack. *Microelectronic engineering*, 73:278–281, 2004.

[9] E. J. Wollack, D. J. Fixsen, R. Henry, A. Kogut, M. Limon, and P. Mirel. Electromagnetic and thermal properties of a conductively loaded epoxy. *International Journal of Infrared and Millimeter Waves*, 29(1):51–61, 2008.

[10] Alexander Friedmann. On the curvature of space. *Z. Phys*, 10:377–386, 1922.

[11] Georges Lemaître. Un univers homogène de masse constante et de rayon croissant rendant compte de la vitesse radiale des nébuleuses extra-galactiques. In *Annales de la Société scientifique de Bruxelles*, volume 47, pages 49–59, 1927.

[12] Edwin Hubble. A relation between distance and radial velocity among extra-galactic nebulae. *Proceedings of the National Academy of Sciences*, 15(3):168–173, 1929.

[13] Ralph A Alpher and Robert C Herman. On the relative abundance of the elements. *Physical Review*, 74(12):1737, 1948.

[14] P James E Peebles, Lyman A Page Jr, and R Bruce Partridge. *Finding the big bang.* Cambridge University Press, 2009.

[15] Robert B Partridge. *3K: the cosmic microwave background radiation*, volume 25. Cambridge University Press, 2007.

[16] Planck Collaboration, R Adam, PAR Ade, N Aghanim, Y Akrami, MIR Alves, M Arnaud, F Arroja, J Aumont, C Baccigalupi, M Ballardini, et al. Planck 2015 results. i. overview of products and scientific results. *arXiv preprint arXiv:1502.01582*, 2015.

[17] Peter AR Ade, N Aghanim, Z Ahmed, RW Aikin, KD Alexander, M Arnaud, J Aumont, C Baccigalupi, Anthony J Banday, D Barkats, et al. Joint analysis of bicep2/keck array and planck data. *Physical review letters*, 114(10):101301, 2015.

[18] Planck Collaboration et al. Planck 2015 results. xiii. cosmological parameters. arxiv preprint. *arXiv*, 1502, 2015.

[19] J Chluba and RA Sunyaev. Free-bound emission from cosmological hydrogen recombination. *Astronomy & Astrophysics*, 458(2):L29–L32, 2006.

[20] Alan H Guth. Inflationary universe: A possible solution to the horizon and flatness problems. *Physical Review D*, 23(2):347, 1981.

[21] Scott Dodelson. *Modern cosmology.* Academic press, 2003.

[22] Wayne Hu and Martin White. A cmb polarization primer. *New Astronomy*, 2(4):323–344, 1997.

[23] Kevork N Abazajian, Peter Adshead, Zeeshan Ahmed, Steven W Allen, David Alonso, Kam S Arnold, Carlo Baccigalupi, James G Bartlett, Nicholas Battaglia, Bradford A Benson, et al. Cmb-s4 science book. *arXiv preprint arXiv:1610.02743*, 2016.

[24] Xuelei Chen and Marc Kamionkowski. Particle decays during the cosmic dark ages. *Physical Review D*, 70(4):043502, 2004.

[25] Nikhil Padmanabhan and Douglas P Finkbeiner. Detecting dark matter annihilation with cmb polarization: Signatures and experimental prospects. *Physical Review D*, 72(2):023508, 2005.

[26] Andreas Albrecht, Gary Bernstein, Robert Cahn, Wendy L Freedman, Jacqueline Hewitt, Wayne Hu, John Huth, Marc Kamionkowski, Edward W Kolb, Lloyd Knox, et al. Report of the dark energy task force. *arXiv preprint astro-ph/0609591*, 2006.

[27] Eva-Maria Mueller, Francesco De Bernardis, Rachel Bean, and Michael D Niemack. Constraints on gravity and dark energy from the pairwise kinematic sunyaev–zel'dovich effect. *The Astrophysical Journal*, 808(1):47, 2015.

[28] Julien Lesgourgues and Sergio Pastor. Neutrino mass from cosmology. *Advances in High Energy Physics*, 2012, 2012.

[29] PAR Ade, RW Aikin, D Barkats, SJ Benton, CA Bischoff, JJ Bock, JA Brevik, I Buder, E Bullock, CD Dowell, et al. Detection of b-mode polarization at degree angular scales by bicep2. *Physical Review Letters*, 112(24):241101, 2014.

[30] Robert Hirsch. Seizing the light. *A history of photography*, 2008.

[31] Martin Griffiths. A brief history of astronomical imaging. In *Choosing and Using Astronomical Filters*, pages 1–8. Springer, 2015.

[32] Donald H Andrews, WF Brucksch Jr, WT Ziegler, and ER Blanchard. Attenuated superconductors i. for measuring infra-red radiation. *Review of Scientific Instruments*, 13(7):281–292, 1942.

[33] Samuel Pierpont Langley. The bolometer and radiant energy. In *Proceedings of the American Academy of Arts and Sciences*, volume 16, pages 342–358. JSTOR, 1880.

[34] C Enss and D McCammon. Physical principles of low temperature detectors: ultimate performance limits and current detector capabilities. *Journal of Low Temperature Physics*, 151(1-2):5–24, 2008.

[35] DH Andrews, RD Fowler, and MC Williams. The effect of alpha-particles on a superconductor. *Physical Review*, 76(1):154, 1949.

[36] F Simon. Application of low temperature calorimetry to radioactive measurements. *Nature*, 135(3418):763, 1935.

[37] H Kamerlingh Onnes. The resistance of pure mercury at helium temperatures. *Commun. Phys. Lab. Univ. Leiden*, 12(120):1, 1911.

[38] Michael Tinkham. *Introduction to superconductivity*. Courier Corporation, 1996.

[39] Walther Meissner and Robert Ochsenfeld. Ein neuer effekt bei eintritt der supraleitfähigkeit. *Naturwissenschaften*, 21(44):787–788, 1933.

[40] Leon N Cooper. Superconductivity in the neighborhood of metallic contacts. *Physical Review Letters*, 6(12):689, 1961.

[41] Hans Meissner. Superconductivity of contacts with interposed barriers. *Physical Review*, 117(3):672, 1960.

[42] Noboru Sato. Crystallographic structure and superconductive properties of nb-ti films with an artificially layered structure. *Journal of applied physics*, 67(12):7493–7506, 1990.

[43] Michael R Vissers, Jiansong Gao, Martin Sandberg, Shannon M Duff, David S Wisbey, Kent D Irwin, and David P Pappas. Proximity-coupled ti/tin multilayers for use in kinetic inductance detectors. *Applied Physics Letters*, 102(23):232603, 2013.

[44] J. Schlaerth, N. Czakon, P. Day, T. Downes, R. Duan, J. Glenn, S. Golwala, M. Hollister, H. LeDuc, P. Maloney, B. Mazin, H. Nguyen, O. Noroozian, J. Sayers, S. Siegel, and J. Zmuidzinas. The status of music: A multicolor sub/millimeter mkid instrument. *Journal of Low Temperature Physics*, pages 1–7, 2012. 10.1007/s10909-012-0541-7.

[45] P Szypryt, BA Mazin, B Bumble, HG Leduc, and L Baker. Ultraviolet, optical, and near-ir microwave kinetic inductance detector materials developments. *IEEE Transactions on Applied Superconductivity*, 25(3):1–4, 2015.

[46] Jonas Zmuidzinas. Superconducting microresonators: Physics and applications. *Annual Review of Condensed Matter Physics*, 3(1):169–214, 2012.

[47] A. V. SERGEEV and M. YU. REIZER. Photoresponse mechanisms of thin superconducting films and superconducting detectors. *International Journal of Modern Physics B*, 10(06):635–667, 1996.

[48] AG Kozorezov, AF Volkov, JK Wigmore, A Peacock, A Poelaert, and R Den Hartog. Quasiparticle-phonon downconversion in nonequilibrium superconductors. *Physical Review B*, 61(17):11807, 2000.

[49] PJ De Visser, SJC Yates, T Guruswamy, DJ Goldie, S Withington, A Neto, N Llombart, AM Baryshev, TM Klapwijk, and JJA Baselmans. The non-equilibrium response of a superconductor to pair-breaking radiation measured over a broad frequency band. *Applied Physics Letters*, 106(25):252602, 2015.

[50] C. M. Wilson, L. Frunzio, and D. E. Prober. Time-resolved measurements of thermodynamic fluctuations of the particle number in a nondegenerate fermi gas. *Phys. Rev. Lett.*, 87:067004, Jul 2001.

[51]   S. B. Kaplan, C. C. Chi, D. N. Langenberg, J. J. Chang, S. Jafarey, and D. J. Scalapino. Quasiparticle and phonon lifetimes in superconductors. *Phys. Rev. B*, 14:4854–4873, Dec 1976.

[52]   J Gao, MR Vissers, MO Sandberg, FCS da Silva, SW Nam, DP Pappas, DS Wisbey, EC Langman, SR Meeker, BA Mazin, et al. A titanium-nitride near-infrared kinetic inductance photon-counting detector and its anomalous electrodynamics. *Applied Physics Letters*, 101(14):142602, 2012.

[53]   Henry G. Leduc, Bruce Bumble, Peter K. Day, Byeong Ho Eom, Jiansong Gao, Sunil Golwala, Benjamin A. Mazin, Sean McHugh, Andrew Merrill, David C. Moore, Omid Noroozian, Anthony D. Turner, and Jonas Zmuidzinas. Titanium nitride films for ultrasensitive microresonator detectors. *Applied Physics Letters*, 97(10):102509, 2010.

[54]   C. Enss, editor. *Cryogenic Particle Detection.* Springer, 2005.

[55]   MD Niemack, Y Zhao, E Wollack, R Thornton, ER Switzer, DS Swetz, ST Staggs, L Page, O Stryzak, H Moseley, et al. A kilopixel array of tes bolometers for act: Development, testing, and first light. *Journal of Low Temperature Physics*, 151(3-4):690–696, 2008.

[56]   *5,120 superconducting bolometers for the PIPER balloon-borne CMB polarization experiment*, volume 7741, 2010.

[57]   A. Monfardini, A. Benoit, A. Bideaud, N. Boudou, M. Calvo, P. Camus, C. Hoffmann, F.-X. Desert, S. Leclercq, M. Roesch, K. Schuster, P. Ade, S. Doyle, P. Mauskopf, E. Pascale, C. Tucker, A. Bourrion, J. Macias-Perez, C. Vescovi, A. Barishev, J. Baselmans, L. Ferrari, S. Yates, A. Cruciani, P. De Bernardis, S. Masi, C. Giordano, B. Marghesin, H. Leduc, and L. Swenson. The neel iram kid arrays (nika). *Journal of Low Temperature Physics*, pages 1–6, 2011. 10.1007/s10909-011-0451-0.

[58]   Loren J Swenson, Peter K Day, Charles D Dowell, Byeong H Eom, Matthew I Hollister, Robert Jarnot, Attila Kovács, Henry G Leduc, Christopher M McKenney, Ryan Monroe, et al. Mako: a pathfinder instrument for on-sky demonstration of low-cost 350 micron imaging arrays. In

SPIE Astronomical Telescopes+ Instrumentation, pages 84520P–84520P. International Society for Optics and Photonics, 2012.

[59] Benjamin A. Mazin, Kieran O'Brien, Sean McHugh, Bruce Bumble, David Moore, Sunil Golwala, and Jonas Zmuidzinas. Arcons: a highly multiplexed superconducting optical to near-ir camera. *Proc. SPIE*, 7735:773518, 2010.

[60] Sean McHugh, Benjamin A Mazin, Bruno Serfass, Seth Meeker, Kieran O'Brien, Ran Duan, Rick Raffanti, and Dan Werthimer. A readout for large arrays of microwave kinetic inductance detectors. *Review of Scientific Instruments*, 83(4):044702, 2012.

[61] SJC Yates, AM Baryshev, JJA Baselmans, B Klein, and R Güsten. Fast fourier transform spectrometer readout for large arrays of microwave kinetic inductance detectors. *Applied Physics Letters*, 95(4):042504, 2009.

[62] Bradley R Johnson, Daniel Flanigan, Maximilian H Abitbol, Peter AR Ade, Sean Bryan, Hsiao-Mei Cho, Rahul Datta, Peter Day, Simon M Doyle, Kent Irwin, et al. Polarization sensitive multi-chroic mkids. In *SPIE Astronomical Telescopes+ Instrumentation*, pages 99140X–99140X. International Society for Optics and Photonics, 2016.

[63] Alessandro Monfardini, Alain Benoit, Aurélien Bideaud, L Swenson, A Cruciani, P Camus, C Hoffmann, FX Désert, S Doyle, P Ade, et al. A dual-band millimeter-wave kinetic inductance camera for the iram 30 m telescope. *The Astrophysical Journal Supplement Series*, 194(2):24, 2011.

[64] J Hubmayr, JA Beall, D Becker, JA Brevik, HM Cho, G Che, M Devlin, B Dober, J Gao, N Galitzki, et al. Dual-polarization-sensitive kinetic inductance detectors for balloon-borne sub-millimeter polarimetry. *Journal of Low Temperature Physics*, 176(3-4):490–496, 2014.

[65] Omid Noroozian, Peter K Day, Byeong Ho Eom, Henry G Leduc, and Jonas Zmuidzinas. Crosstalk reduction for superconducting microwave resonator arrays. *IEEE Transactions on Microwave Theory and Techniques*, 60(5):1235–1243, 2012.

[66] Sam Rowe, Enzo Pascale, Simon Doyle, Chris Dunscombe, Peter Hargrave, Andreas Papageorgio, Ken Wood, Peter AR Ade, Peter Barry, Aurélien Bideaud, et al. A passive terahertz video camera based on lumped element kinetic inductance detectors. *Review of Scientific Instruments*, 87(3):033105, 2016.

[67] B Dober, JA Austermann, JA Beall, D Becker, G Che, HM Cho, M Devlin, SM Duff, N Galitzki, J Gao, et al. Optical demonstration of thz, dual-polarization sensitive microwave kinetic inductance detectors. *Journal of Low Temperature Physics*, pages 1–7, 2015.

[68] Gerhard Ulbricht, Benjamin A Mazin, Paul Szypryt, Alex B Walter, Clint Bockstiegel, and Bruce Bumble. Highly multiplexible thermal kinetic inductance detectors for x-ray imaging spectroscopy. *Applied Physics Letters*, 106(25):251103, 2015.

[69] Thomas W Cecil, Lisa Gades, Timothy Madden, Daikang Yan, and Antonino Miceli. Optimization of thermal kinetic inductance detectors for x-ray spectroscopy. *IEEE Transactions on Applied Superconductivity*, 25(3):2400805–5, 2015.

[70] Erik A Tholén, Adem Ergül, Evelyn M Doherty, Frank M Weber, Fabien Grégis, and David B Haviland. Nonlinearities and parametric amplification in superconducting coplanar waveguide resonators. *Applied physics letters*, 90(25):253509, 2007.

[71] Andreas Wallraff, David I Schuster, Alexandre Blais, L Frunzio, R-S Huang, J Majer, S Kumar, Steven M Girvin, and Robert J Schoelkopf. Strong coupling of a single photon to a superconducting qubit using circuit quantum electrodynamics. *Nature*, 431(7005):162–167, 2004.

[72] JAB Mates, GC Hilton, KD Irwin, LR Vale, and KW Lehnert. Demonstration of a multiplexer of dissipationless superconducting quantum interference devices. *Applied Physics Letters*, 92(2):023514, 2008.

[73] Albert A Michelson and Edward W Morley. On the relative motion of the earth and of the luminiferous ether. *Sidereal Messenger, vol. 6, pp. 306-310*, 6:306–310, 1887.

[74] H. Fizeau. Rapport sur le concours du prix bordin de l'année 1867. *Comptes Rendus des Séances de l'Académie des Sciences*, 66:932–934, 1868.

[75] Albert A Michelson. Measurement of jupiter's satellites by interference. *Publications of the Astronomical Society of the Pacific*, 3(17):274–278, 1891.

[76] Albert A Michelson and Francis G Pease. Measurement of the diameter of alpha-orionis by the interferometer. *Proceedings of the National Academy of Sciences*, 7(5):143–146, 1921.

[77] A Kogut, DJ Fixsen, DT Chuss, J Dotson, E Dwek, M Halpern, GF Hinshaw, SM Meyer, SH Moseley, MD Seiffert, et al. The primordial inflation explorer (pixie): a nulling polarimeter for cosmic microwave background observations. *Journal of Cosmology and Astroparticle Physics*, 2011(07):025, 2011.

[78] EM Leitch, JM Kovac, C Pryke, JE Carlstrom, NW Halverson, WL Holzapfel, M Dragovan, B Reddall, and ES Sandberg. Measurement of polarization with the degree angular scale interferometer. *Nature*, 420(6917):763–771, 2002.

[79] Andrei L Korotkov, Jaiseung Kim, Gregory S Tucker, Amanda Gault, Peter Hyland, Siddharth Malu, Peter T Timbie, Emory F Bunn, Evan Bierman, Brian Keating, et al. The millimeter-wave bolometric interferometer. In *SPIE Astronomical Telescopes+ Instrumentation*, pages 62750X–62750X. International Society for Optics and Photonics, 2006.

[80] E. Battistelli, A. Baú, D. Bennett, L. Bergé, J.-Ph. Bernard, P. de Bernardis, G. Bordier, A. Bounab, É. Bréelle, E.F. Bunn, M. Calvo, R. Charlassier, S. Collin, A. Coppolecchia, A. Cruciani, G. Curran, M. de Petris, L. Dumoulin, A. Gault, M. Gervasi, A. Ghribi, M. Giard, C. Giordano, Y. Giraud-Héraud, M. Gradziel, L. Guglielmi, J.-Ch. Hamilton, V. Haynes, J. Kaplan, A. Korotkov, J. Landé, B. Maffei, M. Maiello, S. Malu, S. Marnieros, J. Martino, S. Masi, A. Murphy, F. Nati, C. O'Sullivan, F. Pajot, A. Passerini, S. Peterzen, F. Piacentini, M. Piat, L. Piccirillo, G. Pisano, G. Polenta, D. Prêle, D. Romano, C. Rosset, M. Salatino, A. Schillaci, G. Sironi, R. Sordini, S. Spinelli, A. Tartari, P. Timbie, G. Tucker, L. Vibert,

F. Voisin, R.A. Watson, and M. Zannoni. Qubic: The qu bolometric interferometer for cosmology. *Astroparticle Physics*, 34(9):705 – 716, 2011.

[81] J Aumont, S Banfi, P Battaglia, ES Battistelli, A Baù, B Bélier, D Bennett, L Bergé, J Ph Bernard, M Bersanelli, et al. Qubic technological design report. *arXiv preprint arXiv:1609.04372*, 2016.

[82] A. Tartari, J. Aumont, S. Banfi, P. Battaglia, E. S. Battistelli, A. Baù, B. Bélier, D. Bennett, L. Bergé, J. Ph. Bernard, M. Bersanelli, M. A. Bigot-Sazy, N. Bleurvacq, G. Bordier, J. Brossard, E. F. Bunn, D. Buzi, D. Cammilleri, F. Cavaliere, P. Chanial, C. Chapron, A. Coppolecchia, G. D'Alessandro, P. De Bernardis, T. Decourcelle, F. Del Torto, M. De Petris, L. Dumoulin, C. Franceschet, A. Gault, D. Gayer, M. Gervasi, A. Ghribi, M. Giard, Y. Giraud-Héraud, M. Gradziel, L. Grandsire, J. Ch. Hamilton, V. Haynes, N. Holtzer, J. Kaplan, A. Korotkov, J. Lande, A. Lowitz, B. Maffei, S. Marnieros, J. Martino, S. Masi, M. McCulloch, S. Melhuish, A. Mennella, L. Montier, A. Murphy, D. Néel, M. W. Ng, C. O'Sullivan, F. Pajot, A. Passerini, C. Perbost, F. Piacentini, M. Piat, L. Piccirillo, G. Pisano, D. Prêle, D. Rambaud, O. Rigaut, M. Salatino, A. Schillaci, S. Scully, M. M. Stolpovskiy, P. Timbie, G. Tucker, D. Viganò, F. Voisin, B. Watson, and M." Zannoni. Qubic: A fizeau interferometer targeting primordial b-modes. *Journal of Low Temperature Physics*, 184(3):739–745, 2016.

[83] C. Perbost, S. Marnieros, B. Bélier, M. Piat, D. Prêle, F. Voisin, and T. Decourcelle. A 256-tes array for the detection of cmb b-mode polarisation. *Journal of Low Temperature Physics*, 184(3):793–798, 2016.

[84] Créidhe O'Sulivan, Stephen Scully, Donnacha Gayer, Marcin Gradziel, J Anthony Murphy, Marco De Petris, Daniele Buzi, Massimo Gervasi, Mario Zannoni, Jean-Christophe Hamilton, et al. The qu bolometric interferometer for cosmology (qubic). 2015.

[85] Stephen Scully. *Quasi-Optical Design and Analysis of a Bolometric Interferometer for Cosmic Microwave Background Radiation Experiments*. PhD thesis, National University of Ireland Maynooth, 2016.

[86] D. Prêle, F. Voisin, M. Piat, T. Decourcelle, C. Perbost, C. Chapron, D. Rambaud, S. Maestre, W. Marty, and L. Montier. A 128 multiplexing factor time-domain squid multiplexer. *Journal of Low Temperature Physics*, 184(1):363–368, 2016.

[87] R Adam, PAR Ade, N Aghanim, M Arnaud, J Aumont, C Baccigalupi, AJ Banday, RB Barreiro, JG Bartlett, N Bartolo, et al. Planck intermediate results-xxx. the angular power spectrum of polarized dust emission at intermediate and high galactic latitudes. *Astronomy & Astrophysics*, 586:A133, 2016.

[88] Peter T Timbie and Greg S Tucker. Adding interferometry for cmbpol. In *Journal of Physics: Conference Series*, volume 155, page 012003. IOP Publishing, 2009.

[89] M-A Bigot-Sazy, R Charlassier, J-Ch Hamilton, J Kaplan, and G Zahariade. Self-calibration: an efficient method to control systematic effects in bolometric interferometry. *Astronomy & Astrophysics*, 550:A59, 2013.

[90] J Errard, PAR Ade, Y Akiba, K Arnold, M Atlas, C Baccigalupi, D Barron, D Boettger, J Borrill, S Chapman, et al. Modeling atmospheric emission for cmb ground-based observations. *The Astrophysical Journal*, 809(1):63, 2015.

[91] Simon Doyle, Philip Mauskopf, J Naylon, Adrian Porch, and C Duncombe. Lumped element kinetic inductance detectors. *Journal of Low Temperature Physics*, 151(1-2):530–536, 2008.

[92] Simon Doyle. *Lumped Element Kinetic Inductance Detectors*. PhD thesis, Brown Cardiff University, 2008.

[93] Jiansong Gao. *The physics of superconducting microwave resonators*. PhD thesis, California Institute of Technology, 2008.

[94] Inder Jit Bahl. *Lumped elements for RF and microwave circuits*. Artech house, 2003.

[95] HM Greenhouse. Design of planar rectangular microelectronic inductors. *IEEE Transactions on parts, hybrids, and packaging*, 10(2):101–109, 1974.

[96] DC Mattis and John Bardeen. Theory of the anomalous skin effect in normal and superconducting metals. *Physical Review*, 111(2):412, 1958.

[97] O.V. Lounasmaa. *Experimental Principles and Methods Below 1 K.* Academic Press Limited, London, 1974.

[98] Grant Wilson. *An Instrument and Technique for Measuring the Anisotropy in the Cosmic Microwave Background Radiation.* PhD thesis, Brown University, 1998.

[99] J.E. Jensen, W.A. Tuttle, R.B. Stewart, H. Brechna, and A.G. Prodell, editors. *Brookhaven National Laboratory Selected Cryogenic Data Notebook.* United States Department of Energy, 1980.

[100] Karwan Rostem, David T Chuss, Nathan P Lourie, George M Voellmer, and Edward J Wollack. A waveguide-coupled thermally isolated radiometric source. *Review of Scientific Instruments*, 84(4):044701, 2013.

[101] Paul F Goldsmith, Institute of Electrical, Electronics Engineers, Microwave Theory, and Techniques Society. *Quasioptical systems: Gaussian beam quasioptical propagation and applications.* IEEE press New York, 1998.

[102] Emily Barrentine. *The Development of a Transition-Edge Hot-Electron Microbolometer for Observation of the Cosmic Microwave Background.* PhD thesis, University of Wisconsin - Madison, 2011.

[103] Frank Pobell. *Matter and Methods at Low Temperatures.* Springer-Verlag, Berlin, 1992.

[104] G. Ventura and V. Martelli. Thermal conductivity of kevlar 49 between 7 and 290 k. *Cryogenics*, 49(12):735 − 737, 2009.

[105] K. Flachbart, A. Feher, S. Janos, Z. Malek, and A. Ryska. Thermal conductivity of nbti alloy in the low-temperature range. *physica status solidi (b)*, 85(2):545–551, 1978.

[106] M Iavarone, G Karapetrov, A Koshelev, W K Kwok, D Hinks, G W Crabtree, W N Kang, Eun-Mi Choi, Hyun Jung Kim, and Sung-Ik Lee. Mgb 2 : directional tunnelling and two-band superconductivity. *Superconductor Science and Technology*, 16(2):156, 2003.

[107] Mun-Seog Kim, John A. Skinta, Thomas R. Lemberger, W. N. Kang, Hyeong-Jin Kim, Eun-Mi Choi, and Sung-Ik Lee. Reflection of a two-gap nature in penetration-depth measurements of mgb$_2$ film. *Phys. Rev. B*, 66:064511, Aug 2002.

[108] H. J. Choi, D. Roundy, H. Sun, M. L. Cohen, and S. G. Louie. Superconducting energy gaps, low temperature specific heat, and quasiparticle spectra of MgB2. *eprint arXiv:cond-mat/0111183*, November 2001.

[109] Warren Pickett. Superconductivity: Mind the double gap. *Nature*, 418(6899):733–734, 2002.

[110] G Binnig, A Baratoff, HE Hoenig, and JG Bednorz. Two-band superconductivity in nb-doped srti o 3. *Physical Review Letters*, 45(16):1352, 1980.

[111] P. C. J. J. Coumou, E. F. C. Driessen, J. Bueno, C. Chapelier, and T. M. Klapwijk. Electrodynamic response and local tunneling spectroscopy of strongly disordered superconducting tin films. *Phys. Rev. B*, 88:180505, Nov 2013.

[112] J Bueno, PCJJ Coumou, G Zheng, PJ de Visser, TM Klapwijk, EFC Driessen, S Doyle, and JJ A Baselmans. Anomalous response of superconducting titanium nitride resonators to terahertz radiation. *Applied Physics Letters*, 105(19):192601, 2014.

[113] P Szypryt, BA Mazin, G Ulbricht, B Bumble, SR Meeker, C Bockstiegel, and AB Walter. High quality factor platinum silicide microwave kinetic inductance detectors. *arXiv preprint arXiv:1610.00725*, 2016.